

## Deriving Stellar Properties, Distances, and Reddenings using Photometry and Astrometry with BRUTUS

JOSHUA S. SPEAGLE,<sup>1,2,3,4,5</sup> CATHERINE ZUCKER,<sup>5,6</sup> ANGUS BEANE,<sup>5</sup> PHILLIP A. CARGILE,<sup>5</sup> AARON DOTTER,<sup>5</sup>  
DOUGLAS P. FINKBEINER,<sup>5,7</sup> GREGORY M. GREEN,<sup>8</sup> BENJAMIN D. JOHNSON,<sup>5</sup> EDWARD F. SCHLAFLY,<sup>9,6</sup> ANA BONACA,<sup>5,10</sup>  
CHARLIE CONROY,<sup>5</sup> GWENDOLYN EADIE,<sup>1,2</sup> DANIEL J. EISENSTEIN,<sup>5</sup> ALYSSA A. GOODMAN,<sup>5,11</sup> JIWON JESSE HAN,<sup>5</sup>  
HARSHIL M. KAMDAR,<sup>5</sup> ROHAN NAIDU,<sup>5,12</sup> HANS-WALTER RIX,<sup>8</sup> ANDREW K. SAYDJARI,<sup>7,5,13</sup>  
YUAN-SEN TING (丁源森),<sup>14,13,15,16,17,18</sup> AND IOANA A. ZELKO<sup>5,19,20</sup>

<sup>1</sup>*Department of Statistical Sciences, University of Toronto, Toronto, ON M5S 3G3, Canada*

<sup>2</sup>*David A. Dunlap Department of Astronomy & Astrophysics, University of Toronto, Toronto, ON M5S 3H4, Canada*

<sup>3</sup>*Dunlap Institute for Astronomy & Astrophysics, University of Toronto, Toronto, ON M5S 3H4, Canada*

<sup>4</sup>*Data Sciences Institute, University of Toronto, 17th Floor, Ontario Power Building, 700 University Ave, Toronto, ON M5G 1Z5, Canada*

<sup>5</sup>*Center for Astrophysics | Harvard & Smithsonian, 60 Garden St., Cambridge, MA, USA 02138*

<sup>6</sup>*Space Telescope Science Institute, 3700 San Martin Drive, Baltimore, MD 21218, USA*

<sup>7</sup>*Department of Physics, Harvard University, 17 Oxford St, Cambridge, MA 02138*

<sup>8</sup>*Max-Planck-Institut für Astronomie, Königstuhl 17, D-69117 Heidelberg, Germany*

<sup>9</sup>*Lawrence Livermore National Laboratory, 7000 East Avenue, Livermore, CA 94550, USA*

<sup>10</sup>*The Observatories of the Carnegie Institution for Science, 813 Santa Barbara Street, Pasadena, 91101, CA, USA*

<sup>11</sup>*Radcliffe Institute for Advanced Study, Harvard University, 10 Garden St, Cambridge, MA 02138*

<sup>12</sup>*Kauli Institute for Astrophysics and Space Research, Massachusetts Institute of Technology, 70 Vassar Street, Cambridge, MA 02139, USA*

<sup>13</sup>*Department of Astrophysical Sciences, Princeton University, Princeton, NJ 08544, USA*

<sup>14</sup>*Institute for Advanced Study, Princeton, NJ 08540, USA*

<sup>15</sup>*Observatories of the Carnegie Institution of Washington, 813 Santa Barbara Street, Pasadena, CA 91101, USA*

<sup>16</sup>*Research School of Astronomy and Astrophysics, Australian National University, Cotter Road, ACT 2611, Canberra, Australia*

<sup>17</sup>*Research School of Computer Science, Australian National University, Acton ACT 2601, Australia*

<sup>18</sup>*Department of Astronomy, The Ohio State University, Columbus, OH 43210, USA*

<sup>19</sup>*Canadian Institute for Theoretical Astrophysics, University of Toronto, 60 St George Street, Toronto, M5S 3H8, Ontario, Canada*

<sup>20</sup>*Department of Physics and Astronomy, University of California-Los Angeles, 475 Portola Plaza, Los Angeles, CA 90095, USA*

### ABSTRACT

We present BRUTUS, an open source PYTHON package for quickly deriving stellar properties, distances, and reddenings to stars based on grids of stellar models constrained by photometric and astrometric data. We outline the statistical framework for deriving these quantities, its implementation, and various Galactic priors over the 3-D distribution of stars, stellar properties, and dust extinction (including  $R_V$  variation). We establish a procedure to empirically calibrate MIST v1.2 isochrones by using open clusters to derive corrections to the effective temperatures and radii of the isochrones, which reduces systematic errors on the lower main sequence. We also describe and apply a method to estimate photometric offsets between stellar models and observed data using nearby, low-reddening field stars. We perform a series of tests on mock and real data to examine parameter recovery with MIST under different modeling assumptions, illustrating that BRUTUS is able to recover distances and other stellar properties using optical to near-infrared photometry and astrometry. The code is publicly available at <https://github.com/joshspeagle/brutus>.

*Keywords:* stellar distance – algorithms – astrostatistics – sky surveys

### 1. INTRODUCTION

One of the central challenges in Galactic astronomy is to convert the projected 2-D positions of sources on the sky into 3-D maps that we can use to infer properties about the Milky Way. This challenge has only accelerated in recent years as large datasets have be-

come publicly available from large projects such as the ground-based Sloan Digital Sky Survey (SDSS; York et al. 2000) and the space-based *Gaia* mission (Gaia Collaboration et al. 2016). Together, these observational efforts promise to provide new, much sharper maps of the stellar components of the Galaxy using billions of individual sources.

Many recent and potential discoveries concerning the structure and evolution of the Milky Way depend upon reliable 3-D maps. Past work with large photometric datasets have discovered large collections of streams (e.g., Belokurov et al. 2006) and mapped out broad components of Milky Way structure (e.g., Jurić et al. 2008). More recent work has uncovered the remnants of a major merger  $\sim 10$  Gyr ago, referred to as “Gaia-Enceladus” or the “Sausage” (e.g., Koppelman et al. 2018; Belokurov et al. 2018; Helmi et al. 2018; Naidu et al. 2021) and a phase-space “spiral” (e.g., Antoja et al. 2018).

Large spectroscopic surveys of stellar chemistry will shed light on the role of hierarchical assembly and radial migration in the present-day distribution of stellar populations (e.g., Roškar et al. 2008). In the halo, accurate phase-space maps of stellar streams will constrain the potential of the Galaxy (e.g., Johnston et al. 1999; Law & Majewski 2010; Bonaca & Hogg 2018; Green & Ting 2020) and probe the existence of a thick dark disk expected in  $\Lambda$ CDM (Read et al. 2008), with the latter having strong implications for the interpretation of direct detection experiments of dark matter (Read 2014). Measuring the radial profile of the inner dark matter halo through maps of dynamical tracers can constrain its accretion history (Wechsler et al. 2002). The key to all these discoveries is the need for a robust statistical framework to infer 3-D properties of a large number of stars.

In order to build these maps, the raw observations from large scale surveys need to be converted into physical quantities such as 3-D positions and velocities, effective temperatures, surface gravities, metallicities,  $\alpha$ -enhancements, masses, and ages. Many of these quantities are reliably estimated from spectroscopy using a combination of empirical relations, theoretical stellar atmosphere models (e.g., ATLAS12 and SYNTHE; Kurucz 1970; Kurucz & Avrett 1981; Kurucz 1993), or some combination of the two (e.g., Ness et al. 2015). Comparisons to the observed flux densities, combined with estimates of foreground extinction and the properties of Galactic dust (i.e. the “reddening”), then enable a measurement of distance (see, e.g., Green et al. 2014).

Most sources ( $\sim 99\%$ ) seen in large photometric surveys, however, do not have measured spectra. Instead, they only have spectral energy distributions (SEDs) that are comprised of flux densities estimated across a range of broad-band and narrow-band photometric filters. More recently, *Gaia* DR2 (Gaia Collaboration et al. 2018) and EDR3 (Gaia Collaboration et al. 2021) has also provided astrometric parallax measurements for

many of these sources, giving independent constraints on the distance. Mapping out the Milky Way in detail and at scale thus requires effective utilization and joint analysis of all of these datasets. Most importantly, it will require robust modeling of stellar SEDs, which will continue to outpace the supply of high-quality parallax measurements and far outpace the supply of even moderate-quality spectra for the foreseeable future.

In recent years there has been extensive work towards this goal from a wide variety of researchers in areas from 3-D dust mapping (e.g., Rezaei Kh. et al. 2018; Leike & Enßlin 2019; Lallement et al. 2019; Green et al. 2019; Leike et al. 2020) to stellar parameter estimation (e.g., Ness et al. 2015; García Pérez et al. 2016; Cargile et al. 2020; Anders et al. 2019; Xiang et al. 2019). We add to these efforts through BRUTUS<sup>1</sup>, a public, open source PYTHON package for quickly and robustly deriving stellar properties, distances, and reddenings to stars with astrometric and/or photometric data. BRUTUS is designed to be well-documented, user-friendly, and highly modular, with various components that can be used for individual stellar parameter estimation, analysis of coeval stellar populations, and 3-D dust mapping within an internally-consistent statistical framework. The code has also already been used in several publications including Zucker & Speagle et al. (2019) and Zucker et al. (2020).

This work joins other recent efforts focused on trying to estimate distances and other stellar properties from astrometry and/or photometry alone. Bailer-Jones et al. (2018) published a large catalog of over a billion distances using only astrometric data from the *Gaia* DR2 and a data-driven model. More recently, Bailer-Jones et al. (2021) has done the same for *Gaia* EDR3 using a similar data-driven approach to estimate distances that incorporates both astrometric and photometric *Gaia* data. An example of work that is most similar to what is presented here is the STARHORSE code (Santiago et al. 2016; Queiroz et al. 2018; Anders et al. 2019), which similar to BRUTUS attempts to estimate stellar parameters, reddenings, *and* distances from photometric and astrometric data using theoretical stellar models. Differences between the two approaches will be discussed in more detail in §3.

The outline of the paper is as follows. In §2, we describe the underlying Bayesian statistical framework and modeling, including the initial set of Galactic priors over the 3-D distribution of stars, dust, and related properties. In §3, we describe the strategy BRUTUS uses for fast exploration and characterization the probabilistic uncertainties for a given source. In §4, we describe the initial set of empirical and theoretical stellar models used to infer stellar properties. In §5, we describe how we use both cluster and field stars to empirically calibrate our

<sup>1</sup> Available online at: <https://github.com/joshspeagle/brutus>.

theoretical isochrones to improve inference, particularly at lower masses. In §6, we describe a series of tests on mock and real data used to validate the performance of the models and the code. We conclude in §7.

Throughout the paper, individual parameters are denoted using standard italicized math fonts ( $\theta$ ) while vectors and matrices are denoted using boldface ( $\boldsymbol{\theta}$ ). Collections of parameters are denoted using sets ( $\boldsymbol{\theta} = \{\theta_i\}_{i=1}^{i=n}$ ). Vectors should be assumed to be in column form (i.e. of shape  $n \times 1$ ) unless explicitly stated otherwise. We will use “hat” notation ( $\hat{\theta}$ ) to define noisy measurements of a particular quantity  $\theta$ .

## 2. STATISTICAL FRAMEWORK

Our statistical framework is divided into four parts. In §2.1, we describe the noiseless (ideal) model for a given source as a function of stellar parameters, dust extinction, and distance. In §2.2, we describe our assumptions regarding the photometric and astrometric data and the corresponding likelihoods. In §2.3, we outline the basis for combining these pieces of information into a Bayesian posterior probability using relevant priors. We discuss these priors in §2.4.

In brief, we assume that:

- Our noiseless model can be described as a linear combination (in magnitudes) of intrinsic stellar, dust, and distance components.
- The measured flux densities (i.e. photometry) and the parallaxes have independently and identically distributed (iid) Normal (i.e. Gaussian) uncertainties.
- The priors for a wide range of parameters can be separated into components involving the stellar initial mass function (IMF), 3-D stellar number density, 3-D metallicity distribution, 3-D age distribution, and 3-D dust extinction.
- The variation in the underlying dust extinction curve can be described with a linear one-parameter model.

See the subsections below for additional details.

### 2.1. Noiseless Model

We assume that the observed magnitudes  $\mathbf{m} \equiv \{m_i\}_{i=1}^{i=b}$  over a set of  $b$  photometric bands can be modeled as

$$\boxed{\mathbf{m}_{\theta,\phi} \equiv \mathbf{M}_{\theta} + \mu + A_V \times (\mathbf{R}_{\theta} + R_V \times \mathbf{R}'_{\theta})} \quad (1)$$

This contains several components:

- The *intrinsic absolute magnitude*  $\mathbf{M}_{\theta}$  of the star as a function of its *intrinsic* (stellar) parameters  $\boldsymbol{\theta}$ .

- The *distance modulus*  $\mu \equiv 5 \log(d/10)$  where  $d$  is the distance to the object in pc.
- The *dust extinction*  $A_V \equiv V_{\text{obs}} - V_{\text{true}}$  in magnitudes, measured using the difference between the observed  $V_{\text{obs}}$  and true  $V_{\text{true}}$  magnitudes in the  $V$ -band.
- The *reddening vector*  $\mathbf{R}_{\theta}$  that determines the wavelength-dependence of extinction across the  $b$  filters.<sup>2</sup>
- The *differential extinction*  $R_V \equiv A_V / (A_B - A_V) \equiv A_V / E(B - V)$  in the  $V$ -band versus the  $B$ -band, where  $E(B - V)$  is often referred to as the color excess.
- The *differential reddening vector*  $\mathbf{R}'_{\theta}$  that modifies the shape of the underlying reddening vector  $\mathbf{R}_{\theta}$ .

For compactness, we define  $\boldsymbol{\phi}$  to be the combined set of all *extrinsic* parameters (here  $\mu$ ,  $A_V$ , and  $R_V$ ) that modify the observed magnitudes to be different from  $\mathbf{M}_{\theta}$ . The combined effect of  $\boldsymbol{\theta}$  and  $\boldsymbol{\phi}$  then generate the observed magnitudes  $\mathbf{m}_{\theta,\phi}$ . We will discuss the logic behind separating  $\boldsymbol{\theta}$  and  $\boldsymbol{\phi}$  into these two separate categories in §3.

#### 2.1.1. Intrinsic Parameters

For the majority of this paper, we define intrinsic (stellar) parameters  $\boldsymbol{\theta}$  as

$$\boldsymbol{\theta} \equiv \begin{bmatrix} M_{\text{init}} \\ [\text{Fe}/\text{H}]_{\text{init}} \\ t_{\text{age}} \end{bmatrix} \quad (2)$$

where  $M_{\text{init}}$  is the initial mass (in  $M_{\odot}$ ),  $[\text{Fe}/\text{H}]_{\text{init}}$  is the initial metallicity (relative to solar), and  $t_{\text{age}}$  is the current age (in Gyr). This is a vast oversimplification of stellar physics and evolution, ignoring the contributions of stellar rotation (Gossage et al. 2019),  $\alpha$ -process element abundance variations (Thomas et al. 2003), binarity (Eldridge et al. 2017), and more. However, given the limited resolution of current, publicly-available photometric data and the difficulty in modeling all of these processes simultaneously, we follow recent work such as Anders et al. (2019) by approximating stellar evolution using only these three parameters. We hope to improve on this in future work.

<sup>2</sup> The dependence on  $\boldsymbol{\theta}$  is due to the changing shape of the stellar spectrum across each filter.

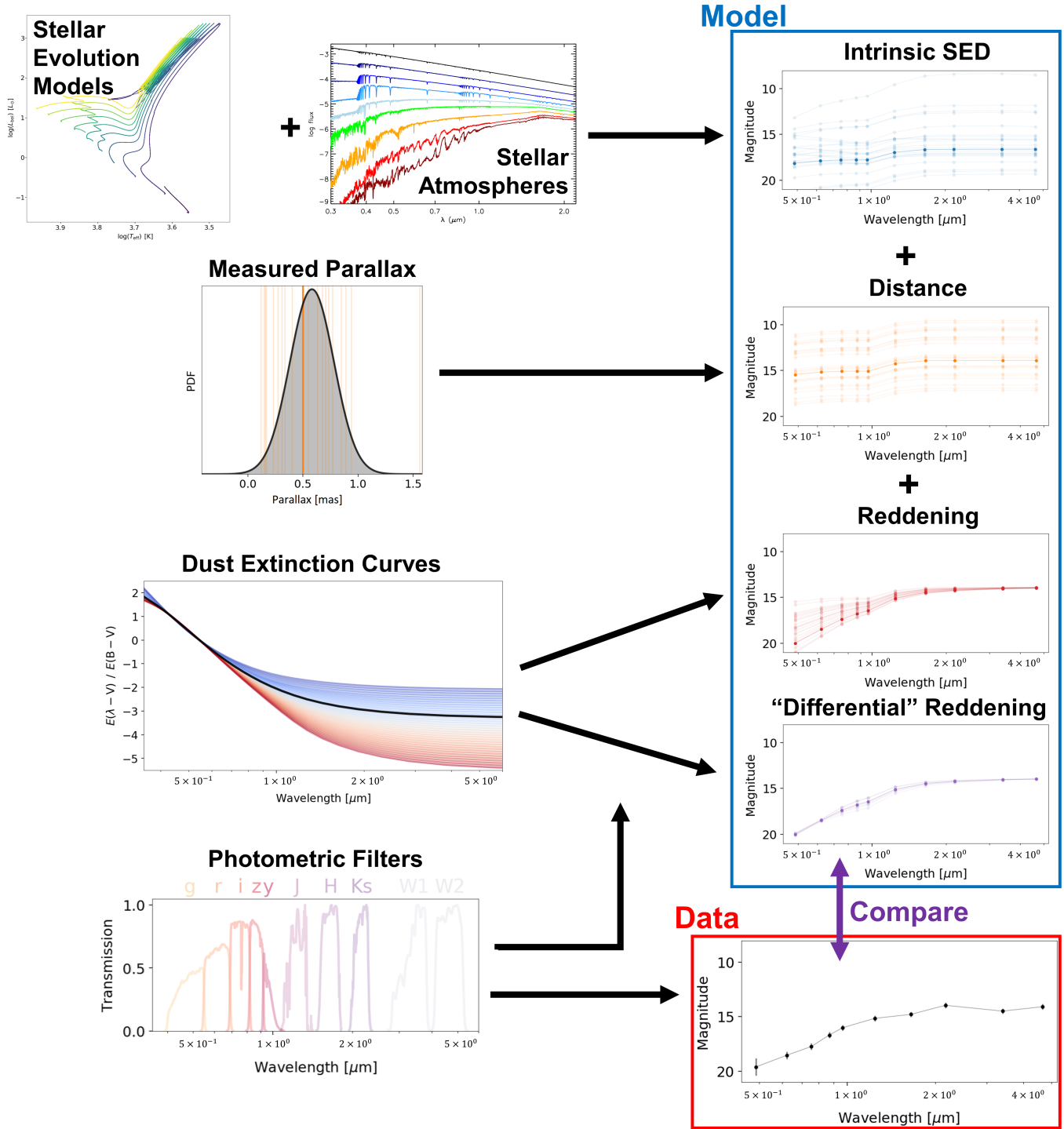


**Figure 1.** An illustration of the components that go into creating stellar spectral energy distributions (SEDs) in BRUTUS. The intrinsic (i.e. absolute, unreddened) magnitudes  $M_{\theta}$  (far top) are constructed using a combination of intrinsic parameters  $\theta$  that incorporate stellar evolutionary models and stellar atmospheric models combined with a given set of photometric filters. These are modified by extrinsic parameters  $\phi$  (middle) including the distance ( $d$ ), which can be compared to astrometric parallax measurements, and the visual extinction ( $A_V$ ) and “differential” reddening ( $R_V$ ), which are based on empirical dust extinction models. These combine to give predicted magnitudes  $m_{\theta,\phi}$  that can be compared to the noisy observed data  $\hat{m}$  (bottom). See §2.1 for additional details.



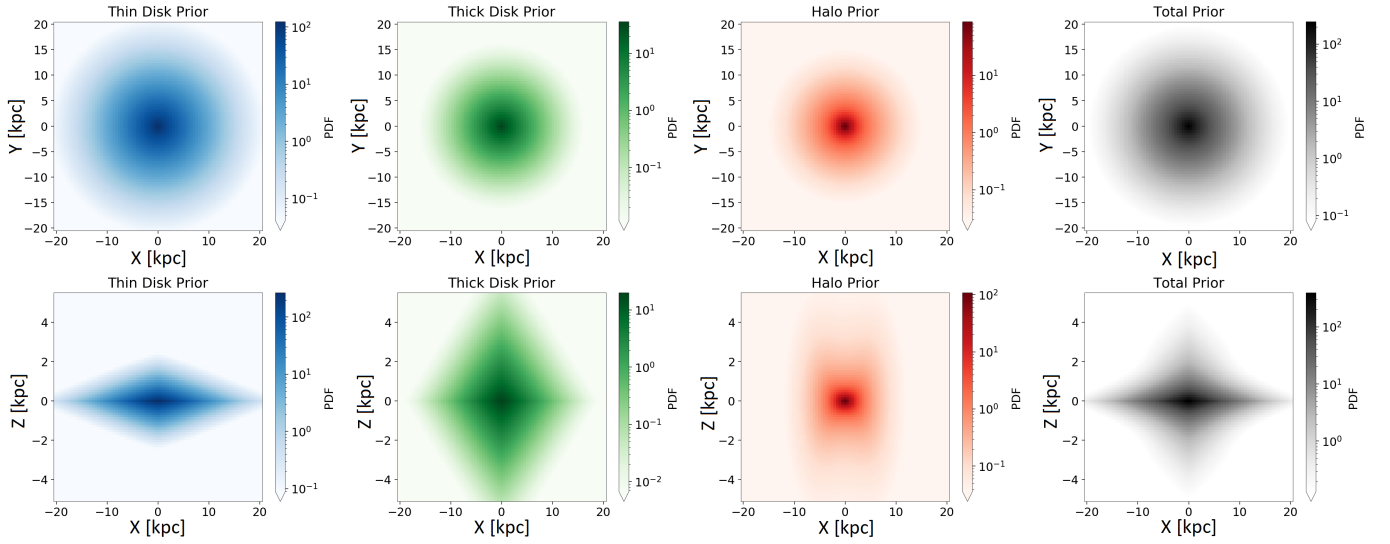


**Figure 2.** The 3-D stellar number density prior used in BRUTUS, marginalized and projected into Galactocentric Cartesian  $X$ - $Y$  (top) and  $X$ - $Z$  (bottom) coordinates. This is divided into thin disk (blue, far left), thick disk (green, center left), and halo (red, center right) components along with their combined contributions (black, far right). The effective prior (not shown here) includes a  $dV \propto d^2$  component centered on the Sun at  $(X, Y, Z) \approx (-8, 0, 0)$  kpc to account for changes in the volume element, leading to suppression/enhancement of the prior relative to the true underlying number density for nearby/faraway sources. See Table 1 and §A.2 for more details.

Theoretical stellar evolutionary tracks can relate these intrinsic parameters  $\theta$  to surface-level stellar parameters

$$\theta_{\star} \equiv \begin{bmatrix} \log g \\ \log T_{\text{eff}} \\ \log L_{\text{bol}} \\ \log R_{\star} \\ [\text{Fe}/\text{H}]_{\text{surf}} \end{bmatrix} \quad (3)$$

where  $g$  is the surface gravity (in cgs),  $T_{\text{eff}}$  is the effective temperature (in K),  $L_{\text{bol}}$  is the bolometric luminosity (in  $L_{\odot}$ ),  $R_{\star}$  is the radius (in  $R_{\odot}$ ), and  $[\text{Fe}/\text{H}]_{\text{surf}}$  is the surface metallicity (relative to solar).<sup>3</sup>  $\theta_{\star}$  can then be connected to the more direct observables through the use of stellar atmospheric models (Kurucz 1970; Gustafsson et al. 2008) and associated line lists (Piskunov et al. 1995; Kupka et al. 2000; Ryabchikova et al. 2015) that relate these parameters to corresponding spectral flux densities  $F_{\nu}(\lambda|\theta)$  as a function of wavelength  $\lambda$ .

The corresponding intrinsic absolute magnitude  $M_i(\theta)$  in a given filter  $i$  with filter transmission curve  $T_i(\lambda)$  is then

$$M_i(\theta) \equiv -2.5 \log \left( \frac{\int_0^{\infty} F_{\nu}(\lambda|\theta) T_i(\lambda) \lambda^{-1} d\lambda}{\int_0^{\infty} S_{\nu}(\lambda) T_i(\lambda) \lambda^{-1} d\lambda} \right) \quad (4)$$

where  $S_{\nu}(\lambda)$  is the spectral flux density used to normalize the observations. In the Vega magnitude system,  $S_{\nu}(\lambda)$  is the spectrum of Vega, while in the AB system  $S_{\nu}(\lambda) = 3631 \text{ Jy}$  is a constant.

Combining these ingredients together then gives us a way to generate the intrinsic magnitudes  $\mathbf{M}_{\theta}$ :

$$\begin{array}{ccc} \theta & \xrightarrow{\text{isochrones}} & \theta_{\star} & \xrightarrow[\text{filters}]{\text{atmospheres}} & \mathbf{M}_{\theta} \\ \begin{bmatrix} M_{\text{init}} \\ [\text{Fe}/\text{H}]_{\text{init}} \\ t_{\text{age}} \end{bmatrix} & \xrightarrow{\text{isochrones}} & \begin{bmatrix} \log g \\ \log T_{\text{eff}} \\ \log L_{\text{bol}} \\ \log R_{\star} \\ [\text{Fe}/\text{H}]_{\text{surf}} \end{bmatrix} & \xrightarrow[\text{filters}]{\text{atmospheres}} & \begin{bmatrix} M_1 \\ \vdots \\ M_b \end{bmatrix} \end{array}$$

### 2.1.2. Extrinsic Parameters

Our intrinsic magnitudes  $\mathbf{M}_{\theta} = \{M_i(\theta)\}_{i=1}^b$  over our  $b$  photometric bands are extinguished by foreground dust with some wavelength-dependent optical depth per  $A_V$ ,  $\tau_{\lambda}$ . The integrated effect for a given scaling factor  $A$  at a distance  $d$  is then

$$m_i(\theta|A, d) = -2.5 \log \left( \frac{d^{-2} \int_0^{\infty} e^{-A\tau_{\lambda}} F_{\nu}(\lambda|\theta) T_i(\lambda) \lambda^{-1} d\lambda}{\int_0^{\infty} S_{\nu}(\lambda) T_i(\lambda) \lambda^{-1} d\lambda} \right). \quad (5)$$

For small  $A$ , we can approximate this expression as

$$m_i(\theta|A, d) \approx M_i(\theta) + A \times R_i(\theta) + \mu(d) \quad (6)$$

where the reddening  $R_i(\theta)$  in the  $i$ th band is

$$R_i(\theta) \equiv \frac{2.5}{\ln 10} \frac{\int_0^{\infty} \tau_{\lambda} F_{\nu}(\lambda|\theta) T_i(\lambda) \lambda^{-1} d\lambda}{\int_0^{\infty} F_{\nu}(\lambda|\theta) T_i(\lambda) \lambda^{-1} d\lambda} \quad (7)$$

and we have added the distance modulus  $\mu = 5 \log(d/10)$  to explicitly account for the impact of the distance  $d$  of the object. For  $A = A_V$  and  $\mathbf{R}_{\theta} = \{R_i(\theta)\}_{i=1}^b$ , this then becomes a simplified version of equation (1).

While the above approximation only strictly holds true for small  $A_V$ , it still generally serves as a good model for observed extinction and reddening for  $A_V \gg 1$  (Green et al. 2014). In addition, while the reddening vector  $\mathbf{R}_{\theta}$  clearly depends on the underlying spectrum  $F_{\nu}(\lambda|\theta)$  and therefore will be different for each star, many approaches further approximate the reddening vector as being independent of the underlying spectrum (i.e.  $\mathbf{R}_{\theta} = \mathbf{R}$ ) (Green et al. 2015, 2018, 2019). As our ability to model the observed extinction is most often limited by our imperfect knowledge of  $\tau_{\lambda}$  and its variation within the Galaxy, this approximation is often reasonable (Schlafly et al. 2016; Green et al. 2021). We will discuss this further in §4.

It is important to note that  $\tau_{\lambda}$  is not universal for foreground dust. It instead depends on a variety of intrinsic properties such as the dust grain size distribution along a given line of sight and the relative composition of dust grains (e.g., silicate versus carbonaceous grains). While the underlying physics are complex (Draine 2003), in practice it has been shown (Fitzpatrick 1999; Schlafly & Finkbeiner 2011; Schlafly et al. 2016) that most of this variability in the optical and near-infrared (NIR) can be modeled with a single parameter  $R_V$  such that

$$\tau_{\lambda, \text{eff}}(R_V) \approx \tau_{\lambda} + R_V \times \tau'_{\lambda} \quad (8)$$

where  $\tau'_{\lambda}$  characterizes the wavelength-dependence of “differential extinction” as a function of  $R_V$ . Adding in this term then gives the corresponding differential reddening in the  $i$ th band as

$$R'_i(\theta) \equiv \frac{2.5}{\ln 10} \frac{\int_0^{\infty} \tau'_{\lambda} F_{\nu}(\lambda|\theta) T_i(\lambda) \lambda^{-1} d\lambda}{\int_0^{\infty} F_{\nu}(\lambda|\theta) T_i(\lambda) \lambda^{-1} d\lambda} \quad (9)$$

Letting  $\mathbf{R}'_{\theta} = \{R'_i(\theta)\}_{i=1}^b$  then gives the final component of the model in equation (1). See §4.1.3 for further discussion on  $R_V$ . This gives a fiducial set of extrinsic parameters  $\phi$  as

$$\phi \equiv \begin{bmatrix} d \\ A_V \\ R_V \end{bmatrix} \quad (10)$$

A schematic illustration of each of the various components of our basic model is shown in Figure 1.

<sup>3</sup> The present-day abundances  $[\text{Fe}/\text{H}]_{\text{surf}}$  differ from the *initial* abundances at birth  $[\text{Fe}/\text{H}]_{\text{init}}$ .

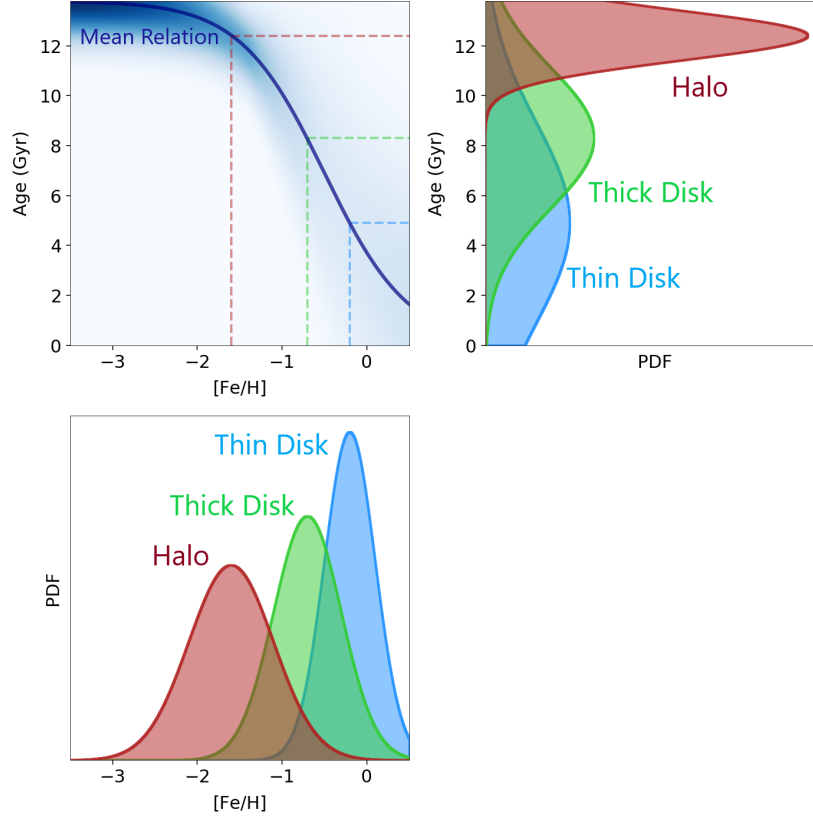


**Figure 3.** The age-metallicity relation (shaded blue density; top left) used to set the thin disk (blue), thick disk (green), and halo (red) 1-D metallicity (bottom-left) and 1-D age (top-right) priors used in BRUTUS. The mean relationship is highlighted as the solid dark blue line. The associated mean values for the ages and metallicities are indicated by the dashed red, green, and blue lines. See Table 1 and §A.3 and §A.4 for more details.

## 2.2. Noisy Data

### 2.2.1. Photometry

We assume that our data contain a set of noisy flux densities  $\hat{\mathbf{F}} = \{\hat{F}_i\}_{i=1}^{i=b}$  in  $b$  photometric bands that are distributed following a Normal distribution around the true flux densities  $\mathbf{F} = \{F_i\}_{i=1}^{i=b}$  with corresponding uncertainties  $\sigma_{\mathbf{F}} = \{\sigma_{F,i}\}_{i=1}^{i=b}$ . More formally,

$$\hat{\mathbf{F}} \sim \mathcal{N}[\mathbf{F}, \mathbf{C}_{\mathbf{F}}] \quad (11)$$

where  $\mathbf{D} \sim \mathcal{N}[\boldsymbol{\mu}, \mathbf{C}]$  indicates that the data  $\mathbf{D} = \hat{\mathbf{F}}$  is drawn from a Normal probability density function (PDF) with mean vector  $\boldsymbol{\mu} = \mathbf{F}$  and covariance matrix  $\mathbf{C} = \mathbf{C}_{\mathbf{F}} = \text{diag}(\sigma_{\mathbf{F}})$ , where  $\text{diag}(\sigma_{\mathbf{F}})$  indicates a diagonal matrix with the  $i$ th value of  $\sigma_{\mathbf{F}}$  located in the  $(i, i)$  matrix position and zeros everywhere else.

The log-likelihood of the observed flux density as a function of  $\boldsymbol{\theta}$  and  $\boldsymbol{\phi}$  follows the PDF of a multivariate Normal distribution:

$$-2 \ln \mathcal{L}_{\text{phot}}(\boldsymbol{\theta}, \boldsymbol{\phi}) = (\hat{\mathbf{F}} - \mathbf{F}_{\boldsymbol{\theta}, \boldsymbol{\phi}})^T \mathbf{C}_{\mathbf{F}}^{-1} (\hat{\mathbf{F}} - \mathbf{F}_{\boldsymbol{\theta}, \boldsymbol{\phi}}) + \ln [\det(2\pi \mathbf{C}_{\mathbf{F}})] \quad (12)$$

where  $\text{T}$  is the transpose operator,  $\mathbf{C}^{-1}$  is the matrix inverse of  $\mathbf{C}$  (i.e. the precision matrix), and  $\det(\cdot)$  is the

determinant of the matrix. In our case where we assume  $\mathbf{C}_{\mathbf{F}}$  is diagonal, this reduces to

$$-2 \ln \mathcal{L}_{\text{phot}}(\boldsymbol{\theta}, \boldsymbol{\phi}) = \sum_{i=1}^b \frac{(\hat{F}_i - F_{\boldsymbol{\theta}, \boldsymbol{\phi}, i})^2}{\sigma_{\mathbf{F}, i}^2} + \ln(2\pi \sigma_{\mathbf{F}, i}^2) \quad (13)$$

Throughout the rest of the paper, we will assume that flux densities are defined in units of “maggies” (i.e. in units relative to the standard reference used to define the magnitude system; Finkbeiner et al. 2004) such that we can convert from flux density to magnitude via

$$\mathbf{m}_{\boldsymbol{\theta}, \boldsymbol{\phi}} \equiv \{-2.5 \log(F_{\boldsymbol{\theta}, \boldsymbol{\phi}, i})\}_{i=1}^{i=b} \quad (14)$$

Note that while this assumption simplifies the majority of the subsequent derivations, it does not impact our results in any way. We will return to this mismatch between our model (in magnitudes) and our data (in flux densities) in §3.

### 2.2.2. Astrometry

In addition to flux densities, we may also have astrometric measurements for many of the sources from

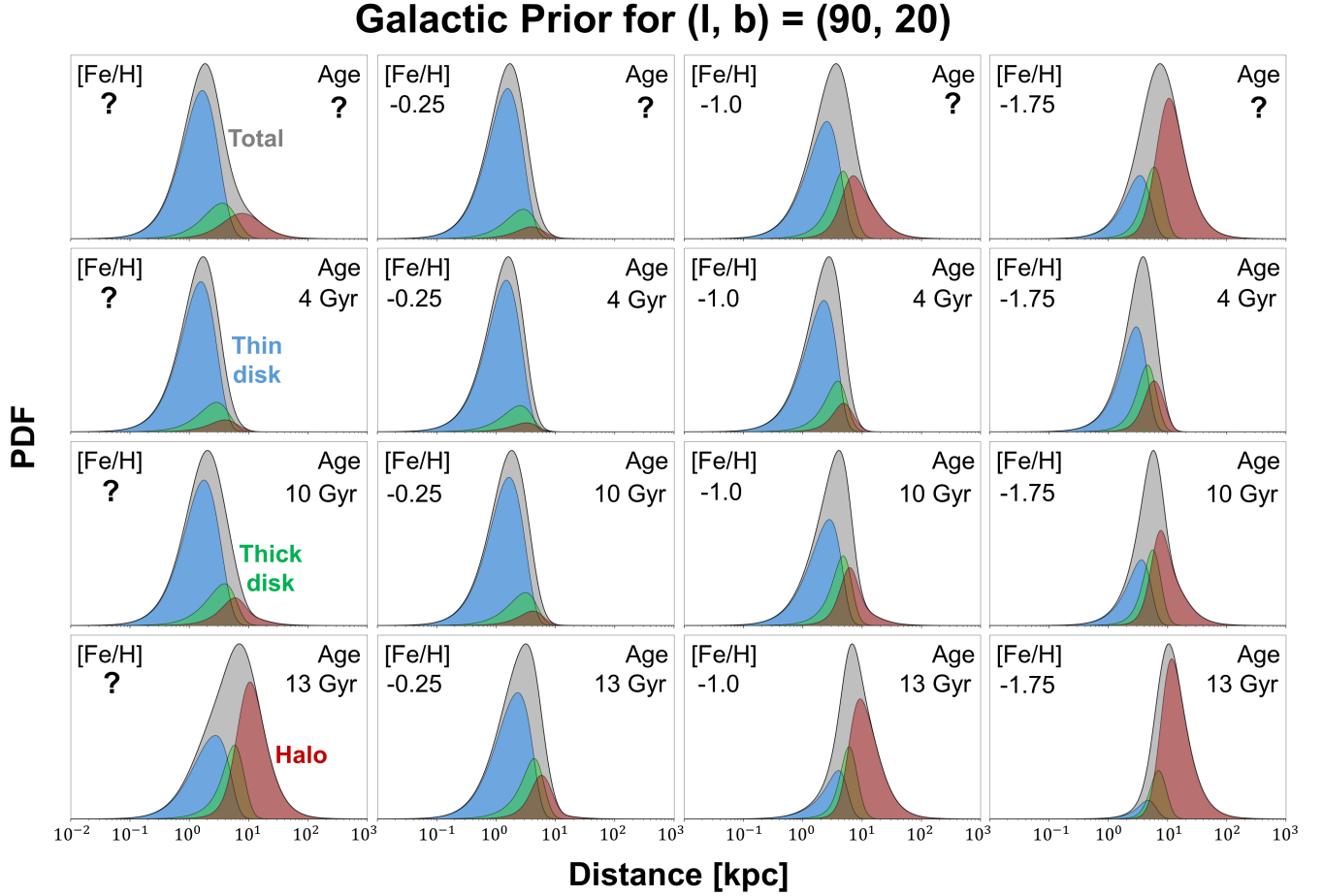


**Figure 4.** An example of the Galactic prior over distance, metallicity, and age used in BRUTUS evaluated for a given sightline with Galactic coordinates  $(\ell, b) = (90^\circ, 20^\circ)$ . Each panel is broken into the total probability density (gray) along with the contribution from the thin disk (blue), thick disk (green), and halo (red). The top-left corner highlights the prior  $\pi(d|\ell, b)$  marginalized over (i.e. assuming unknown values of) stellar metallicity  $[\text{Fe}/\text{H}]$  and age  $t_{\text{age}}$ , as indicated by question marks. The left-most column shows the prior  $\pi(d|\ell, b, t_{\text{age}})$  conditioning only on  $t_{\text{age}}$ , while the top-most row shows the prior  $\pi(d|\ell, b, [\text{Fe}/\text{H}])$  but conditioning on  $[\text{Fe}/\text{H}]$  instead. Each sub-panel shows the prior  $\pi(d|\ell, b, [\text{Fe}/\text{H}], t_{\text{age}})$  conditioning on both  $[\text{Fe}/\text{H}]$  and  $t_{\text{age}}$ . Marginalized over  $[\text{Fe}/\text{H}]$  and  $t_{\text{age}}$ , the prior prefers a source to be in the thin disk with small but non-negligible contributions from the thick disk and halo. Conditioning on low  $[\text{Fe}/\text{H}]$  or high  $t_{\text{age}}$ , however, begins to favor a source being in the halo. Only after conditioning on both low  $[\text{Fe}/\text{H}]$  and high  $t_{\text{age}}$  is a source strongly favored to be in the halo. As expected, at high  $[\text{Fe}/\text{H}]$  and low  $t_{\text{age}}$  a source is almost entirely associated with the thin disk, although small contributions from the thick disk and halo remain due to their much larger number densities (relative to the thin disk) at larger distances. See Table 1, §2.4, and §A for more details.

*Gaia* (Lindegren et al. 2018). While these include both noisy parallax and proper motion measurements, in this work we will only utilize the parallaxes for our inference and leave incorporating proper motions to future work. We assume that the noisy parallax  $\hat{\varpi}$  is Normally distributed about the true parallax  $\varpi \equiv 1/d$  (in mas) for a given distance to the object  $d$  (in kpc) with some scatter  $\sigma_{\varpi}$  such that

$$\hat{\varpi} \sim \mathcal{N}[\varpi, \sigma_{\varpi}]. \quad (15)$$

The corresponding log-likelihood is then

$$-2 \ln \mathcal{L}_{\text{astr}}(\phi) = \frac{(\hat{\varpi} - \varpi(\phi))^2}{\sigma_{\varpi}^2} + \ln(2\pi\sigma_{\varpi}^2) \quad (16)$$

since  $\varpi(\phi) = \varpi(\mu) = \varpi(d)$  is one of the extrinsic parameters we are interested in.

### 2.3. Posterior Probability

The probability  $P(\theta, \phi|\hat{\mathbf{F}}, \hat{\varpi})$  for a particular set of intrinsic parameters  $\theta$  and extrinsic parameters  $\phi$  given the observed  $b$  flux densities  $\hat{\mathbf{F}}$ , parallax  $\hat{\varpi}$ , and prior

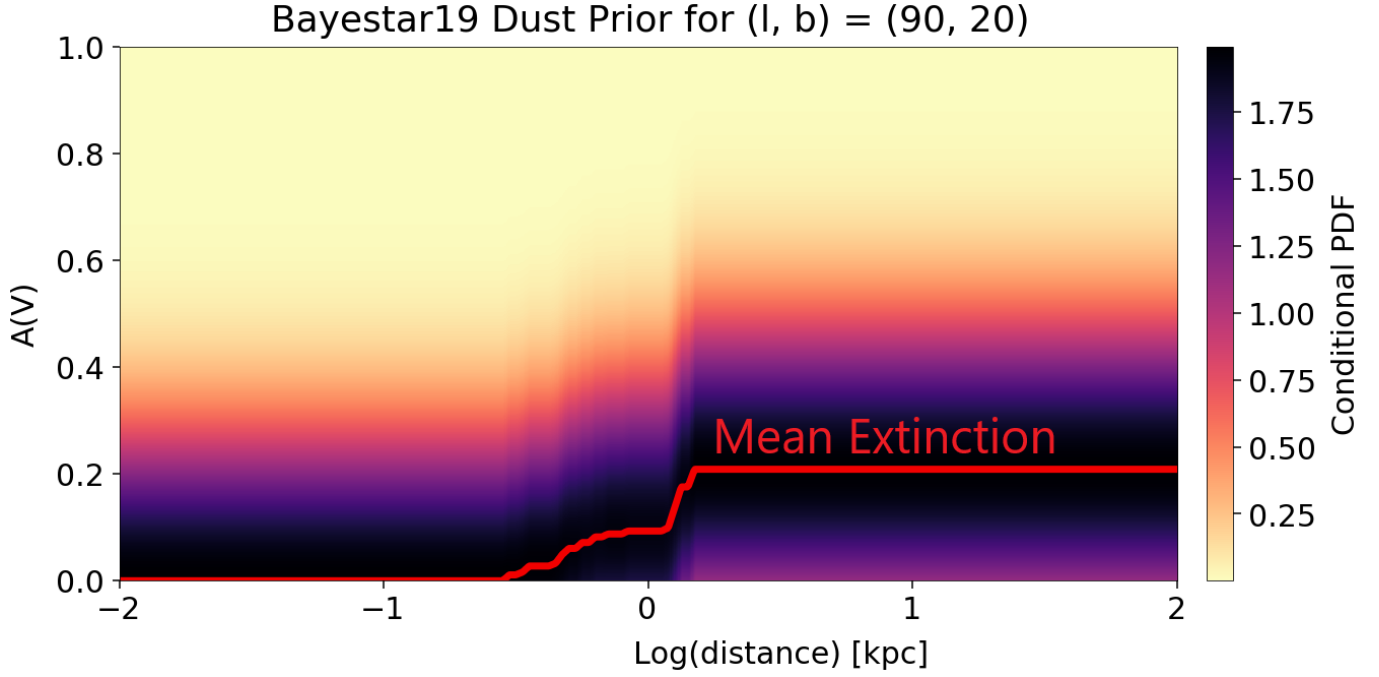


**Figure 5.** An illustration of the Green et al. (2019) Bayestar19 3-D dust prior  $\pi(A_V|\ell, b, d)$  used in BRUTUS along the same  $(\ell, b) = (90^\circ, 20^\circ)$  sightline as Figure 4. The mean relationship is highlighted as the solid red line. There is evidence for diffuse dust between 0.3 kpc and 1.0 kpc and a concentrated dust feature between 1.1 kpc to 1.3 kpc. This increases the preferred  $A_V$  value for a particular source at larger distances, although there is still a substantial amount of variation allowed by the prior. See Table 1 and §A.5 for more details.

knowledge  $P(\boldsymbol{\theta}, \boldsymbol{\phi})$  about  $\boldsymbol{\theta}$  and  $\boldsymbol{\phi}$  can be derived using Bayes Theorem:

$$P(\boldsymbol{\theta}, \boldsymbol{\phi}|\hat{\mathbf{F}}, \hat{\omega}) \propto P(\hat{\mathbf{F}}, \hat{\omega}|\boldsymbol{\theta}, \boldsymbol{\phi})P(\boldsymbol{\theta}, \boldsymbol{\phi})$$

$$\equiv \mathcal{L}_{\text{phot}}(\boldsymbol{\theta}, \boldsymbol{\phi})\mathcal{L}_{\text{astr}}(\boldsymbol{\phi})\pi(\boldsymbol{\theta}, \boldsymbol{\phi}) \quad (17)$$

where  $P(\boldsymbol{\theta}, \boldsymbol{\phi}|\hat{\mathbf{F}}, \hat{\omega})$  is the *posterior* probability for  $\boldsymbol{\theta}$  and  $\boldsymbol{\phi}$ ,  $P(\hat{\mathbf{F}}, \hat{\omega}|\boldsymbol{\theta}, \boldsymbol{\phi}) \equiv \mathcal{L}_{\text{phot}}(\boldsymbol{\theta}, \boldsymbol{\phi})\mathcal{L}_{\text{astr}}(\boldsymbol{\phi})$  is the *likelihood*, which we have split into photometric  $\mathcal{L}_{\text{phot}}(\boldsymbol{\theta}, \boldsymbol{\phi})$  and astrometric  $\mathcal{L}_{\text{astr}}(\boldsymbol{\phi})$  terms, and  $P(\boldsymbol{\theta}, \boldsymbol{\phi}) \equiv \pi(\boldsymbol{\theta}, \boldsymbol{\phi})$  is the *prior*.

Combined, this allows us to translate from a set of observed flux densities  $\hat{\mathbf{F}}$  and parallax  $\hat{\omega}$ , along with their corresponding errors  $\boldsymbol{\sigma}_{\mathbf{F}}$  and  $\sigma_{\omega}$ , into constraints on the distance ( $\mu$ ), dust extinction ( $A_V, R_V$ ), and intrinsic stellar properties ( $\boldsymbol{\theta}$ ) for each source.

#### 2.4. Priors

Our prior  $\pi(\boldsymbol{\theta}, \boldsymbol{\phi})$  over  $\boldsymbol{\theta}$  and  $\boldsymbol{\phi}$  represents a Galactic model describing the 3-D distribution of stars, dust, and their associated properties throughout the Milky Way. Within the stable implementation of BRUTUS in use at the time of writing<sup>4</sup>, the prior is divided up into a few independent components describing several different

processes:

$$\pi(\boldsymbol{\theta}, \boldsymbol{\phi}) \propto \underbrace{\pi(M_{\text{init}})}_{\text{IMF}} \times \underbrace{\pi(d|\ell, b)}_{\text{3D number}} \times \underbrace{\pi([\text{Fe}/\text{H}]_{\text{init}}|d, \ell, b)}_{\text{3D metallicity}} \times \underbrace{\pi(t_{\text{age}}|d, \ell, b)}_{\text{3D age}} \times \underbrace{\pi(A_V|d, \ell, b)}_{\text{3D extinction}} \times \underbrace{\pi(R_V)}_{\text{Dust curve}} \quad (18)$$

where  $d$  is the heliocentric distance of a source and  $(\ell, b)$  are the Galactic longitude and latitude, respectively. While this assumption makes the problem more straightforward, it enforces a couple of assumptions regarding, e.g., the universality of the IMF or the lack of correlations between individual stellar ages and corresponding metallicities.

Schematic illustrations of our 3-D stellar and extinction priors are shown in Figures 2, 3, 4, and 5. A summary of the priors and associated constants are de-

<sup>4</sup> v0.7.5: <http://doi.org/10.5281/zenodo.3711493>



scribed in Table 1. A detailed description can be found in §A. We hope to add in more options for more complex Galactic stellar priors (number densities, metallicities, ages,  $\alpha$ -abundance variations, etc.) and 3-D dust extinction priors, such as those included in DUSTMAPS<sup>5</sup> (Green 2018), in the future.

### 3. IMPLEMENTATION

BRUTUS uses a combination of linear regression, Monte Carlo sampling, and brute force methods to generate fast but robust approximations to the underlying posterior. This approach is able to capture strong covariances between parameters, trace extended structures in this distribution, and characterize multiple possible solutions. The basic procedure works as follows:

1. For all models in a given grid of (intrinsic) stellar parameters, use linear regression in magnitude space to solve for the best-fit solution for our extrinsic parameters  $\phi$  given the intrinsic stellar parameters  $\theta$ .
2. After removing models that are poor fits, improve the remaining fits by transforming the best-fit solutions from magnitudes into flux densities and using linear regression to solve for first-order corrections.
3. After further removing models with low expected posterior probabilities, use Monte Carlo sampling to numerically integrate over the prior.
4. (Re)sample  $\theta$  and  $\phi$  from the estimated posterior.

Previous work such as STARHORSE Santiago et al. (2016); Queiroz et al. (2018); Anders et al. (2019) also use grids of parameters over stellar models to estimate  $\theta$  and  $\phi$ . The main differences between the approach taken in BRUTUS outlined above and those in many previous approaches are as follows:

1. *Parameter grids:* Many past approaches fit grids in both intrinsic  $\theta$  and extrinsic  $\phi$  stellar parameters. BRUTUS only requires grids in  $\theta$ , which are then used to generate continuous estimates for  $\phi$ .
2. *Variation in dust curves:* While many previous approaches can deal with variations in  $A_V$ , BRUTUS can model both variation in  $A_V$  and  $R_V$ .
3. *Flux density vs magnitude:* Previous approaches often compare models and data in magnitudes, which can cause issues for data with low signal-to-noise ratios (SNRs). BRUTUS fits performs better at lower SNR by comparing models and data in flux densities.

<sup>5</sup> <https://github.com/greggreen/dustmaps>

4. *Error modelling:* Some past approaches do not propagate certain aspects of measurement and/or model uncertainties when evaluating individual models. BRUTUS includes methods to explicitly try and model both.

A schematic illustration of our approach is shown in Figure 6. An example of the output stellar parameters and the associated SED can be seen in Figure 7. A detailed description can be found in §B. We find that for a typical source observed in  $\sim 8$  optical-to-NIR photometric bands with weak parallax constraints, BRUTUS is able to generate  $\sim 250$  samples from the posterior in  $\sim 5$  seconds for a grid of  $\sim 7.5 \times 10^5$  models. See §B.6 for additional discussion.

### 4. STELLAR AND EXTINCTION MODELS

While BRUTUS can in theory incorporate an arbitrary set of stellar and extinction models via a corresponding grid in  $\{\theta_i\}_{i=1}^{i=n} \rightarrow \{\theta_{*,i}\}_{i=1}^{i=n} \rightarrow \{\mathbf{M}_{\theta,i}, \mathbf{R}_{\theta,i}, \mathbf{R}'_{\theta,i}\}_{i=1}^{i=n}$ , it is currently designed to work with two models by default:

- The theoretical MESA Isochrone and Stellar Tracks (MIST) models (Choi et al. 2016) combined with the  $R_V$ -dependent extinction curve from (Fitzpatrick 2004).
- The empirical **Bayestar** models (Green et al. 2014, 2015; Zucker & Speagle et al. 2019) combined with the empirical  $R_V$ -dependent extinction curve from Schlafly et al. (2016).

We hope to incorporate additional models such as PARSEC (Bressan et al. 2012) and BPASS (Eldridge et al. 2017) in the future.

A comparison of the MIST and **Bayestar** models is shown in Figure 8. A detailed description of the MIST models and the corresponding pre-generated photometric grids in BRUTUS is provided in §4.1. A detailed description of the **Bayestar** models and the corresponding photometric grids in BRUTUS is provided in 4.2. All of the relevant data products described in this section are available online as part of the BRUTUS codebase.

#### 4.1. MIST

##### 4.1.1. Isochrones

The MESA Isochrone and Stellar Tracks (MIST) models are a set of theoretical isochrones built off of the Modules in Stellar Evolution (MESA; Paxton et al. 2011, 2013, 2015, 2018, 2019) codebase that connect intrinsic stellar evolutionary parameters  $\theta$  to physical surface-level parameters  $\theta_*$  as described in §2.1. A full description of the models can be found in (Choi et al. 2016). We utilize the MIST Version 1.2 *non-rotating* models com-

**Table 1.** Description of default priors and their corresponding hyper-parameters in BRUTUS based on Bland-Hawthorn & Gerhard (2016) and Xue et al. (2015). See §2.4 and §A for additional details.

Description	Symbol	Value	Description	Symbol	Value
<b>Initial Mass Function</b>					
Low-mass power law slope	$\alpha_1$	1.3	High-mass power law slope	$\alpha_2$	2.3
<b>3-D Stellar Number Density</b>					
Solar radius	$R_\odot$	8.2 kpc	Halo smoothing radius	$R_s$	1 kpc
Solar height	$Z_\odot$	0.025 kpc	Halo oblateness at $r = 0$	$q_0$	0.2
Thin disk scale radius	$R_{\text{thin}}$	2.6 kpc	Halo oblateness at $r = \infty$	$q_\infty$	0.8
Thin disk scale height	$Z_{\text{thin}}$	0.3 kpc	Halo scale radius	$r_q$	6 kpc
Thick disk scale radius	$R_{\text{thick}}$	2.0 kpc	Halo power law slope	$\eta$	4.2
Thick disk scale height	$Z_{\text{thick}}$	0.9 kpc	Halo fractional contribution at $R_\odot$	$f_{\text{halo}}$	0.005
Thick disk fractional contribution at $R_\odot$	$f_{\text{thick}}$	0.04			
<b>Stellar Metallicity</b>					
Thin disk mean metallicity	$\mu_{[\text{Fe}/\text{H}],\text{thin}}$	-0.2	Halo mean metallicity	$\mu_{[\text{Fe}/\text{H}],\text{halo}}$	-1.6
Thin disk metallicity scatter	$\sigma_{[\text{Fe}/\text{H}],\text{thin}}$	0.3	Halo metallicity scatter	$\sigma_{[\text{Fe}/\text{H}],\text{halo}}$	0.5
Thick disk mean metallicity	$\mu_{[\text{Fe}/\text{H}],\text{thick}}$	-0.7			
Thick disk metallicity scatter	$\sigma_{[\text{Fe}/\text{H}],\text{thick}}$	0.4			
<b>Stellar Age</b>					
Maximum age	$t_{\text{max}}$	13.8 Gyr	Thin disk mean age	$\mu_t,\text{thin}$	4.9 Gyr
Minimum age	$t_{\text{min}}$	0 Gyr	Thin disk age scatter	$\sigma_t,\text{thin}$	4 Gyr
Maximum age scatter	$\sigma_{\text{max}}$	4 Gyr	Thick disk mean age	$\mu_t,\text{thick}$	8.3 Gyr
Minimum age scatter	$\sigma_{\text{min}}$	1 Gyr	Thick disk age scatter	$\sigma_t,\text{thick}$	2.8 Gyr
Age-metallicity relation pivot	$\xi_{[\text{Fe}/\text{H}]}$	-0.5	Halo mean age	$\mu_t,\text{halo}$	12.4 Gyr
Age-metallicity relation scale-length	$\Delta_{[\text{Fe}/\text{H}]}$	0.5	Halo age scatter	$\sigma_t,\text{halo}$	1 Gyr
Standard deviation from maximum age	$n_\sigma$	2			
<b>3-D Dust Extinction</b>					
3-D $A_V$ mean	$\mu_A(d \ell, b)$	Bayestar19 mean	3-D $A_V$ scatter	$\Delta_A$	0.2 mag
3-D $A_V$ uncertainty	$\sigma_A(d \ell, b)$	Bayestar19 scatter			
<b>Dust Curve Variation</b>					
$R_V$ mean	$\mu_R$	3.32	$R_V$ scatter	$\sigma_R$	0.18

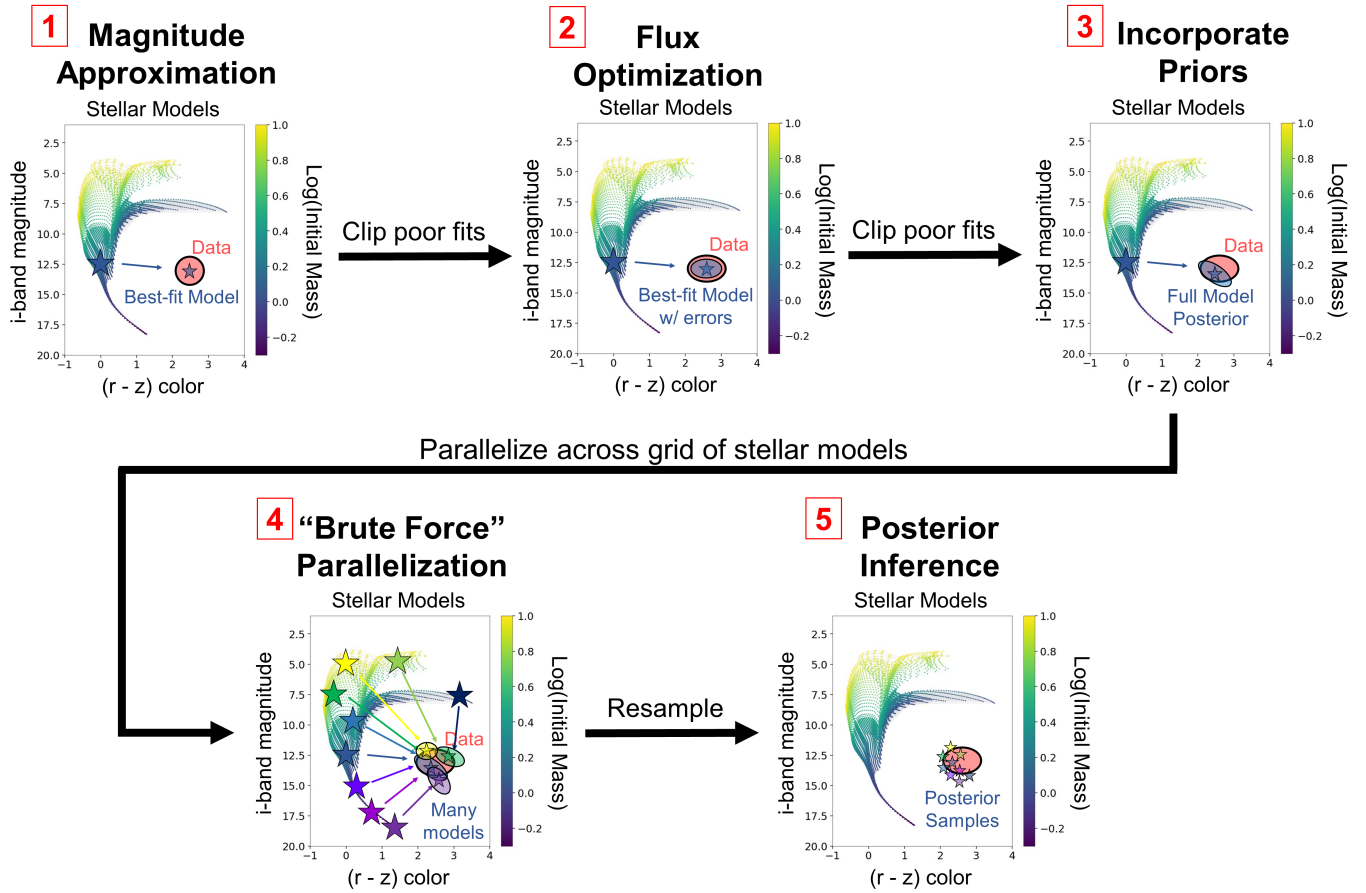


**Figure 6.** A schematic illustration of the approach BRUTUS takes to estimate stellar parameters across a  $b$ -band SED (only 3 are shown for visual clarity). First, BRUTUS constructs a “quick approximation” of the observed magnitudes (1, top left; see §B.6.1). After clipping poor fits, BRUTUS transforms the data to the native flux densities and conducts a limited optimization of the best-fit parameters (2, top middle; see §B.6.2). After clipping poor fits again using more stringent criteria, BRUTUS uses importance sampling to incorporate constraints from our priors (see §2.4) as well as any measured parallax (3, top right; see §B.6.3). These steps are processed in parallel across a grid of stellar models (4, bottom left) and subsequently resampled to approximately sample from the underlying posterior (5, bottom right; see §B.6.4). The whole process takes only a few seconds for a typical SED with  $b \sim 10$  bands and parallax measurements with low-to-moderate signal-to-noise ratios. See §3 for more details and Table 6 for a summary of important hyper-parameters.

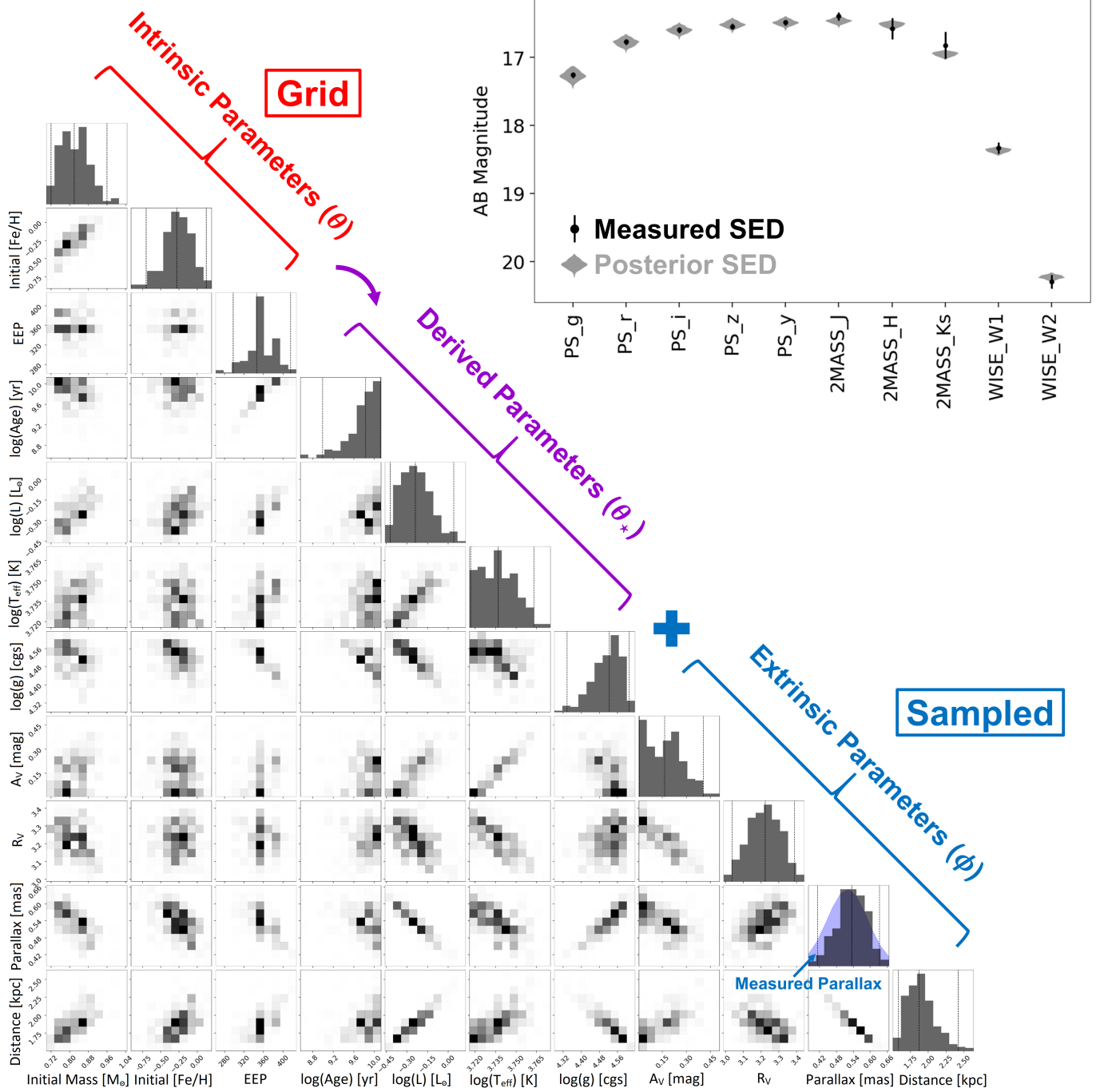


**Figure 7.** An example of parameters estimated from BRUTUS using the default priors (see §2.4) and setup (see §3 and Table 6) and the MIST models (see §4 and §5) for a real object observed in Pan-STARRS (PS), 2MASS, and WISE with a *Gaia* parallax measurement. The upper-right region shows the measured SED (black points) with the associated 2-sigma errors (black lines) along with SED realizations from the posterior (gray shaded regions). The lower-left region highlights the 1-D and 2-D marginalized posterior distributions estimated using the  $n_{\text{post}} = 250$  samples saved to disk with 10 evenly-spaced bins in each dimension, with the grayscale indicating the relative density of samples across the  $10 \times 10$  bins in each dimension. The labels, which are read in directly from the stellar model grid, correspond to the set of (gridded) intrinsic stellar parameters  $\theta$  and their derived surface-level stellar parameters  $\theta_*$  along with the (sampled) extrinsic parameters  $\phi$ . The astrometric constraints from the measured parallax alone are highlighted in light blue. Since the fits for each model  $\theta_i$  on the grid are done entirely in parallel, all correlations that emerge are a result of the posterior resampling process.

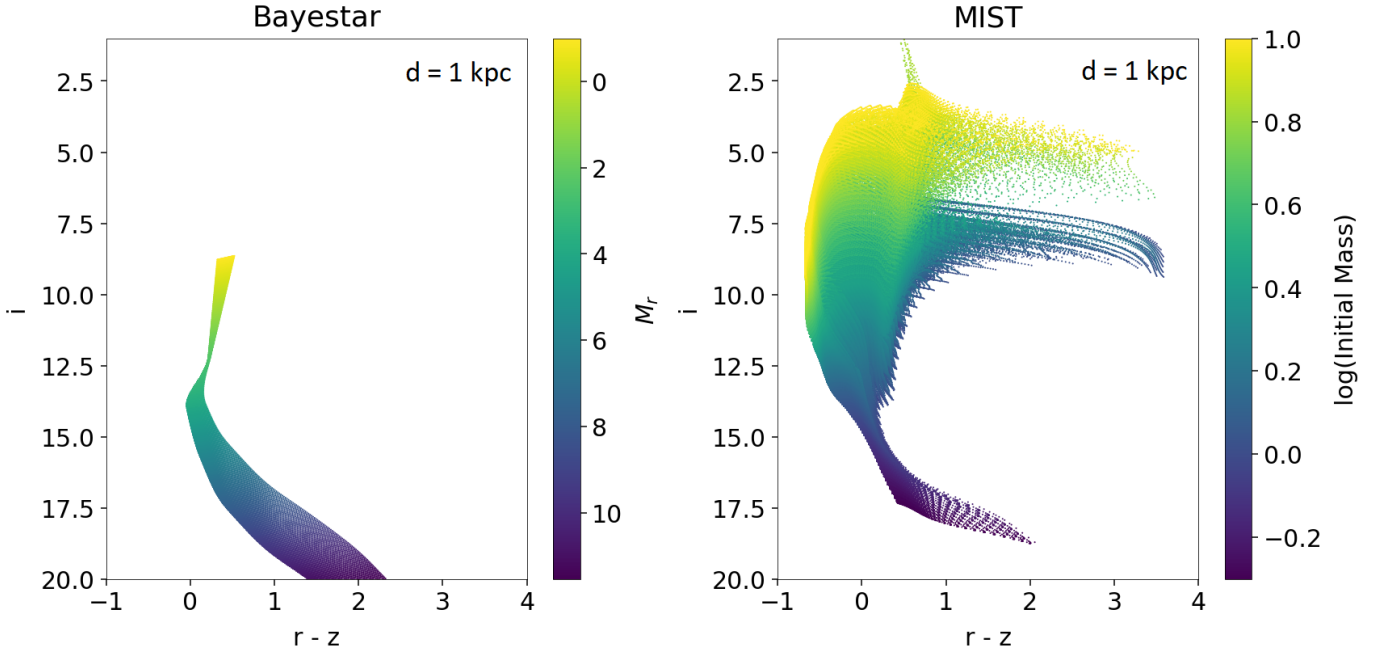


**Figure 8.** Color-magnitude diagrams (CMDs) in  $i$  magnitude (at 1 kpc) versus  $r-z$  color in the Pan-STARRS filters for **Bayestar** (`grid_bayestar_v5`, left) and **MIST** (`grid_mist_v8`, right) models, implemented by default in BRUTUS. The  $n \sim 4 \times 10^4$  empirical **Bayestar** models (see §4.2) are defined over a grid of metallicity values along with absolute Pan-STARRS  $r$ -band magnitudes  $M_r$  (left color scale), which serve as a rough proxy of intrinsic luminosity (and hence initial mass). The  $n \sim 7.5 \times 10^5$  theoretical **MIST** models (see §4.1), including the empirical corrections discussed in §5, are defined over a grid of ages, metallicities, and initial masses (right color scale). While the **Bayestar** models extend down to fainter intrinsic luminosity (lower initial mass) on the Main Sequence (MS; i.e. “dwarfs”), they only contain limited models at higher initial masses and little-to-no post-MS models (giants). They also are not calibrated outside a limited set of photometric bands. By contrast, while the **MIST** models are constrained to be above  $M_{\text{init}} \sim 0.5 M_{\odot}$  in this work (see §5), they include a wide variety of evolutionary phases and extend to higher initial masses.



puted over a grid of initial masses, initial metallicities, and ages as described on the MIST website<sup>6</sup>.

As described in Dotter (2016), since the timescale of stellar evolution is sensitive to the initial mass, different stars will reach different evolutionary phases at different times and over different timescales. As a result, it is advantageous to define a grid in *Equivalent Evolutionary Points* (EEPs) instead, which interpolate smoothly between particular stellar evolutionary states. While these have a monotonic relation with age, they are defined such that evolutionary phases where there are rapid changes to the surface or interior stellar properties are adequately captured in relevant evolutionary tracks and isochrone tables. EEPs can therefore be converted to ages  $t_{\text{age}}$  using associated lookup tables for a particular  $M_{\text{init}}$  and  $[\text{Fe}/\text{H}]_{\text{init}}$ . To account for the subsequent unequal spacing in age, the grid spacing  $\Delta_i$  for each model  $\theta_i$  for our MIST grid also includes the associated  $\Delta t_{\text{age},i}/\Delta \text{EEP}_i$  estimated at each EEP using central finite differences (which have errors at second order).

While the MIST models have been generally successful at reproducing stellar behavior across a wide range of masses, metallicities, and ages, we want to highlight two particular areas where more work is needed:

1. *Rotation*: Non-rotating stellar evolutionary tracks are used in this work for simplicity. This is a limitation since stars rotate, which can alter the relationship between age and EEP as well as the associated surface parameters  $\theta_*$ , especially around the Main Sequence turn-off for  $M_{\text{init}} > 1.2 M_{\odot}$  (see, e.g., Gossage et al. 2018). We note that this inevitably will introduce systematic uncertainties in any inferred stellar parameters (both  $\theta$  and  $\theta_*$ ).
2. *Abundance patterns*: The MIST models assume entirely solar-scaled abundance patterns. However, substantial populations of stars both in clusters and in the field display enhancement/depletion of  $\alpha$ -process elements (Ne, Mg, Si, S, Ar, Ca, and Ti) relative to the Sun (i.e.  $[\alpha/\text{Fe}] \neq 0$ ).  $[\alpha/\text{Fe}]$  variations can induce changes in the effective temperature on the order of  $\pm 100\text{K}$  that are somewhat degenerate with other effects such as changes in metallicity and intervening dust extinction (Dotter et al. 2007). These effects will be included in an upcoming suite of newer MIST models (Dotter et al. in prep.) and are not addressed in this work.

The 3-D grid over  $M_{\text{init}}$ ,  $[\text{Fe}/\text{H}]_{\text{init}}$ , and EEP we use for the MIST models is described in Table 2. This is adaptively spaced in  $M_{\text{init}}$  and defined in EEP to have coarser resolution on the Main Sequence (MS) (EEP = 202 – 454) and finer resolution on the post-MS (EEP >

**Table 2.** Default grid of parameters for the MIST models used in BRUTUS (`grid_mist_v8`). See §4.1 for additional details.

Minimum	Maximum	Spacing
<b>Initial Mass (<math>M_{\text{init}}</math>)</b>		
$0.5 M_{\odot}$	$2.8 M_{\odot}$	$0.02 M_{\odot}$
$2.8 M_{\odot}$	$3.0 M_{\odot}$	$0.1 M_{\odot}$
$3.0 M_{\odot}$	$8.0 M_{\odot}$	$0.25 M_{\odot}$
$8.0 M_{\odot}$	$10.0 M_{\odot}$	$0.5 M_{\odot}$
<b>Initial Metallicity (<math>[\text{Fe}/\text{H}]_{\text{init}}</math>)</b>		
–4.0	+0.5	0.06
<b>Equivalent Evolutionary Point (EEP)</b>		
202	454	12
454	808	6

454). It does not include any models on the pre-MS (EEP < 202) or at or beyond the start of the thermally-pulsing asymptotic giant branch (EEP > 808).<sup>7</sup>

We use linear interpolation to generate the corresponding grid over the surface-level parameters  $\{\theta_i\}_{i=1}^{i=n} \rightarrow \{\theta_{*,i}\}_{i=1}^{i=n}$ . After removing models with unphysical combinations of parameters (e.g., ages substantially exceeding the estimated current age of the Universe), we are left with a total of  $n \sim 7.5 \times 10^5$  models.<sup>8</sup> Cross-validation and hold-out tests over the original grid indicates interpolation errors can become significant ( $\gtrsim 10\%$ ) above  $2 M_{\odot}$ , but remain at the few percent level between  $0.5 M_{\odot}$  and  $2 M_{\odot}$ .

#### 4.1.2. Atmospheric Models

As in Cargile et al. (2020), we connect each model  $\theta_*$  to an underlying spectrum  $F_{\nu}(\lambda|\theta_*)$  using the C3K atmospheric models (C. Conroy, priv. comm.) given the predicted value of  $\theta_*(\theta)$  from linear interpolation and the relevant filter transmission curves (see §2.1). These synthetic spectra are calculated using the 1-D local thermodynamic equilibrium (LTE) plane-parallel

<sup>7</sup> See the MIST website and/or Dotter (2016) for additional information on the EEP definitions used in MIST.

<sup>8</sup> While BRUTUS allows for modeling additional unresolved binary components, internal testing found current systematic uncertainties (see §5) are too large to infer meaningful quantities for many individual stars. This feature is therefore disabled by default.

<sup>6</sup> <http://waps.cfa.harvard.edu/MIST/>

atmosphere and radiative transfer codes ATLAS12 and SYNTHE maintained by R. Kurucz (Kurucz 1970; Kurucz & Avrett 1981; Kurucz 1993). The line list used in the radiative transfer calculations was provided by R. Kurucz (private communication) after being empirically tuned to the observed, ultra-high resolution spectra of the Sun and Arcturus (Cargile et al. in prep). The micro-turbulence is assumed to be constant with a velocity of  $v_{\text{micro}} = 1 \text{ km s}^{-1}$ . The C3K atmosphere models have been shown to reproduce the observed relationship between color- $T_{\text{eff}}$  relations for all but the very lowest mass stars (i.e. M dwarfs) at the few percent level in  $T_{\text{eff}}$ .

The C3K atmosphere models are originally constructed over a 4-D grid in effective temperature  $T_{\text{eff}}$ , surface gravity  $\log g$ , surface metallicity  $[\text{Fe}/\text{H}]_{\text{surf}}$ , and surface  $\alpha$ -abundance enhancement  $[\alpha/\text{Fe}]_{\text{surf}}$  over an adaptive grid as outlined in Table 3. This includes a total of  $n = 26561$  models after removing unphysical combinations of parameters. Since the current MIST models only use solar-scaled abundance patterns, when predicting spectra and/or photometry BRUTUS always sets  $[\alpha/\text{Fe}]_{\text{surf}} = 0$  by default.

#### 4.1.3. Dust Extinction Curve

To incorporate the impact of dust extinction, we add two dimensions to the C3K atmospheric model grid in both  $A_V$  and  $R_V$  based on the  $R_V$ -dependent dust extinction curve from Fitzpatrick (2004). This dust curve has been shown to accurately reproduce detailed observations from spectra and photometry in the optical and NIR (Fitzpatrick 2004; Schlafly et al. 2016). The associated grid in  $A_V$  and  $R_V$  is shown in Table 3. The final 6-D grid contains  $n \sim 6.4 \times 10^5$  models.

#### 4.1.4. Photometry

Photometry is computed from each synthetic spectrum for a large set of photometric systems derived from various imaging surveys. This currently includes:

- Pan-STARRS:  $g$ ,  $r$ ,  $i$ ,  $z$ ,  $y$ ,  $w$ , and  $w_{\text{open}}$ .
- DECam:  $u$ ,  $g$ ,  $r$ ,  $i$ ,  $z$ , and  $Y$ .
- Bessel:  $U$ ,  $B$ ,  $V$ ,  $R$ , and  $I$ .
- 2MASS:  $J$ ,  $H$ , and  $K_s$ .
- UKIDSS:  $Z$ ,  $Y$ ,  $J$ ,  $H$ , and  $K$ .
- WISE:  $W_1$ ,  $W_2$ ,  $W_3$ , and  $W_4$ .
- *Gaia*:  $G$ ,  $BP$ , and  $RP$ .
- *Tycho*:  $B$  and  $V$ .
- *Hipparcos*:  $H_p$ .
- *Kepler*:  $D_{51}$  and  $K_p$ .

**Table 3.** Grid of parameters for the C3K stellar atmosphere models used in BRUTUS. See §4.1 for additional details. Dust extinction is incorporated using the  $R_V$ -dependent dust curve from Fitzpatrick (2004).

Minimum	Maximum	Spacing
<b>Effective Temperature (<math>T_{\text{eff}}</math>)</b>		
2500 K	50000 K	200 K – 10000 K
<b>Surface Gravity (<math>\log g</math>)</b>		
-1.0	5.0	0.5
<b>Surface Metallicity (<math>[\text{Fe}/\text{H}]_{\text{surf}}</math>)</b>		
-4.0	-3.0	0.5
-3.0	+0.5	0.25
<b>Surface <math>\alpha</math> Abundance (<math>[\alpha/\text{Fe}]_{\text{surf}}</math>)</b>		
-0.2	+0.6	0.2
<b>Dust Extinction (<math>A_V</math>)</b>		
0.0	5.0	1.0
<b>Dust Curve Variation (<math>R_V</math>)</b>		
2.0	5.0	1.0

- *TESS*:  $w_{\text{TESS}}$ .

Note that the *Gaia* filter curves and zeropoints are computed using the DR2 photometric calibrations from Evans et al. (2018) and Maíz Apellániz & Weiler (2018). For the *BP* filter, where the behavior on the bright and faint end substantially differ, we have opted to utilize the “faint” version of the filter curve. See Choi et al. (2016) and the MIST website for additional discussion on the filters, photometric systems, and corresponding “zero-points”. We will return to some of these in §5.

To generate photometry in a given band  $M_i(\theta_*, A_V, R_V)$ , we need to both integrate each model over the corresponding filter transmission curve  $T_b(\lambda)$  and interpolate over the corresponding 6-D grid. While the former operation is straightforward, the latter is slightly more difficult due to the larger dimensionality

of our grid and smooth (but non-linear) behavior in the synthetic spectra as a function of our parameters.

As discussed in Ting et al. (2019), the use of artificial neural networks (NNs) to predict synthetic spectra (and in our case photometry) has advantages over other interpolation methods. We train a multi-layered feed-forward NN using PYTORCH over the 6-D grid of normalized photometry after integrating the synthetic spectra over each filter transmission curve. We use the same architecture and training procedure described in Cargile et al. (2020). Briefly, our network has 4 layers (2 hidden layers) with 64 neurons per layer and sigmoid activation functions. Training is performed using adaptive cross-validation procedures over regular epochs and where the density of models are increased where the network’s predictions are the least accurate. The predicted magnitudes have a mean square error (MSE) of  $\sim 0.01$  mag over both the training data and a subset of hold-out test data. This is below the level of known systematic uncertainties in the MIST models (Choi et al. 2016) and seen in §5.

#### 4.1.5. Linear Reddening Approximation

As described in §2.1, we need to approximate the impact of dust extinction through the use of a linear reddening vector  $\mathbf{R}_\theta$  and differential reddening vector  $\mathbf{R}'_\theta$  over our filter curves. As expected, we find that for large changes in  $A_V$  and  $R_V$  the corresponding change in magnitudes is not fully described by a single linear vector but requires additional polynomial terms in both parameters. While this will impact the “absolute” inferred  $A_V$  and  $R_V$ , it is consistent both with the definition of  $E(B - V) \rightarrow A_V$  from the 3-D dust map of Green et al. (2019) (henceforth Bayestar19) and of  $R_V$  from Schlafly et al. (2016) and Schlafly et al. (2017).

The details of our approximation are described in §C. Overall, we find agreement at the few percent level across a wide range of  $A_V$  and  $R_V$  values.

## 4.2. Bayestar

### 4.2.1. Stellar Models

As described in Green et al. (2014, 2015), the Bayestar stellar models are obtained by fitting a stellar locus in 7-D color space in the Panoramic Survey Telescope and Rapid Response System (Pan-STARRS; Chambers et al. 2016) *grizy* and Two Micron All Sky Survey (2MASS; Skrutskie et al. 2006) *JHK<sub>s</sub>* bands following the procedure described in Newberg & Yanny (1997). These are derived from  $\sim 1$  million stars with detections in all bands, estimated magnitude errors of  $< 0.5$  mag, and estimated dust extinction  $E(B - V) < 0.01$  based on the 2-D integrated dust map from Schlegel et al. (1998). The photometry is then “de-reddened” by assuming all stars have the same reddening vector (i.e.  $\mathbf{R}_\theta = \mathbf{R}$ ), where  $\mathbf{R}$  is estimated from a  $T_{\text{eff}} = 7000$  K solar-metallicity source spectrum at  $E(B - V) = 0.4$  mag

using the extinction curve from Cardelli et al. (1989) with  $R_V = 3.1$ .

Once this 7-D locus has been derived, metallicity-dependent absolute magnitudes  $\mathbf{M}_\theta$  are obtained using the metallicity-dependent photometric parallax relation given in Ivezić et al. (2008). This makes the Bayestar stellar models primarily dependent on only two parameters: the absolute magnitude  $M_r$  in the Pan-STARRS *r*-band and the “metallicity”  $[\text{Fe}/\text{H}]$  of the star. The locus is extended artificially to lower stellar masses (fainter  $M_r$ ) using the prescription outlined in Green et al. (2014).

Since this fitting is done exclusively in color space, it is not sensitive to evolved giants with nearly-identical colors as MS stars (i.e. “dwarfs”). As a result, giant templates from Ivezić et al. (2008), derived from linear fits to globular cluster color-magnitude diagrams (CMDs), are “grafted” onto the stellar locus based on their corresponding *r*–*i* color. While these templates are quite limited relative to the diverse evolutionary states included in the MIST models (see Figure 8), they still capture basic features of the dwarf-giant degeneracy.

Since these templates are only defined based on specific photometric bands and are not connected to any underlying stellar spectra, they cannot be easily extended to other bands. Currently, they are only supported in the DECam, Pan-STARRS, and 2MASS system (Green et al. 2014, 2015; Zucker & Speagle et al. 2019).

### 4.2.2. Dust Extinction Curve

For the Bayestar models, we follow the approach taken in Green et al. (2014) and subsequent work by assuming the reddening vector is again both linear and constant for all models such that  $\mathbf{R}_\theta = \mathbf{R}$ . As in Green et al. (2019), we take this reddening vector to be the empirical reddening vector derived from Schlafly et al. (2016) re-normalized to scale with  $A_V$  as described in Zucker & Speagle et al. (2019). Similarly, we also assume that the differential reddening vector is the same for all models such that  $\mathbf{R}'_\theta = \mathbf{R}'$ , where  $\mathbf{R}'$  is again derived from Schlafly et al. (2016).

As with the empirical stellar models, it is also difficult to extend these results to other photometric systems without constraints on the underlying dust extinction curve. Schlafly et al. (2016), however, do provide a simple functional form for the dust curve that reproduces the observational constraints for a particular stellar spectrum. This was used in Zucker & Speagle et al. (2019) to (re-)derive  $\mathbf{R}$  and  $\mathbf{R}'$  in the DECam, Pan-STARRS, and 2MASS photometric system.

### 4.2.3. Priors

While we have used the same notation  $\theta$  to refer to the intrinsic parameters for both the MIST and Bayestar models, the Bayestar models do not have age  $t_{\text{age}}$  or initial mass  $M_{\text{init}}$  estimates. As a result, inference over these models does not incorporate

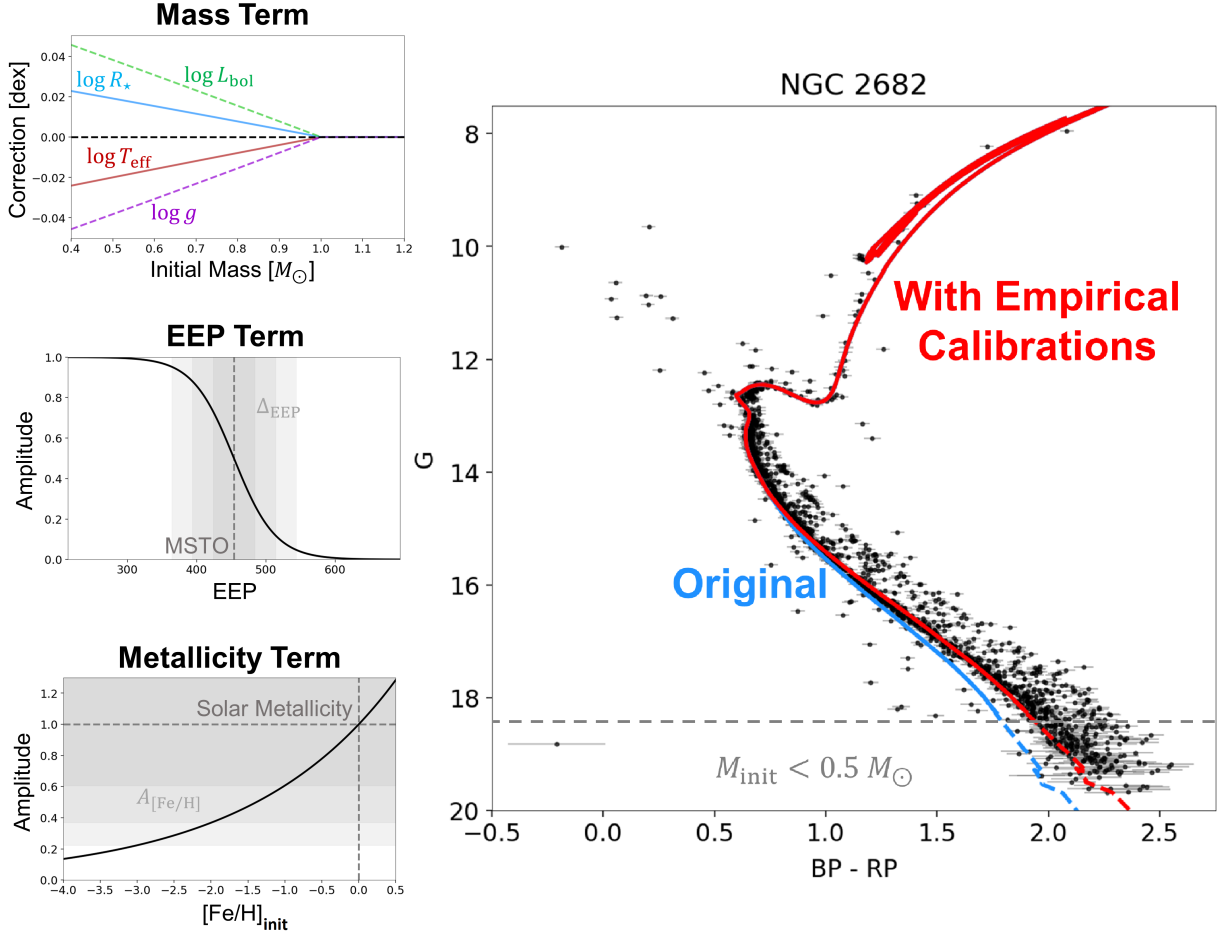


**Figure 9.** An illustration of the components used in our empirical MIST isochrone corrections. The top left panel shows the underlying corrections, which we take to be linear adjustments in  $\log R_*$  (solid blue) and  $\log T_{\text{eff}}$  (solid red) as a function of initial mass, with no corrections above  $M_{\text{init}} = 1 M_{\odot}$ . These then propagate to corrections in  $\log g$  (dashed purple) and  $\log L_{\text{bol}}$  (dashed green) at fixed  $T_{\text{eff}}$ . The middle left panel shows the function used to suppress the overall amplitude of these corrections near the Main Sequence turn-off (MSTO) as a function of EEP, with intervals of the suppression scale  $\Delta_{\text{EEP}}$  highlighted with shaded grey regions. The bottom left panel shows the function used to modify the overall amplitude as a function of initial metallicity relative to  $[\text{Fe}/\text{H}]_{\text{init}} = 0$ , with intervals of the  $e$ -folding amplitude  $e^{A_{[\text{Fe}/\text{H}]}}$  highlighted with shaded grey regions. The combined effect these have on a specific isochrone is shown in the *Gaia*  $G$  versus  $BP - RP$  color-magnitude diagram of NGC 2682 (i.e. M67) on the right, with the data shown in black, the original isochrone in blue, and the isochrone after applying these corrections in red. The approximate location where  $M_{\text{init}} < 0.5 M_{\odot}$  is indicated with a dashed grey line (see Figure 11). The overall shape and behavior of the isochrone displays much better agreement with the data, especially at lower masses, while the behavior near and beyond the MSTO remains relatively unchanged. See §5.1 and §D.4 for additional details.

our age prior  $\pi(t_{\text{age}}|d, \ell, b)$  or IMF prior  $\pi(M_{\text{init}})$ . Instead, the **Bayestar** models are subject to a luminosity function prior  $\pi(M_r)$  taken from Green et al. (2014). This is derived by computing the luminosity function  $\pi(M_r|[\text{Fe}/\text{H}], t_{\text{age}})$  for a particular metallicity  $[\text{Fe}/\text{H}]$  and age  $t_{\text{age}}$  based on the PARSEC models (Bressan et al. 2012) assuming a Chabrier (2003) IMF and then marginalizing over  $[\text{Fe}/\text{H}]$  and  $t_{\text{age}}$  such that

$$\pi(M_r) = \int \pi(M_r|[\text{Fe}/\text{H}], t_{\text{age}}) \pi([\text{Fe}/\text{H}], t_{\text{age}}) d[\text{Fe}/\text{H}] dt_{\text{age}} \quad (19)$$

where the prior over  $[\text{Fe}/\text{H}]$  and  $t_{\text{age}}$  is the product of two independent Normal distributions

$$\pi([\text{Fe}/\text{H}], t_{\text{age}}) = \mathcal{N} \left[ \mu_{[\text{Fe}/\text{H}]}, \sigma_{[\text{Fe}/\text{H}]}^2 \right] \times \mathcal{N} \left[ \mu_t, \sigma_t^2 \right] \quad (20)$$

given  $\mu_{[\text{Fe}/\text{H}]} = -0.5$ ,  $\sigma_{[\text{Fe}/\text{H}]} = 0.5$ ,  $\mu_t = 7$  Gyr, and  $\sigma_t = 2$  Gyr. The resulting  $\pi(M_r)$  prior is tabulated over a large grid of  $M_r$  values that is provided as part of the BRUTUS package.

## 5. EMPIRICAL CALIBRATION OF MIST ISOCHRONES



Unlike the *Bayestar* models, which are derived directly from data, the MIST models (both the underlying MIST V1.2 isochrones and the atmospheric C3K models) have known systematic offsets in predicted stellar properties  $\theta_*$  and observed photometric flux densities  $\mathbf{F}$  over particular sets of intrinsic parameters  $\theta$  (Choi et al. 2016). This is particularly acute for, e.g., the very broad *Gaia* filters. These systematics can also become pronounced at lower stellar masses ( $M_{\text{init}} \lesssim 0.75$ ), where the impact of stellar activity, magnetic fields, convection, and molecular absorption features, among others, become increasingly important.

To ameliorate some of these differences, we develop limited empirical calibrations for the MIST models described above. The corrections and models are available as part of the BRUTUS package.

We perform these calibrations in two steps. First, we utilize a set of “benchmark” open clusters to calibrate mass-dependent and metallicity-dependent offsets in predicted surface properties from the MIST isochrones as well as a series of preliminary photometric offsets. Afterwards, we validate and refine our photometric offsets using a large population of nearby, high-latitude, low-reddening field stars with good parallax measurements.

We provide an overview of our empirical corrections in §5.1 and illustrate them in Figure 9. Our calibration using over a set of “benchmark” open clusters is described in §5.2 and illustrated in Figure 10. Our calibration with field stars is described in §5.3.

Additional details describing our cluster model can be found in §D.

### 5.1. Overview of Empirical Corrections

We use a series of *empirically-motivated corrections* to address systematic modeling issues derived from the use of theoretical isochrones such as MIST and synthetic spectra such as C3K. These change the output surface-level parameters of a star to a “corrected” version  $\theta_*(\theta) \rightarrow \theta'_*(\theta_*, \theta)$  as a function of the original predicted surface-level parameters  $\theta_*$  as well as the underlying stellar evolution parameters  $\theta$  from the MIST isochrones. In particular, we opt to modify the stellar radius  $\log R_*$  and the effective temperature  $\log T_{\text{eff}}$  (and by proxy the surface gravity  $\log g$  and bolometric luminosity  $\log L_{\text{bol}}$ ) such that

$$\begin{bmatrix} M_{\text{init}} \\ [\text{Fe}/\text{H}]_{\text{init}} \\ t_{\text{age}} \end{bmatrix} \rightarrow \begin{bmatrix} \log g \\ \log T_{\text{eff}} \\ \log L_{\text{bol}} \\ \log R_* \\ [\text{Fe}/\text{H}]_{\text{surf}} \end{bmatrix} \rightarrow \begin{bmatrix} \log g' \\ \log T'_{\text{eff}} \\ \log L'_{\text{bol}} \\ \log R'_* \\ [\text{Fe}/\text{H}]_{\text{surf}} \end{bmatrix} \rightarrow \begin{bmatrix} M_1 \\ \vdots \\ M_b \end{bmatrix}$$

We choose to apply empirical corrections to  $\log R_*$  and  $\log T_{\text{eff}}$  for two reasons:

1. We expect both to be strongly affected by magnetic fields (which are not included in MIST), which

**Table 4.** A summary of the parameters used to apply the empirical MIST isochrone corrections used in BRUTUS. See §D for additional details.

Description	Symbol	Value
Slope of $M_{\text{init}}$ -dependent $T_{\text{eff}}$ correction	$c_T$	+0.09
Slope of $M_{\text{init}}$ -dependent $R_*$ correction	$c_R$	−0.09
Scale of EEP suppression	$\Delta_{\text{EEP}}$	30
Amplitude of [Fe/H] suppression	$A_{[\text{Fe}/\text{H}]}$	0.5

appear to “puff up” stars (making them larger) and contribute to sunspot activity (making them cooler), especially at lower masses (Berdyugina 2005; Somers & Pinsonneault 2015; Somers et al. 2020).

2. Detailed modeling of binaries already suggests that the MIST models deviate slightly from the observations in these two parameters (Choi et al. 2016).

To keep our empirical corrections as simple as possible, we only introduce corrections for masses below  $M_{\text{init}} = 1 M_{\odot}$  and “suppress” the effects of our derived corrections after stars evolve off the MS (i.e. after stars have EEP > 454) and for sub-solar metallicities (where the fits are relatively unconstrained; see §5.2). We further assume that our corrections only involve a single parameter,  $M_{\text{init}}$ , and that they are fully linear<sup>9</sup> with slopes  $c_R$  and  $c_T$  for  $\log R_*$  and  $\log T_{\text{eff}}$ , respectively. We suppress effects for evolved stars<sup>10</sup> over a scale of  $\Delta_{\text{EEP}}$  and for sub-solar metallicities with an amplitude of  $A_{[\text{Fe}/\text{H}]}$ . Effects are then propagated to other parameters such as  $\log g$  and  $\log L_{\text{bol}}$  in a self-consistent manner.

An illustration of the functional forms used for the corrections themselves is shown in Figure 9. See Table 4 for a summary of the parameters used to model empirical corrections used in this work and their final set of values. We find that the overall empirical corrections substantially improve behavior down to  $M_{\text{init}} \sim 0.5 M_{\odot}$ , which can be seen more clearly in Figure 11.

In addition to these isochrone-oriented corrections, we also fit for a set of *photometric offsets* to account for slightly different photometric calibrations between the synthetic photometry computed from models versus the real photometry from surveys or issues with the C3K stellar atmosphere models. We model these offsets explicitly

<sup>9</sup> While we experimented with more complex functional forms, we found that there was not enough data to warrant using them.

<sup>10</sup> While there are known disagreements between the MIST models and observations for post-MS stellar evolutionary phases (Choi et al. 2016), investigating them is beyond the scope of this work.



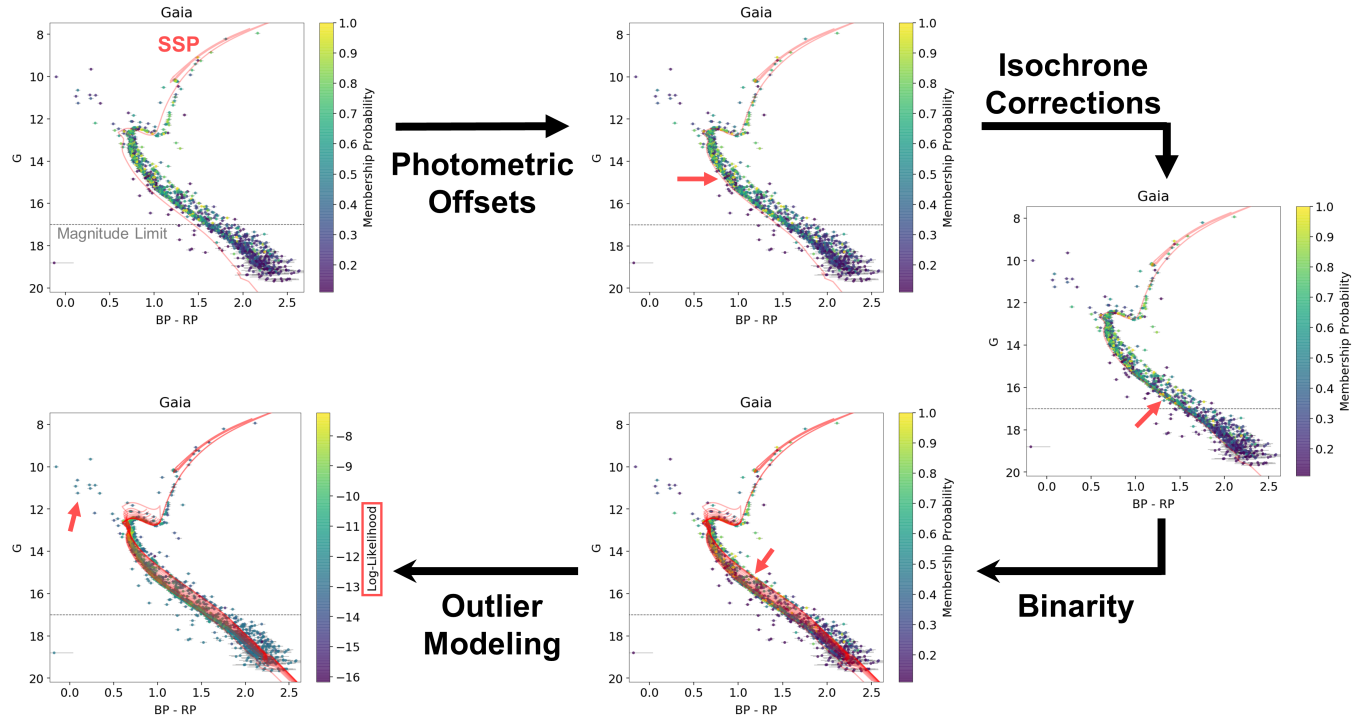


**Figure 10.** An illustration of the components in the cluster model we use as part of our empirical calibration of the MIST models, highlighting data from NGC 2682 (i.e. M67; see Figure 11). A total of six clusters were used. The baseline component is a simple stellar population (SSP; top left), which we integrate over for every single source for a given set of cluster parameters  $\theta_{\text{cluster}}$  such as age and metallicity. We then add in a set of empirical “corrections” including overall photometric offsets (top middle) and mass-dependent luminosity and temperature shifts (right) that adjust the SSP model to better match the data (see Figure 9). We then integrate over possible contributions from unresolved binaries (bottom middle) with unknown secondary companion masses. Finally, we use information on cluster membership from astrometric measurements from *Gaia* DR2 along with mixture modeling to compute robust likelihoods (bottom left). This is done simultaneously over all sources and in all bands, allowing us to leverage the full SED for each source along with corresponding parallax measurements. See §D for additional details.

by introducing a set of scale-factors  $\mathbf{s}_{\text{em}} = \{s_{\text{em},i}\}_{i=1}^{i=b}$  that simply rescale the *data* such that the new flux density  $\hat{F}'_{i,j}$  for a given star  $i$  in band  $j$  is

$$\hat{F}'_{i,j} = s_{\text{em},j} \times \hat{F}_{i,j} \quad (21)$$

We are able to do so thanks to the large number of available parallax measurements from *Gaia* DR2 that give independent constraints on the distance, thereby fixing not just offsets in color but offsets in absolute magnitude.

The impact these two sets of empirical corrections have on our cluster model is shown in the fourth and fifth panels of Figure 10.

### 5.2. Calibration with “Benchmark” Clusters

The full cluster model (§D) includes both cluster-level parameters  $\theta_{\text{cluster}}$  and the empirical correction terms described in §5.1. While typically we would be interested in inferring  $\theta_{\text{cluster}}$ , in this work we are instead interested in constraining the empirical correction parameters  $c_T$ ,  $c_R$ , and  $\mathbf{s}_{\text{em}}$  that modify the MIST models. We

estimate these parameters by marginalizing over  $\theta_{\text{cluster}}$  based on fits to a series of “benchmark” clusters. To do this, we use the three-step approach:

1. Use optimization methods to compute the maximum-likelihood estimate (MLE) for  $\theta_{\text{cluster}}$ ,  $c_T$ ,  $c_R$ , and  $\mathbf{s}_{\text{em}}$  for each cluster, allowing all parameters to vary.
2. Fix  $c_T$  and  $c_R$  to be roughly the median value across all of the benchmark clusters, then re-optimize the results starting from the previous MLE.
3. Fix  $\mathbf{s}_{\text{em}}$  to be the roughly the median value across all of the benchmark clusters, the re-optimize the results starting from the previous MLE.

We perform this iterative conditional optimization using a combination of Powell’s method (Powell 1964) and Nelder-Mead (Nelder & Mead 1965) implemented within the OPTIMIZE.MINIMIZE routine in SCIPY (Virtanen et al. 2020). To avoid being biased by difficulties

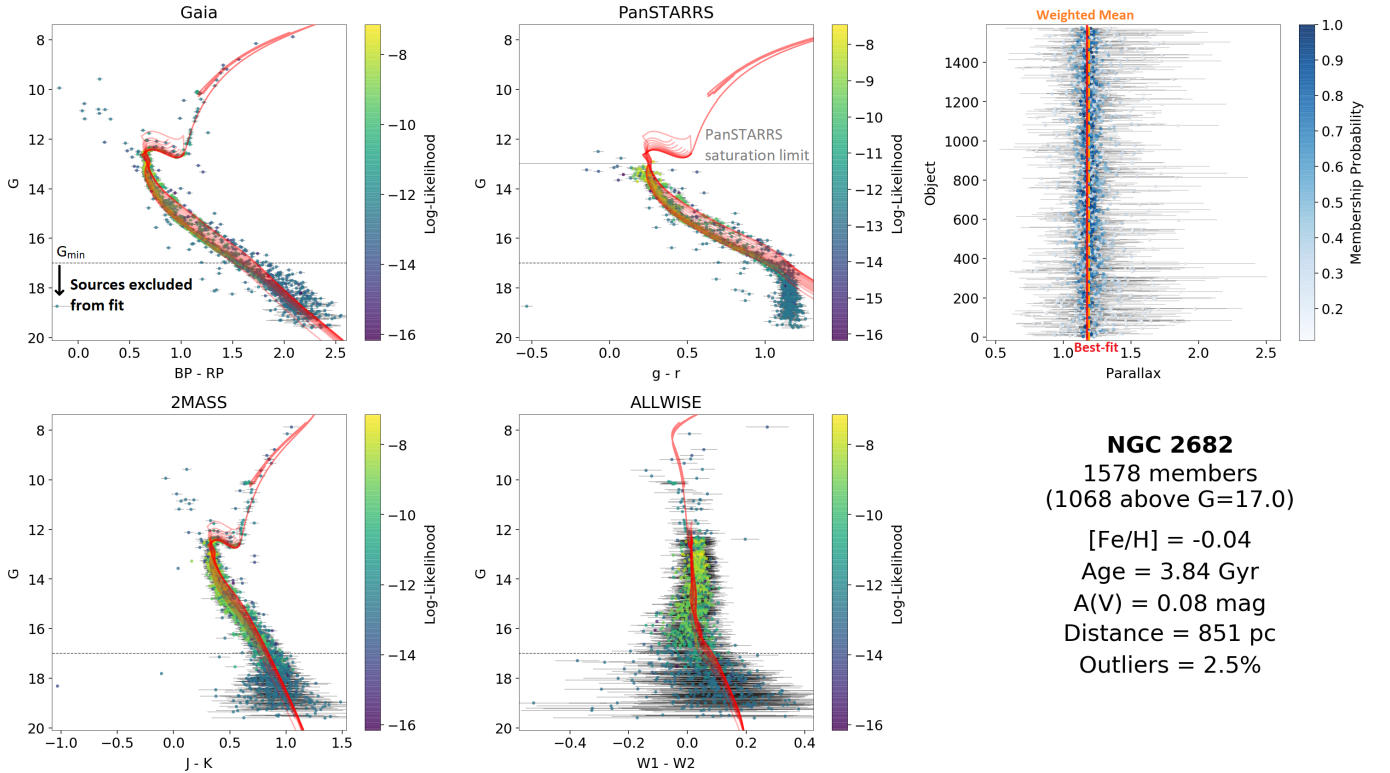


**Figure 11.** Our best-fit cluster model (see §D) to *Gaia* DR2, Pan-STARRS, 2MASS, and AllWISE data for NGC 2862 (i.e. M67) for all stars with  $G > 17.0$  (horizontal dashed black line). Color-magnitude diagrams (CMDs) for the sources associated with the cluster are shown in the left four panels. Points are colored according to their log-likelihoods with respect to our best-fit model, whose associated isochrone tracks are overplotted in red. The parallax measurements for the individual sources, colored according to their membership probability, are shown in the top right along with the weighted mean (dashed orange line) and best-fit distance (solid red). A summary of the best-fit parameters are shown on the bottom right. We see that the overall model is a good fit to the SED overall, capturing the behavior across the MS and post-MS down to  $G_{\min} = 17$  ( $M_{\text{init}} \sim 0.5 M_{\odot}$ ), and that the outlier model does a good job of reducing the contribution of the small ( $\approx 2.5\%$ ) percentage of outlying sources such as blue stragglers (top left area of CMDs). The values for the age, metallicity, and  $A(V)$  are in excellent overall agreement with measurements from the literature.

modeling low-mass sources, for each cluster we impose a *Gaia* DR2  $G$ -band cutoff  $G_{\min}$  below which no sources are included in the fit.

The data we use to perform this calibration come from six open clusters: NGC 2548 (M48), NGC 752, NGC 188, NGC 2632 (Praesepe), NGC 2682 (M67), and NGC 3532. The reasons for choosing these particular open clusters are as follows:

- *Well-studied:* Each cluster has been the subject of numerous studies and has reasonably well-known literature values of the overall metallicity, age, and distance, often validated using multiple methods.
- *Wavelength coverage:* With the exception of NGC 3532 (which does not have Pan-STARRS coverage), all clusters have photometry and astrometry measurements from *Gaia* DR2 and photometry from Pan-STARRS, 2MASS, and AllWISE. The long wavelength range is crucial for disentangling

the relative impacts of dust compared to those expected from our empirical corrections.

- *Metal-rich:* Because models of evolved stars on the horizontal giant branch at lower metallicities are unreliable, all clusters are required to have  $[Fe/H]_{\text{init}} \sim 0$ . We hope to extend our sample down to lower metallicities and improve upon our outlier modelling in future work.

Cluster membership probabilities  $p_{\text{mem},i}$  were assigned using the Hierarchical Density-Based Spatial Clustering of Applications with Noise (HDBSCAN) algorithm (Campello et al. 2013; McInnes et al. 2017; McInnes & Healy 2017) using proper motion and parallax measurements from *Gaia* DR2. Photometry was taken from Pan-STARRS, 2MASS, and AllWISE (Cutri & et al. 2013) surveys and cross-matched using Pan-STARRS as the primary catalogue within a 0.5 arcsecond radius. All

photometric errors had 0.02 mags added in quadrature to account for possible systematic effects (see also §5.3).

The final fit to NGC 2682 (M67) is shown in Figure 11 to illustrate the overall quality of our results. The fits to the remaining five clusters are shown in §E. The final set of empirical isochrone corrections are listed in Table 4 while the final set of empirical photometric offsets are listed in Table 5. We find the resulting temperature and radius offsets agree well with observations from binary systems presented in Choi et al. (2016). When we subsequently discuss the MIST models, the assumption should be that these isochrone-level corrections have already been applied unless explicitly stated otherwise.

### 5.3. Calibration with “Benchmark” Field Stars

While the overall behavior of the empirical isochrone corrections was somewhat stable across clusters, we found there was substantially more variation in the fitted photometric offsets  $\mathbf{s}_{\text{em}}$  from cluster to cluster. This led us to develop an independent pipeline to derive and validate photometric offsets between the MIST models and the data using a sample of nearby, low-reddening stars with high signal-to-noise parallax measurements.

The idea behind this method is straightforward. If a star has very precise parallax measurements, there is not much allowed variation in the overall distance. The overall lack of dust also guarantees a fairly accurate measure of the underlying luminosity. Taken together, we thus expect that any photometric offsets between the model and the data must be primarily due to  $\mathbf{s}_{\text{em}}$ . While this measurement will be noisy for any individual source and likely vary as a function of  $\theta$ , averaging over a large enough number of sources allows us to estimate  $\mathbf{s}_{\text{em}}$  robustly. Details on this procedure can be found in §F.

We apply this overall procedure to a set of field stars selected using the following criteria:

- $|b| > 60^\circ$ : High Galactic latitude to avoid crowding and dust.
- $E(B - V) < 0.2$  mag: Low total line-of-sight reddening, as estimated from the Schlegel et al. (1998) dust map.
- $\hat{\omega}/\sigma_{\hat{\omega}} > 50$ : Extremely high signal-to-noise parallax measurements to ensure absolute distances are essentially fixed.
- *Full photometric coverage*: We require all sources have detections in *Gaia*, Pan-STARRS, 2MASS, and AllWISE.
- $M_{\text{init}} > 0.55 M_{\odot}$ : We require all sources to have initial masses that are sufficiently away from the low edge of our mass grid ( $M_{\text{init}} = 0.5 M_{\odot}$ ). Using the MIST models, we approximate this to be the case when  $G < -0.052 \times (BP - RP)^2 + 1.88 \times (BP - RP) + 4.97$ , where  $G$  is the *absolute Gaia*

**Table 5.** A summary of the photometric offsets (see §D.5) derived for the empirical MIST isochrone corrections used in BRUTUS along with the estimated systematic uncertainties in the models. See §5.2 and §5.3 for additional details on the values derived using open clusters and high-latitude field stars, respectively. Note that the field values (highlighted in bold) are the ones implemented by default. We find offsets/uncertainties of roughly 2% uncertainties in the optical, 3% in the NIR, and 4% in the IR.

Filter	Value (Cluster)	Value (Field)	Uncertainty
<i>Gaia</i> DR2 <sup>a</sup>			
<i>G</i>	1.03	<b>1.01</b>	0.02
<i>BP</i>	1.05	<b>1.02</b>	0.02
<i>RP</i>	1.00	<b>0.97</b>	0.02
Pan-STARRS			
<i>g</i>	1.03	<b>1.01</b>	0.02
<i>r</i>	0.96	<b>0.97</b>	0.02
<i>i</i>	0.98	<b>0.97</b>	0.02
<i>z</i>	0.99	<b>0.96</b>	0.02
<i>y</i>	1.00	<b>0.97</b>	0.02
2MASS			
<i>J</i>	1.00	<b>0.99</b>	0.03
<i>H</i>	1.04	<b>1.04</b>	0.03
<i>K<sub>s</sub></i>	1.02	<b>1.04</b>	0.03
WISE			
<i>W1</i>	1.02	<b>1.02</b>	0.04
<i>W2</i>	1.07	<b>1.03</b>	0.04

<sup>a</sup>Offsets were derived using the latest *Gaia* DR2 filter curves from Maíz Apellániz & Weiler (2018). They shift by  $\sim 0.03$  mag when using previously published filter curves.

*G*-band magnitude estimated using the measured parallax.

This leaves us with a sample of  $n = 22933$  stars. Their distribution in the *Gaia* *G* versus  $BP - RP$  CMD is shown in Figure 12. The resulting photometric offsets are listed in Table 5.

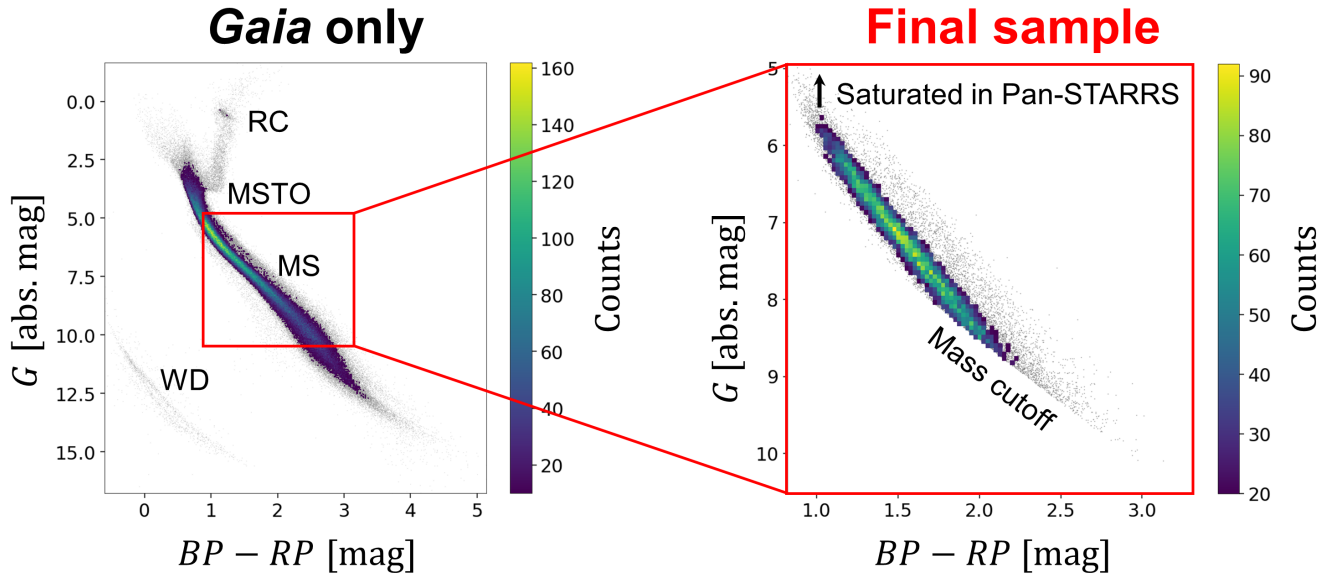


**Figure 12.** The number density of sources across the *Gaia*  $G$  versus  $BP - RP$  CMD for the set of “benchmark” field stars used to calibrate empirical photometric offsets for the MIST and *Bayestar* models assuming a distance of  $1 \text{ kpc} = 1/(1 \text{ mas})$ . Above a given threshold colored histograms are used to highlight the number density; below this threshold individual sources are plotted as gray points. The left panel shows the set of stars with high Galactic latitude ( $|b| > 60$ ), low reddening ( $E(B - V) < 0.2$ ), and well-measured parallax ( $\hat{\varpi}/\sigma_{\varpi} > 50$ ), with a few stellar populations labeled (WD = white dwarf, MS = main sequence, MSTO = main sequence turn-off, RC = red clump). The final collection of  $n = 22933$  stars after requiring full photometric coverage in *Gaia* DR2, Pan-STARRS, 2MASS, and AllWISE is highlighted in the red box and shown on the right. The impact of the Pan-STARRS  $r < 14$  saturation limit and the  $M_{\text{init}} > 0.55 M_{\odot}$  initial mass cutoff are labeled.

Overall, we find that the offsets for the empirical *Bayestar* models are on the order of  $\lesssim 1\%$ , which is expected since the *Bayestar* models were originally constructed using these exact datasets. The resulting offsets for the MIST models (with empirical isochrone corrections) are on the order of  $\sim 3\%$ , in agreement with the results from §5.2, although the exact values differ somewhat between bands. We find that applying these offsets substantially improves the quality of the fits for the MIST models, increasing the number of objects with  $\chi^2/b \lesssim 1$  by  $\sim 20\%$ . In total, we find that  $\sim 95\%$  of the sample is well-fit by both sets of models.

The behavior of these offsets for the *Bayestar* and MIST models as a function of magnitude and position on the *Gaia* CMD can be found in §G.

#### 5.4. Additional Remarks

We emphasize that the corrections outlined in the previous sections should only be seen as “functional” rather than fundamental. They have been calibrated and are designed to be applied to a particular set of stellar models to improve performance in a particular context, and are not expected to apply more generally. This is because these corrections really are a combination of four separate underlying issues:

1. *Shortcomings in stellar evolution models.* The models do not account for magnetic fields, radius inflation, and stellar activity, all of which are important factors for low-mass and evolved stars.
2. *Shortcomings in the stellar atmospheric models.* While the C3K models reproduce color- $T_{\text{eff}}$  relations for most stars except those at the lowest masses, limited molecular line lists and treatment of convection might lead to  $T_{\text{eff}}$ -dependent systematics at  $< 4000 \text{ K}$  (where molecules become important) and for giants (where 3-D effects become more important).
3. *Shortcomings in the dust extinction curve.* The dust extinction curve is known to vary substantially throughout the Galaxy. While the Fitzpatrick (2004) curve used here has been shown to reproduce the overall reddening for giants, modeling errors would lead to systematics as a function of  $A_V$  and  $R_V$  that are almost entirely degenerate with changes in  $T_{\text{eff}}$ .
4. *Shortcomings in the flux calibration in the data.* Based on many recent surveys and work done in Portillo & Speagle et al. (2020) investigating magnitude-dependent biases, we expect these to be at the  $\sim 2\%$  level, although it may be higher



in some cases. This should lead to a single, global offset for each band (up to the non-linearity of the detector).

Using internal testing, we have verified that the offsets derived here are broadly consistent across similar photometric systems in both the optical and NIR, which suggests that the bulk of the offsets in Table 5 are *not* simply absolute zero-point issues. Investigating the exact causes for these effects, however, is beyond the scope of this paper. We hope to investigate these in more detail in future work.

## 6. VALIDATION

To validate and examine the performance of BRUTUS, we consider two classes of tests:

1. *Tests on mock data:* Tests on mock (i.e. simulated) data are important to understand in detail how BRUTUS performs in various scenarios and how well it can recover stellar parameters.
2. *Independent comparisons:* Comparing results against independent methods allows the characterization of systematics when applying BRUTUS to real data.

We describe each class of tests in the following subsections. In §6.1, we discuss a suite of mock tests to illustrate how well BRUTUS is able to recover intrinsic stellar parameters  $\theta$  under various conditions. In §6.2, we examine how well BRUTUS is able to estimate distances compared to *Gaia* DR2 parallax measurements and spectrophotometric distances from Cargile et al. (2020).

A third class of tests (“A/B tests”) where various features of the code were changed one-at-a-time to examine the impact of underlying model choices is discussed in §H.

### 6.1. Tests on Mock Data

Methods that utilize both spectra and photometry are able to get independent constraints on stellar parameters from the spectra (e.g.,  $\log g$ ,  $[\text{Fe}/\text{H}]$ ) and photometry (e.g.,  $T_{\text{eff}}$ ). This enables complementary constraints on distance (via  $\log g \rightarrow \log R_{\star} \rightarrow \log L_{\text{bol}}$ ) as well as on intrinsic color (via  $[\text{Fe}/\text{H}]_{\text{surf}}$ ). Photometry alone, however, does not provide these additional constraints and therefore can’t break these degeneracies. This leads to a much stronger reliance on both the underlying Galactic prior and on independent distance constraints from parallax measurements  $\hat{\varpi}$ .

In order to examine how well BRUTUS is able to recover intrinsic stellar parameters  $\theta$  from photometry and astrometry alone, we generate mock data for stars at several evolutionary states:

- EEP = 350: On the Main Sequence (MS).
- EEP = 450: On the MS turn-off (MSTO).

- EEP = 550: On the first ascent up the Red Giant branch (RGB).
- EEP = 650: On the Red Clump (RC).

As in Cargile et al. (2020), we choose to generate models from a  $t_{\text{age}} = 5$  Gyr MIST isochrone. This spans a wide range of evolutionary states (with differing evolutionary timescales) and a moderate range in initial mass  $M_{\text{init}}$ , leading to a diverse set of SEDs.

To highlight the impact of the prior, we choose to place these sources at a distance of  $d = 1$  kpc along the line-of-sight located at Galactic coordinates of  $(\ell, b) = (90^\circ, 20^\circ)$ . As highlighted in Figure 4, this sightline intersects all major components of our prior, thereby providing an illustrative example of how BRUTUS performs. At  $d = 1$  kpc, in particular, an object is strongly favored to be a member of the thin disk. As a result, we generate two models: one with  $[\text{Fe}/\text{H}]_{\text{init}} = 0$ , which is consistent with the expected metallicity of our prior, and one at  $[\text{Fe}/\text{H}]_{\text{init}} = -1$ , which is more consistent with the thick disk and halo and in tension with our prior.

As shown in Figure 5, this sightline also displays a small but non-negligible amount of dust extinction. To examine systematic deviations from the prior, we set the extinction  $A_V = 0.4$  mag to be somewhat above the mean expected from the 3-D dust extinction prior at  $d = 1$  kpc. We opt to leave  $R_V = 3.3$  to keep it in line with prior expectations.

In Figure 13, we illustrate the impact of the prior for a 10-band SED (Pan-STARRS, 2MASS, and WISE) for a source with a measured parallax  $\hat{\varpi} = 1.0$  mas with a SNR of 5. As shown in the top panels highlighting the CMDs, the fitted SEDs from BRUTUS are nearly identical. However, the inferred parameters differ substantially between the initial fitted likelihoods and the final inferred posteriors. In particular, we see that the IMF prior, combined with the 3-D dust prior, leads BRUTUS to prefer *intrinsically redder* sources on/near the MS. This leads to a bias towards cooler inferred  $T_{\text{eff}}$  values, although the true solution is clearly still captured. To illustrate that this is the ultimate cause, we add in strong constraints on  $A_V$  and  $R_V$  so that there is no additional degeneracy between  $T_{\text{eff}}$  and  $A_V$ . As expected, in this case we achieve unbiased parameter recovery. In general, we find we are able to recover parameters at each EEP quite well, with the uncertainties decreasing for more evolved stars with more distinctive SEDs.

In Figure 14, we illustrate how the inferred parameters vary as a function of parallax SNR. At high SNR ( $\hat{\varpi}/\sigma_{\varpi} = 25$ ), the distance is tightly constrained, leading to the majority of the variation captured in the inferred  $T_{\text{eff}}$  and  $A_V$ . As expected, due to the IMF prior and the slightly higher  $A_V$  value compared to what is expected from the prior, the posterior prefers somewhat intrinsically redder sources, leading to cooler inferred  $T_{\text{eff}}$  (although the true solution is again still captured). At  $\hat{\varpi}/\sigma_{\varpi} = 5$ , the distance is still constrained to be around



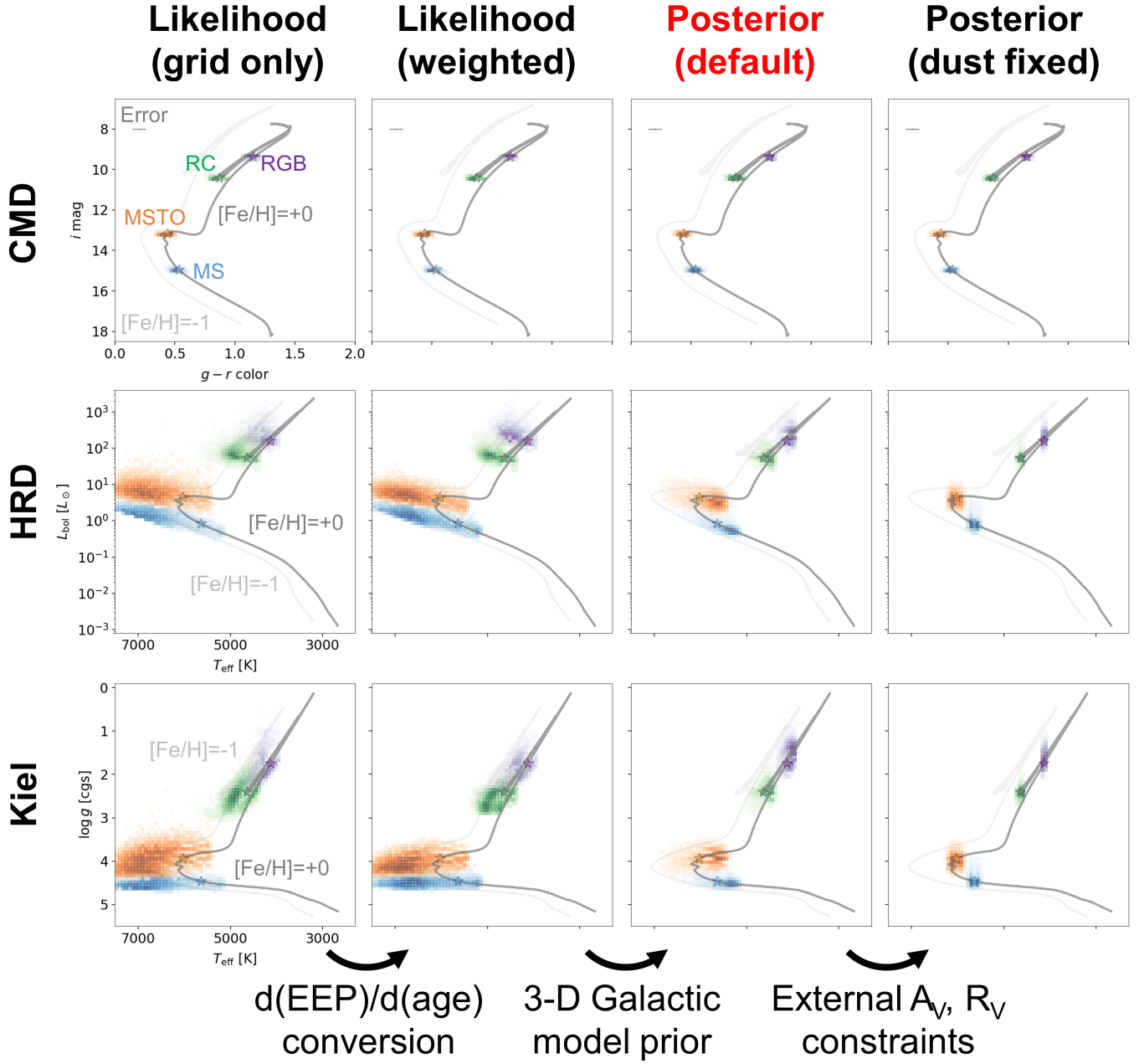


**Figure 13.** Parameter recovery for a mock 10-band SED (Pan-STARRS, 2MASS, and WISE) with a noisy parallax measurement ( $\hat{\omega}/\sigma_{\omega} = 5$ ),  $A_V = 0.4$ ,  $R_V = 3.3$ , and  $d = 1$  kpc located along the same sightline  $(\ell, b) = (90^\circ, 20^\circ)$  shown in Figures 4 and 5. Four cases are highlighted: a star on the main sequence (MS; blue), at the MS turn-off (MSTO; orange), on the red giant branch (RGB; purple), and at the red clump (RC; green). The input values on the  $i$  versus  $g - r$  color-magnitude diagram (CMD; top), Hertzsprung-Russel diagram (HRD; middle), and Kiel diagram (bottom) are indicated with a star.  $[\text{Fe}/\text{H}]_{\text{init}} = 0$  and  $[\text{Fe}/\text{H}]_{\text{init}} = -1$  isochrones are also shown in dark gray and light gray, respectively. The 2-sigma measurement errors are highlighted in the top left corner of the CMD. Samples from the resulting probability density functions (PDFs) derived from BRUTUS are shown as shaded regions taking into account constraints from the SED and measured parallax (far left), uneven model sampling over our grid (middle left), the full 3-D Galactic prior (middle right), and additional (tight) constraints on  $A_V$  and  $R_V$  (far right). Axes labels are only included in the leftmost panels for visual clarity. The initial mass function (IMF) prior, combined with the 3-D dust prior, leads BRUTUS to prefer intrinsically redder, cooler sources on/near the MS, although the true solution is clearly still captured. Strong constraints on  $A_V$  and  $R_V$  give unbiased parameter recovery. Note that the CMD PDFs show the quality of the fits in all cases are essentially identical, highlighting the strong impact our prior has on the inferred parameters.

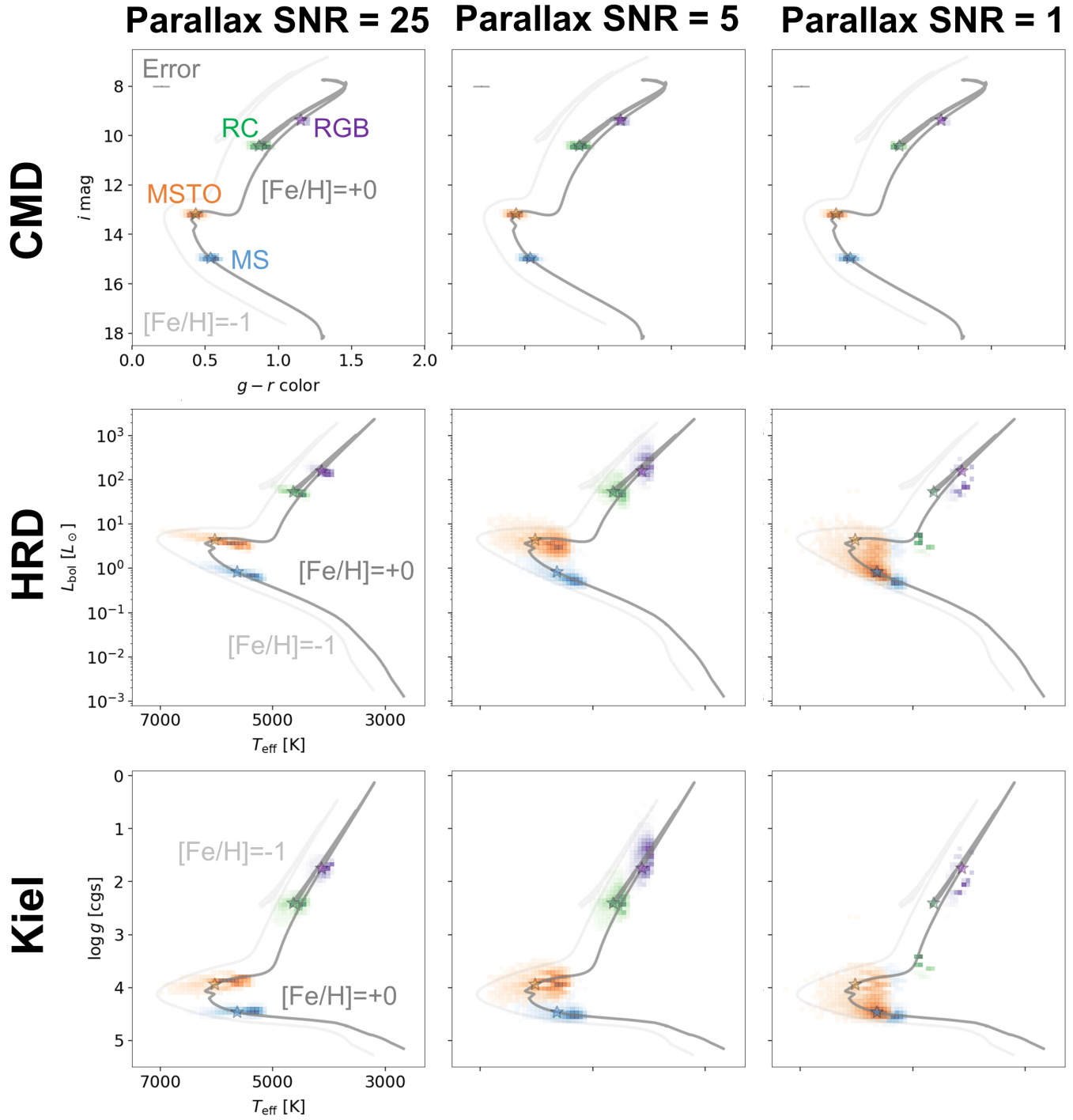


**Figure 14.** As Figure 13, but now showing the posterior as a function of the the measured parallax signal-to-noise (SNR) ratio  $SNR = \hat{\varpi}/\sigma_{\varpi}$  for  $SNR = 25$  (left),  $SNR = 5$  (middle), and  $SNR = 1$ . As in Figure 13, we see that even for objects with well-constrained distances uncertainty on the dust extinction leads to specific degeneracies in the HR and Kiel diagrams along with preferences for cooler, lower-mass sources. These uncertainties are broadened in  $\log L_{bol}$  and  $\log g$  for parallaxes with lower SNR due to larger allowed variation in the estimated distance. At extremely low SNR, the impact of the prior leads to a strong preference for lower masses and longer-lasting phases of stellar evolution, leading to lower estimates on the MS, a preference for the MS over the MSTO, and a preference for the MSTO over the RC. For models that have evolved off the post-MS, the preference for lower-mass solutions and lower dust extinction leads to a preference of higher metallicities and therefore intrinsically redder and cooler SEDs, shifting solutions down and to the right on the HR and Kiel diagrams.

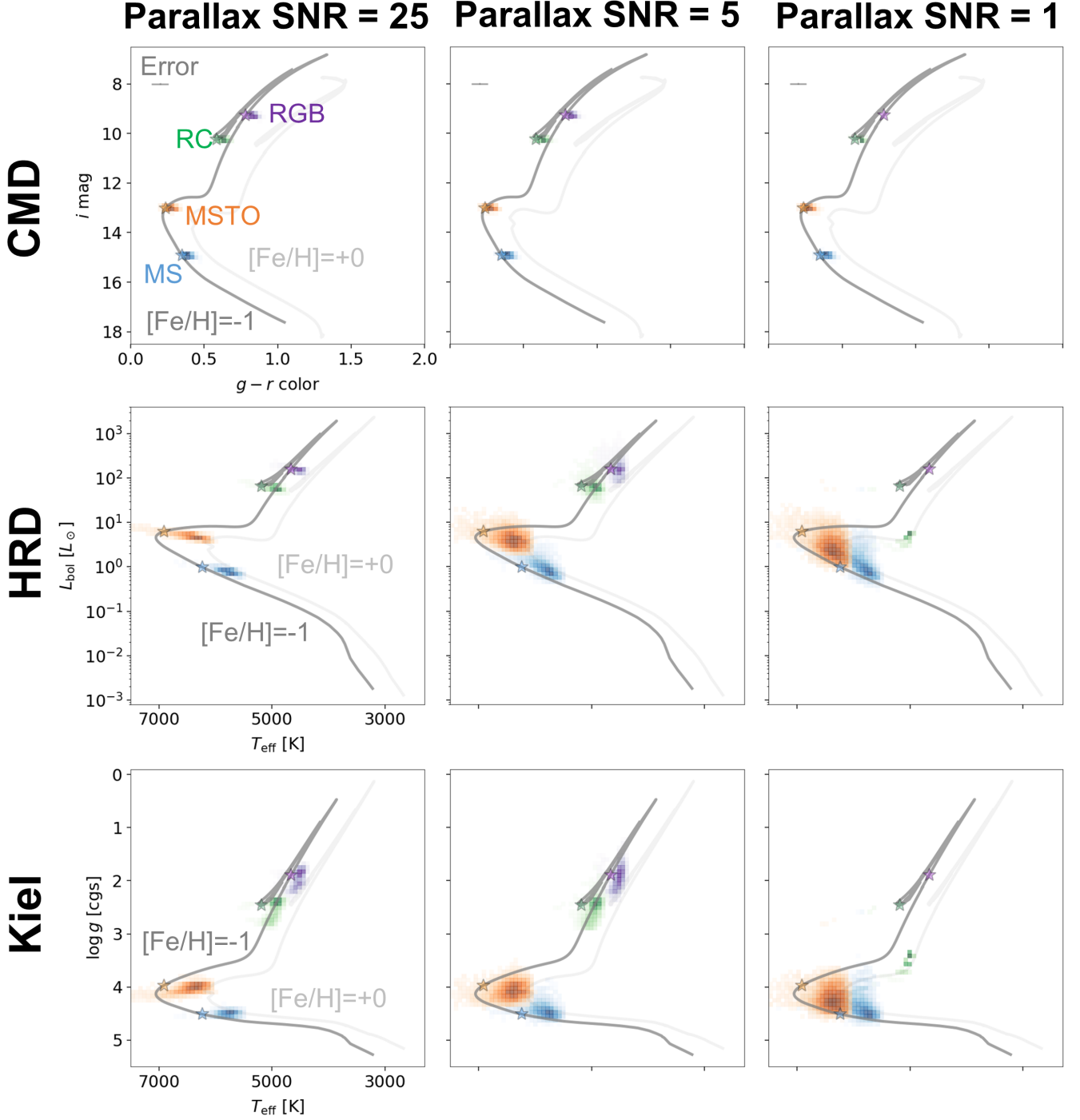


**Figure 15.** As Figure 14, but now for sources with  $[\text{Fe}/\text{H}]_{\text{init}} = -1$  rather than  $[\text{Fe}/\text{H}]_{\text{init}} = 0$ . At this location, our prior strongly prefers metallicities that are consistent with the thin disk, leading to a bias towards redder observed colors in the observed CMD. This remains true even at high parallax SNR (although the true solution remains within the uncertainties). For the RGB solution at low parallax SNR, the prior belief against the correct stellar parameters is so strong that all relevant fits are prematurely removed before the optimization and Monte Carlo sampling steps (see B.6), causing BRUTUS to fail to produce a reliable posterior PDF.

$d \sim 1$  kpc but there is more flexibility to shift the star around, leading to larger uncertainties in  $\log L_{\text{bol}}$  and  $\log g$ . At  $\hat{\varpi}/\sigma_{\varpi} = 1$ , however, the constraint on the distance is much weaker. At this point, the influence of the prior dominates, preferring stars to be at longer-lasting evolutionary stages and lower masses. This shifts the MS star to lower masses, the MSTO star to be on the MS, and the RC star to instead be at the end of the MSTO before beginning the ascent up the RGB. The RGB star, which is uniquely constrained by the SED, instead simply prefers a lower-mass, higher-metallicity solution.

Finally, in Figure 15 we illustrate the  $[\text{Fe}/\text{H}]_{\text{init}} = -1$  case where the metallicity deviates substantially from the expected value based on the Galactic prior. In this case, the prior is strong enough that we actually observe it “pulling” the SED to be intrinsically redder in color, as shown on the CMDs. This also leads the prior to infer metallicities around  $[\text{Fe}/\text{H}]_{\text{init}} = -0.5$  rather than  $-1$ , making the inferred temperatures substantially cooler (and the intrinsic SED redder) compared to their actual values, although again the true solution is clearly still captured. When the parallax SNR becomes  $\sim 1$ , we further see solutions being pulled towards the  $[\text{Fe}/\text{H}]_{\text{init}} = 0$  isochrone and shifted in intrinsic colors appropriately as a result, mirroring the behavior from Figure 14. We also find the RGB solution behaves differently than the other three cases. Due to its rapid evolution, we find that with the default settings the prior belief against the RGB solution is so strong the BRUTUS actually clips the true solution before the final optimization/sampling step and fails to produce a reasonable posterior estimate. This highlights one of the risks with the implementation outlined in §B.6, which can eliminate extremely rare (but possible) solutions from the fitting process. We confirm that true solution can be properly recovered when the thresholds used for clipping fits are substantially relaxed.<sup>11</sup>

### 6.2. Independent Comparison with H3

As a final series of tests, we want to examine how well BRUTUS can recover distances to real stars. To make this comparison, we utilize a subset of  $n \sim 5100$  stars from the H3 survey (Conroy et al. 2019). In brief, the H3 Survey is a high-latitude ( $|b| > 30^\circ$ ), high-resolution ( $R = 32,000$ ) spectroscopic survey of the distant ( $d \gtrsim 2$  kpc Galaxy). Targets are selected purely on their Gaia parallax ( $\varpi < 0.4 - 0.5$  mas), brightness ( $15 < r_{\text{PS1}} < 18$ ), and accessibility to the 6.5 m MMT in Arizona, USA ( $\text{dec} > -20^\circ$ ). The survey measures radial velocities to 0.1 km/s precision, surface abundances ( $[\text{Fe}/\text{H}]_{\text{surf}}$  and  $[\alpha/\text{Fe}]_{\text{surf}}$ ) to 0.1 dex preci-

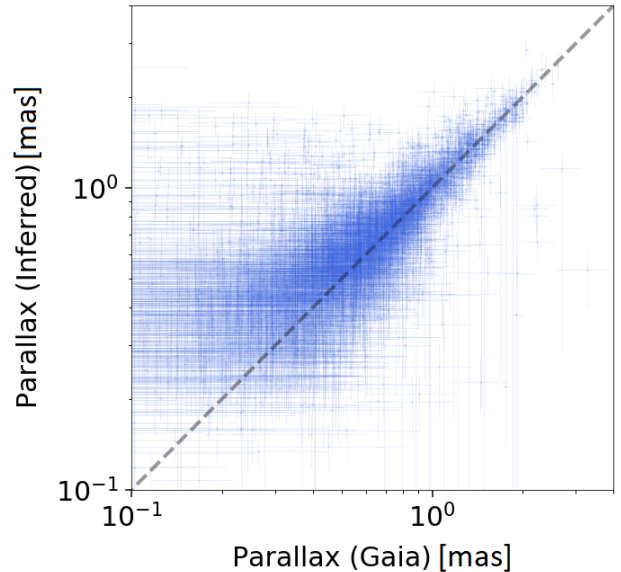


**Figure 16.** The inferred parallax for  $n \sim 5100$  representative objects with (only) a 10-band Pan-STARRS, 2MASS, and WISE SED from BRUTUS versus the estimated parallax from Gaia DR2. 1-sigma errors from both sources are plotted for each point and the one-to-one relation is shown with a dashed gray line. The inferred parallaxes from BRUTUS agree well with the measurements down to low parallax SNR. For smaller parallaxes, we observe a bias towards larger inferred values due to the 3-D stellar density prior, as well as objects with much larger inferred values caused by giants being incorrectly modeled as dwarfs. Both of these effects are expected (see Figures 13, 14, and 15) and largely mitigated once parallax measurements are incorporated into the modelling (see Figure 17).

sion, and spectrophotometric distances to 10% precision using MINESWEEPER (Cargile et al. 2020).

For internal testing purposes, spectrophotometric distances for a few thousand objects were derived from MINESWEEPER both with and without Gaia parallax measurements. In addition to being a representative, low-reddening subsample of sources, all of these measurements were estimated using the same underlying MIST isochrones, excluding the empirical corrections and photometric offsets derived in this work. This makes the comparisons both independent (estimated using different codebases and with/without spectra) while still remaining internally consistent (similar photometry and underlying stellar models).

In Figure 16, we show the inferred parallaxes for this subsample of stars from BRUTUS *without* including the Gaia DR2 parallax measurements using up to 10 bands of photometry (Pan-STARRS, 2MASS, and AllWISE). The results show that BRUTUS is able to recover accurate parallaxes *exclusively* from photometry to many nearby

<sup>11</sup> Some of these changes have been implemented in more recent versions of the code, but are not included in v0.7.5.

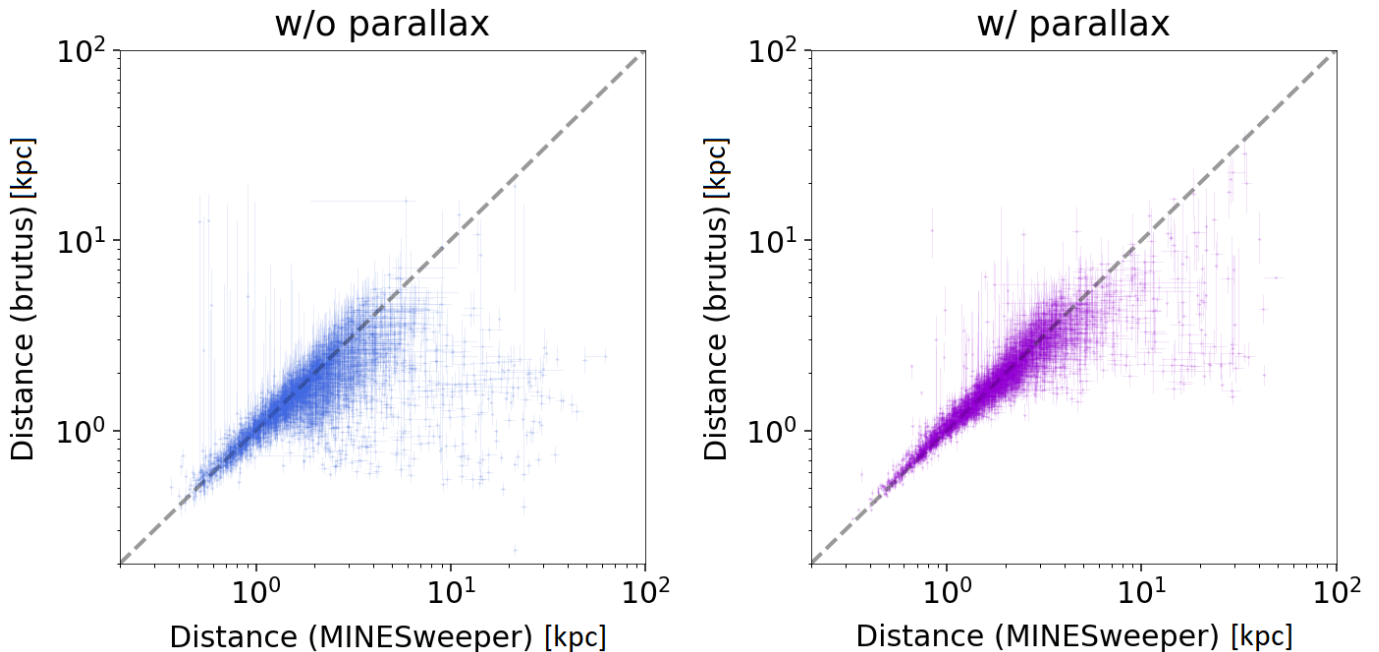


**Figure 17.** A comparison of the distances derived from BRUTUS (photometry only) and MINESWEEPER (photometry and spectroscopy) for the same sample of  $n \sim 5100$  objects shown in Figure 16 without (left, blue) and with (right, purple) *Gaia* parallax constraints. 1-sigma errors from both sources are plotted for each point and the one-to-one relation is shown with a dashed gray line. In both cases, we find excellent agreement between the two methods for the majority of objects. Without parallax constraints, however, BRUTUS overwhelmingly prefers to model sources as being MS dwarfs compared to MINESWEEPER (which has access to  $\log g$  information from the spectrum), leading to a substantial fraction of post-MS giants being incorrectly classified as MS dwarfs. Many of these sources are correctly classified once the parallax information is included in the fits since *even an extremely low SNR parallax still rules out small distances*. In other words, while a parallax of  $\hat{\varpi} \sim 0$  gives almost no constraint on the distance, it *does* imply that  $d \gtrsim 2$  kpc or so, which can be enough to substantially disfavor modeling faraway giants sources as nearby dwarfs.

sources and that the results are mostly unbiased down to objects with smaller parallaxes.

For sources at  $\gtrsim 2$  kpc, we observe a bias towards larger inferred values. This is expected and arises for two reasons. The first is the 3-D Galactic prior, which prefers objects being a few kpc away (see Figure 4), disfavoring larger distances (and therefore smaller parallaxes). This “bias” is physically-motivated and expected, as discussed in Bailer-Jones et al. (2018). The second is the mis-classification of giants as dwarfs, as illustrated in Figures 14 and 15, which leads to anomalously large parallax estimates compared to the measured values from *Gaia*.

We now investigate how the distance estimates from BRUTUS compare with those from MINESWEEPER for the same sample of stars. In Figure 17, we show the resulting distances estimated with and without *Gaia* DR2 parallaxes. In the left panel of the figure, we see that indeed without parallax constraints BRUTUS systematically mis-classifies giants as dwarfs relative to the spectroscopic classifications obtained by MINESWEEPER. Outside of these sources at large distances, however, the

results are in excellent agreement between the two codes and datasets.

Once the parallaxes are included, the overall distance agreement improves, as expected. We also observe that the rate of mis-classification between BRUTUS and MINESWEEPER decreases substantially, even for objects with extremely small parallaxes and correspondingly low parallax SNRs. This result is due to one fundamental feature of parallaxes: *even an extremely low SNR parallax still rules out small distances*. In other words, while a parallax of  $\hat{\varpi} \sim 0$  gives almost no constraint on the distance, it *does* imply that  $d \gtrsim 2$  kpc or so, which is enough to substantially disfavor modeling faraway giants sources as nearby dwarfs. This further highlights just how crucial parallax measurements *at all SNR* are for accurately recovering not only intrinsic stellar parameters but also accurate distances to many sources.

## 7. CONCLUSION

One of the main challenges of studying the Milky Way is transforming observations of the projected 2-D positions of sources on the sky into full 3-D maps. This has become particularly important in recent years as



large-area surveys such as SDSS (York et al. 2000), Pan-STARRS (Chambers et al. 2016), and *Gaia* (Gaia Collaboration et al. 2016) provide measurements to billions of stars. These datasets have been crucial to driving new discoveries related to the structure and evolution of the Milky Way (Koppelman et al. 2018; Belokurov et al. 2018; Helmi et al. 2018; Antoja et al. 2018).

To build the reliable 3-D maps much of these discoveries are based on, the raw observations (photometry, astrometry, spectroscopy, etc.) from these surveys must be converted into physical quantities such as 3-D positions and velocities, metallicities, masses, ages, and more. Part of this process requires developing an algorithm that can quickly yet robustly derive many of these parameters from photometry and astrometry alone, which characterizes the vast majority ( $\sim 99\%$ ) of the data currently available in the Milky Way.

To assist with this process, in this paper we presented BRUTUS, a public, open-source PYTHON package that uses a combination of statistical approaches to infer stellar properties, distances, and extinctions for sources using photometry and astrometry. We described the statistical framework behind the code (§2), the techniques used to perform inference (§3), and the stellar models that are currently implemented (§4). All of these portions of the code are designed to be highly modular so that each component can be adjusted and varied through various input files and command-line arguments.

We then outlined a procedure for “calibrating” the underlying stellar models in BRUTUS using a novel approach to fit stellar clusters (§D). We applied this procedure to a series of “benchmark” open clusters, finding excellent overall fits (§5.2). We then used a sample of  $\sim 20,000$  nearby field stars to further investigate photometric offsets, further demonstrating the underlying models match the data well (§5.3).

Finally, we validated the performance of the code using a series of validation tests over both mock data and real observations (§6). These illustrated that BRUTUS performs well overall while also highlighting the limitations of the code and the sensitivity of parameter recovery to the Galactic prior and parallax observations.

Overall, we hope that the paper serves as a useful overview of the challenges associated with astrophotometric stellar parameter estimation and the various parts of BRUTUS that attempt to solve this problem. The application of the code to a sample of  $> 10^8$  stars are described in a companion paper (?).

## ACKNOWLEDGMENTS

### *Contributions:*

The author list is divided up into 3 groups:

1. a list of primary authors who made direct contributions to the BRUTUS codebase and were actively involved in development and testing (JSS, CZ, and ABe),
2. an alphabetized secondary list of authors who made direct contributions to data products, indirect contributions to the code, and/or were involved in detailed discussions surrounding its development (PAC to EFS), and
3. an alphabetized tertiary list of authors who provided useful feedback during the development process and/or on the paper itself (ABo to IAZ).

### *Personal:*

JSS is immensely grateful to Rebecca Bleich for being an amazing and supportive partner during these difficult times. JSS would also like to thank Jan Rybizki, Stefan Meingast, João Alves, Seth Gossage, and Nayan-tara Mudur for insightful discussions that improved the quality of this work.

### *Funding:*

JSS and CZ were partially supported by the Harvard Data Science Initiative. HMK acknowledges support from the DOE CSGF under grant number DE-FG02-97ER25308. AD received support from the National Aeronautics and Space Administration (NASA) under Contract No. NNG16PJ26C issued through the WFIRST Science Investigation Teams Program. CZ and DPF acknowledge support from NSF grant AST-1614941, “Exploring the Galaxy: 3-Dimensional Structure and Stellar Streams.” AKS gratefully acknowledges support by a National Science Foundation Graduate Research Fellowship (DGE-1745303). YST acknowledges financial support from the Australian Research Council through DECRA Fellowship DE220101520.

### *Code:*

This work has benefited from the following packages:

- ASTROPY (Astropy Collaboration et al. 2013; Price-Whelan et al. 2018)
- NUMPY (van der Walt et al. 2011)
- SCIPY (Virtanen et al. 2020)
- MATPLOTLIB (Hunter 2007)
- HEALPY (Górski et al. 2005; Zonca et al. 2019)
- CORNER (Foreman-Mackey 2016)
- HDBSCAN (McInnes et al. 2017; McInnes & Healy 2017)

## REFERENCES

- Anders, F., Khalatyan, A., Chiappini, C., et al. 2019, *A&A*, 628, A94
- Antoja, T., Helmi, A., Romero-Gómez, M., et al. 2018, *Nature*, 561, 360
- Astropy Collaboration, Robitaille, T. P., Tollerud, E. J., et al. 2013, *A&A*, 558, A33
- Bailer-Jones, C. A. L., Rybizki, J., Fouesneau, M., Demleitner, M., & Andrae, R. 2021, *AJ*, 161, 147
- Bailer-Jones, C. A. L., Rybizki, J., Fouesneau, M., Mantelet, G., & Andrae, R. 2018, *AJ*, 156, 58
- Belokurov, V., Erkal, D., Evans, N. W., Koposov, S. E., & Deason, A. J. 2018, *MNRAS*, 478, 611
- Belokurov, V., Zucker, D. B., Evans, N. W., et al. 2006, *ApJL*, 642, L137
- Berdugina, S. V. 2005, *Living Reviews in Solar Physics*, 2, 8
- Bland-Hawthorn, J., & Gerhard, O. 2016, *ARA&A*, 54, 529
- Bonaca, A., & Hogg, D. W. 2018, *ApJ*, 867, 101
- Bressan, A., Marigo, P., Girardi, L., et al. 2012, *MNRAS*, 427, 127
- Brooks, S., Gelman, A., Jones, G., & Meng, X.-L. 2011, *Handbook of Markov Chain Monte Carlo* (CRC press)
- Campello, R. J. G. B., Moulavi, D., & Sander, J. 2013, in *Advances in Knowledge Discovery and Data Mining*, ed. J. Pei, V. S. Tseng, L. Cao, H. Motoda, & G. Xu (Berlin, Heidelberg: Springer Berlin Heidelberg), 160–172
- Cardelli, J. A., Clayton, G. C., & Mathis, J. S. 1989, *ApJ*, 345, 245
- Cargile, P. A., Conroy, C., Johnson, B. D., et al. 2020, *ApJ*, 900, 28
- Chabrier, G. 2003, *PASP*, 115, 763
- Chambers, K. C., Magnier, E. A., Metcalfe, N., et al. 2016, *arXiv e-prints*, arXiv:1612.05560
- Choi, J., Dotter, A., Conroy, C., et al. 2016, *ApJ*, 823, 102
- Conroy, C., Bonaca, A., Cargile, P., et al. 2019, *arXiv e-prints*, arXiv:1907.07684
- Cutri, R. M., & et al. 2013, *VizieR Online Data Catalog*, II/328
- De Gennaro, S., von Hippel, T., Jefferys, W. H., et al. 2009, *ApJ*, 696, 12
- de Jong, J. T. A., Rix, H. W., Martin, N. F., et al. 2008, *AJ*, 135, 1361
- Dolphin, A. 1997, *NewA*, 2, 397
- Dolphin, A. E. 2002, *MNRAS*, 332, 91
- Dotter, A. 2016, *ApJS*, 222, 8
- Dotter, A., Chaboyer, B., Ferguson, J. W., et al. 2007, *ApJ*, 666, 403
- Dotter, A., Milone, A. P., Conroy, C., Marino, A. F., & Sarajedini, A. 2018, *ApJL*, 865, L10
- Draine, B. T. 2003, *ARA&A*, 41, 241
- Eldridge, J. J., Stanway, E. R., Xiao, L., et al. 2017, *PASA*, 34, e058
- Evans, D. W., Riello, M., De Angeli, F., et al. 2018, *A&A*, 616, A4
- Finkbeiner, D. P., Padmanabhan, N., Schlegel, D. J., et al. 2004, *AJ*, 128, 2577
- Fitzpatrick, E. L. 1999, *PASP*, 111, 63
- Fitzpatrick, E. L. 2004, in *Astronomical Society of the Pacific Conference Series*, Vol. 309, *Astrophysics of Dust*, ed. A. N. Witt, G. C. Clayton, & B. T. Draine, 33
- Foreman-Mackey, D. 2016, *The Journal of Open Source Software*, 24, doi:10.21105/joss.00024. <http://dx.doi.org/10.5281/zenodo.45906>
- Gaia Collaboration, Brown, A. G. A., Vallenari, A., et al. 2016, *A&A*, 595, A2
- . 2018, *A&A*, 616, A1
- . 2021, *A&A*, 649, A1
- García Pérez, A. E., Allende Prieto, C., Holtzman, J. A., et al. 2016, *AJ*, 151, 144
- Górski, K. M., Hivon, E., Banday, A. J., et al. 2005, *ApJ*, 622, 759
- Gossage, S., Conroy, C., Dotter, A., et al. 2018, *ApJ*, 863, 67
- . 2019, *ApJ*, 887, 199
- Gouliermis, D. A., Dolphin, A. E., Robberto, M., et al. 2011, *ApJ*, 738, 137
- Green, G. M. 2018, *The Journal of Open Source Software*, 3, 695
- Green, G. M., Schlafly, E., Zucker, C., Speagle, J. S., & Finkbeiner, D. 2019, *ApJ*, 887, 93
- Green, G. M., & Ting, Y.-S. 2020, *arXiv e-prints*, arXiv:2011.04673
- Green, G. M., Schlafly, E. F., Finkbeiner, D. P., et al. 2014, *ApJ*, 783, 114
- . 2015, *ApJ*, 810, 25
- Green, G. M., Schlafly, E. F., Finkbeiner, D., et al. 2018, *MNRAS*, 478, 651
- Green, G. M., Rix, H.-W., Tschesche, L., et al. 2021, *ApJ*, 907, 57
- Gustafsson, B., Edvardsson, B., Eriksson, K., et al. 2008, *A&A*, 486, 951
- Helmi, A., Babusiaux, C., Koppelman, H. H., et al. 2018, *Nature*, 563, 85
- Hogg, D. W., & Foreman-Mackey, D. 2018, *ApJS*, 236, 11
- Hunter, J. D. 2007, *Computing in Science Engineering*, 9, 90
- Ivezic, Z., Tyson, J. A., Abel, B., et al. 2008, *ArXiv e-prints*, arXiv:0805.2366

- Johnston, K. V., Zhao, H., Spergel, D. N., & Hernquist, L. 1999, *ApJL*, 512, L109
- Jurić, M., Ivezić, Ž., Brooks, A., et al. 2008, *ApJ*, 673, 864
- Koppelman, H., Helmi, A., & Veljanoski, J. 2018, *ApJL*, 860, L11
- Kroupa, P. 2001, *MNRAS*, 322, 231
- Kupka, F. G., Ryabchikova, T. A., Piskunov, N. E., Stempels, H. C., & Weiss, W. W. 2000, *Baltic Astronomy*, 9, 590
- Kurucz, R. L. 1970, *SAO Special Report*, 309
- . 1993, *SYNTH* spectrum synthesis programs and line data
- Kurucz, R. L., & Avrett, E. H. 1981, *SAO Special Report*, 391
- Lallement, R., Babusiaux, C., Vergely, J. L., et al. 2019, *A&A*, 625, A135
- Law, D. R., & Majewski, S. R. 2010, *ApJ*, 714, 229
- Leike, R. H., & Enßlin, T. A. 2019, *A&A*, 631, A32
- Leike, R. H., Glatzle, M., & Enßlin, T. A. 2020, *A&A*, 639, A138
- Leja, J., Speagle, J. S., Johnson, B. D., et al. 2019, *arXiv e-prints*, arXiv:1910.04168
- Lindgren, L., Hernández, J., Bombrun, A., et al. 2018, *A&A*, 616, A2
- Maíz Apellániz, J., & Weiler, M. 2018, *A&A*, 619, A180
- McInnes, L., & Healy, J. 2017, in *Data Mining Workshops (ICDMW)*, 2017 IEEE International Conference on, IEEE, 33–42
- McInnes, L., Healy, J., & Astels, S. 2017, *The Journal of Open Source Software*, 2, 205
- Naidu, R. P., Conroy, C., Bonaca, A., et al. 2021, *arXiv e-prints*, arXiv:2103.03251
- Nelder, J. A., & Mead, R. 1965, *Computer Journal*, 7, 308
- Ness, M., Hogg, D. W., Rix, H. W., Ho, A. Y. Q., & Zasowski, G. 2015, *ApJ*, 808, 16
- Newberg, H. J., & Yanny, B. 1997, *ApJS*, 113, 89
- Paxton, B., Bildsten, L., Dotter, A., et al. 2011, *ApJS*, 192, 3
- Paxton, B., Cantiello, M., Arras, P., et al. 2013, *ApJS*, 208, 4
- Paxton, B., Marchant, P., Schwab, J., et al. 2015, *ApJS*, 220, 15
- Paxton, B., Schwab, J., Bauer, E. B., et al. 2018, *ApJS*, 234, 34
- Paxton, B., Smolec, R., Schwab, J., et al. 2019, *ApJS*, 243, 10
- Piskunov, N. E., Kupka, F., Ryabchikova, T. A., Weiss, W. W., & Jeffery, C. S. 1995, *A&AS*, 112, 525
- Planck Collaboration, Ade, P. A. R., Aghanim, N., et al. 2016, *A&A*, 594, A20
- Portillo & Speagle, S. K. N., S., J., & Finkbeiner, D. P. 2020, *AJ*, 159, 165
- Powell, M. J. D. 1964, *The Computer Journal*, 7, 155. <http://comjnl.oxfordjournals.org/content/7/2/155.abstract>
- Price-Whelan, A. M., Sipőcz, B. M., Günther, H. M., et al. 2018, *AJ*, 156, 123
- Queiroz, A. B. A., Anders, F., Santiago, B. X., et al. 2018, *MNRAS*, 476, 2556
- Read, J. I. 2014, *Journal of Physics G Nuclear Physics*, 41, 063101
- Read, J. I., Lake, G., Agertz, O., & Debattista, V. P. 2008, *MNRAS*, 389, 1041
- Rezaei Kh., S., Bailer-Jones, C. A. L., Hogg, D. W., & Schultheis, M. 2018, *A&A*, 618, A168
- Roškar, R., Debattista, V. P., Quinn, T. R., Stinson, G. S., & Wadsley, J. 2008, *ApJL*, 684, L79
- Ryabchikova, T., Piskunov, N., Kurucz, R. L., et al. 2015, *PhyS*, 90, 054005
- Salpeter, E. E. 1955, *ApJ*, 121, 161
- Sandage, A. R. 1953, *AJ*, 58, 61
- Santiago, B. X., Brauer, D. E., Anders, F., et al. 2016, *A&A*, 585, A42
- Schlafly, E. F., & Finkbeiner, D. P. 2011, *ApJ*, 737, 103
- Schlafly, E. F., Peek, J. E. G., Finkbeiner, D. P., & Green, G. M. 2017, *ApJ*, 838, 36
- Schlafly, E. F., Green, G., Finkbeiner, D. P., et al. 2014, *ApJ*, 789, 15
- Schlafly, E. F., Meisner, A. M., Stutz, A. M., et al. 2016, *ApJ*, 821, 78
- Schlegel, D. J., Finkbeiner, D. P., & Davis, M. 1998, *ApJ*, 500, 525
- Sharma, S. 2017, *Annual Review of Astronomy and Astrophysics*, 55, 213
- Skilling, J. 2004, in *American Institute of Physics Conference Series*, Vol. 735, American Institute of Physics Conference Series, ed. R. Fischer, R. Preuss, & U. V. Toussaint, 395–405
- Skilling, J. 2006, *Bayesian Anal.*, 1, 833. <https://doi.org/10.1214/06-BA127>
- Skrutskie, M. F., Cutri, R. M., Stiening, R., et al. 2006, *AJ*, 131, 1163
- Somers, G., Cao, L., & Pinsonneault, M. H. 2020, *ApJ*, 891, 29
- Somers, G., & Pinsonneault, M. H. 2015, *ApJ*, 807, 174
- Speagle, J. S. 2019, *arXiv e-prints*, arXiv:1909.12313
- Thomas, D., Maraston, C., & Bender, R. 2003, *MNRAS*, 339, 897
- Ting, Y.-S., Conroy, C., Rix, H.-W., & Cargile, P. 2019, *ApJ*, 879, 69

- van der Walt, S., Colbert, S. C., & Varoquaux, G. 2011, Computing in Science Engineering, 13, 22
- van Dyk, D. A., DeGennaro, S., Stein, N., Jefferys, W. H., & von Hippel, T. 2009, Ann. Appl. Stat., 3, 117.  
<https://doi.org/10.1214/08-AOAS219>
- Virtanen, P., Gommers, R., Oliphant, T. E., et al. 2020, Nature Methods, 17, 261
- von Hippel, T., Jefferys, W. H., Scott, J., et al. 2006, ApJ, 645, 1436
- Wechsler, R. H., Bullock, J. S., Primack, J. R., Kravtsov, A. V., & Dekel, A. 2002, ApJ, 568, 52
- Weisz, D. R., Dalcanton, J. J., Williams, B. F., et al. 2011, ApJ, 739, 5
- Xiang, M., Ting, Y.-S., Rix, H.-W., et al. 2019, ApJS, 245, 34
- Xue, X.-X., Rix, H.-W., Ma, Z., et al. 2015, ApJ, 809, 144
- York, D. G., Adelman, J., Anderson, Jr., J. E., et al. 2000, AJ, 120, 1579
- Zonca, A., Singer, L., Lenz, D., et al. 2019, Journal of Open Source Software, 4, 1298.  
<https://doi.org/10.21105/joss.01298>
- Zucker, C., Speagle, J. S., Schlafly, E. F., et al. 2020, A&A, 633, A51
- Zucker & Speagle, C. . J. S., Schlafly, E. F., Green, G. M., et al. 2019, ApJ, 879, 125

## APPENDIX

## A. DETAILED DESCRIPTION OF PRIORS

A.1. *Initial Mass Function*

We assume that stars are all born with initial masses  $M_{\text{init}}$  independently sampled from a universal stellar initial mass function (IMF). We assume that this follows a broken power law such that

$$\pi(M_{\text{init}}) \propto \begin{cases} 0 & M_{\text{init}} < 0.08 \\ M_{\text{init}}^{-\alpha_1} & 0.08 \leq M_{\text{init}} < 0.5 \\ M_{\text{init}}^{-\alpha_2} & M_{\text{init}} \geq 0.5 \end{cases} \quad (\text{A1})$$

where we exclude initial masses below the deuterium-burning limit of  $\sim 0.08M_{\odot}$  and we set  $\alpha_1 = -1.3$  and  $\alpha_2 = -2.3$  following [Kroupa \(2001\)](#). As we currently do not recommend modeling stars below  $0.5M_{\odot}$  (see §5), this is functionally equivalent to a [Salpeter \(1955\)](#) IMF. We hope to extend our models and priors down to lower stellar masses in future work.

A.2. *3-D Stellar Number Density*

For a given number density distribution  $n(d|\ell, b)$  along a particular line of sight (LOS) specified by Galactic coordinate  $\ell$  and  $b$ , the probability of observing stars at a given distance  $d$  involves accounting for the increasing differential volume from the associated shell  $dV/dd = 4\pi d^2$  as a function of distance so that

$$\pi(d|\ell, b) \propto n(d|\ell, b) \times d^2 \quad (\text{A2})$$

We assume that the number density of stars in the Galaxy come from three components:

- A *thin disk* of younger stars with higher metallicities.
- A *thick disk* of slightly older stars with lower metallicities.
- A *halo* of substantially older stars with low metallicities.

This implies our number density is

$$n(d|\ell, b) = \sum_x n_x(d|\ell, b) \quad (\text{A3})$$

where the sum over  $x$  is taken over each component  $n_{\text{thin}}(d|\ell, b)$ ,  $n_{\text{thick}}(d|\ell, b)$ , and  $n_{\text{halo}}(d|\ell, b)$ . Unlike other recent work (e.g., [Anders et al. 2019](#)), we do not currently include any components corresponding to the Galactic bulge and/or bar. We hope to include these in future work. Note that while we use terms like “thick disk” to refer to these functions, they are intended to be purely *operational* terms that serve as shorthand to describe the underlying components and are not meant to imply any particular formation history.

Since measuring absolute number densities can be difficult, observations often can better constrain the *relative* number density  $n'(d|\ell, b)$  such that

$$n_x(d|\ell, b) = f_x \times n_{\odot, \text{thin}} \times n'_x(d|\ell, b) \quad (\text{A4})$$

where  $n'_x(d = 0|\ell, b) \equiv 1$  at the position of the Sun ( $d = 0$ ),  $n_{\odot, \text{thin}}$  is the number density of the thin disk at  $d = 0$ , and  $f_x$  is a scale factor specifying the relative contribution for the  $x$ th component (where  $f_{\text{thin}} = 1$  by definition). Since  $n_{\odot, \text{thin}}$  is the same for all terms, we can ignore its contribution to the prior and work directly with  $f_x$  and  $n'_x(d|\ell, b)$ .

We model the relative number density of stars in the thin and thick disk with an exponential profile as a function of Galactocentric radius  $R$  and disk height  $Z$

$$n'_{\text{disk}}(R, Z) = \exp\left[\frac{R - R_{\odot}}{R_{\text{disk}}}\right] \times \exp\left[\frac{|Z| - |Z_{\odot}|}{Z_{\text{disk}}}\right] \quad (\text{A5})$$

where  $R_{\text{disk}}$  is the scale radius,  $Z_{\text{disk}}$  is the scale height, and  $R_{\odot} = 8.2$  kpc and  $Z_{\odot} = 0.025$  kpc are the corresponding Solar values taken from [Bland-Hawthorn & Gerhard \(2016\)](#). It is straightforward to convert from Galactic coordinates to Galactocentric cylindrical coordinates  $(d, \ell, b) \rightarrow (R, Z, \phi)$  to evaluate this prior from our observed data using



ASTROPY<sup>12</sup> (Astropy Collaboration et al. 2013; Price-Whelan et al. 2018) or other publicly-available PYTHON packages. The values for constants assumed for the thin and thick disk are taken from Bland-Hawthorn & Gerhard (2016) and summarized in Table 1.

Following Xue et al. (2015), we model the relative number density of stars in the halo using a power law of the form

$$n'_{\text{halo}}(r_{\text{eff}}) = \left( \frac{r_{\text{eff}}}{r_{\odot, \text{eff}}} \right)^{-\eta} \quad (\text{A6})$$

as a function of effective radius

$$r_{\text{eff}}(R, Z, q(r), R_s) = \sqrt{R^2 + (Z/q(r))^2 + R_s^2} \quad (\text{A7})$$

where  $\eta = 4.2$ ,  $q$  is the oblateness ( $q = 1$  is spherical,  $q = 0$  is perfectly flat) and  $R_s = 1$  kpc is a smoothing radius that prevents the power law from diverging near the Galactic center.<sup>13</sup> The oblateness  $q(r)$  is allowed to change as a function of Galactocentric spherical radius  $r = \sqrt{R^2 + Z^2}$  such that:

$$q(r) = q_{\infty} - (q_{\infty} - q_0) \times \exp \left[ 1 - \sqrt{1 + (r/r_q)^2} \right] \quad (\text{A8})$$

where  $q_{\infty} = q(r = \infty) = 0.8$  is the oblateness at large radii,  $q_0 = q(r = 0) = 0.2$  is the oblateness at the Galactic center, and  $r_q = 6$  kpc is the scale radius over which the oblateness begins to transition from  $q_0$  to  $q_{\infty}$ . To ensure  $n'_{\text{halo}}(R_{\odot}, Z_{\odot}) = 1$ , the function is normalized to

$$r_{\odot, \text{eff}} \equiv \sqrt{R_{\odot}^2 + (Z_{\odot}/q_{\odot})^2 + R_s^2} \approx 8.26 \text{ kpc} \quad (\text{A9})$$

where  $q_{\odot} = q(r = r_{\odot}) \approx 0.5$  for  $r_{\odot} = \sqrt{R_{\odot}^2 + Z_{\odot}^2}$ .

A schematic illustration of our combined 3-D number density/distance prior is shown in Figure 2.

### A.3. 3-D Stellar Metallicity

We assume a spatially-invariant prior on the metallicities of stars within each component (indexed by  $x$ ) based loosely on Bland-Hawthorn & Gerhard (2016) and Anders et al. (2019) that follow a Normal distribution with mean  $\mu_{[\text{Fe}/\text{H}],x}$  and standard deviation  $\sigma_{[\text{Fe}/\text{H}],x}$ :

$$\pi_x([\text{Fe}/\text{H}]_{\text{init}}) = \frac{1}{\sqrt{2\pi\sigma_{[\text{Fe}/\text{H}],x}^2}} \times \exp \left[ -\frac{1}{2} \frac{([\text{Fe}/\text{H}]_{\text{init}} - \mu_{[\text{Fe}/\text{H}],x})^2}{\sigma_{[\text{Fe}/\text{H}],x}^2} \right] \quad (\text{A10})$$

$$\equiv \mathcal{N} \left[ \mu_{[\text{Fe}/\text{H}],x}, \sigma_{[\text{Fe}/\text{H}],x}^2 \right] \quad (\text{A11})$$

where we slightly abuse notation by letting  $\mathcal{N}[\mu, \sigma^2]$  represent the PDF of a Normal distribution with mean  $\mu$  and standard deviation  $\sigma$ . The metallicity prior at a particular 3-D position is then a number-density weighted combination of each component

$$\pi([\text{Fe}/\text{H}]_{\text{init}}|d, \ell, b) = \sum_x \frac{n_x(d|\ell, b)}{n(d|\ell, b)} \times \pi_x([\text{Fe}/\text{H}]_{\text{init}}) \quad (\text{A12})$$

The values for the mean and standard deviation of each component of our prior (thin disk, thick disk, and halo) are summarized in Table 1 and highlighted in Figure 3.

### A.4. 3-D Stellar Age

Similar to our metallicity prior, we also assume a spatially-invariant prior on the ages of stars within each component loosely following Bland-Hawthorn & Gerhard (2016), Xue et al. (2015), and Anders et al. (2019) that follows a truncated Normal distribution between minimum age  $t_{\text{min}}$  and maximum age  $t_{\text{max}}$  with mean  $\mu_{t,x}$  and standard deviation  $\sigma_{t,x}$ :

$$\pi_x(t_{\text{age}}) = \begin{cases} \frac{\mathcal{N}[\mu_{t,x}, \sigma_{t,x}^2]}{\int_{t_{\text{min}}}^{t_{\text{max}}} \mathcal{N}[\mu_{t,x}, \sigma_{t,x}^2] dt_{\text{age}}} & t_{\text{min}} \leq t_{\text{age}} \leq t_{\text{max}} \\ 0 & \text{otherwise} \end{cases} \quad (\text{A13})$$

<sup>12</sup> <https://www.astropy.org>

<sup>13</sup> Note that this is larger than the  $R_s = 0.5$  kpc adopted in Green et al. (2019) to avoid being overly sensitive to density changes near the Galactic center.

where we choose  $t_{\min} = 0$  and  $t_{\max} = 13.8$  (roughly the current age of the Universe; [Planck Collaboration et al. 2016](#)). The age prior at a particular 3-D position is again a number-density weighted combination of each component

$$\pi(t_{\text{age}}|d, \ell, b) = \sum_x \frac{n_x(d|\ell, b)}{n(d|\ell, b)} \times \pi_x(t_{\text{age}}) \quad (\text{A14})$$

Although we do not account for explicit covariances between the metallicities and ages of stars within/across components in this work, we still want to connect the overall mean  $\mu_{t,x}$  and scatter  $\sigma_{t,x}$  in the ages of stars for each component to the mean metallicity  $\mu_{[\text{Fe}/\text{H}],x}$  of that component. We choose a smooth logistic function

$$\mu_{t,x}(\mu_{[\text{Fe}/\text{H}],x}) = \frac{t_{\max} - t_{\min}}{1 + \exp\left[\frac{\mu_{[\text{Fe}/\text{H}],x} - \xi_{[\text{Fe}/\text{H}]}}{\Delta_{[\text{Fe}/\text{H}]}}\right]} + t_{\min} \quad (\text{A15})$$

where  $\xi_{[\text{Fe}/\text{H}]} = -0.5$  is the ‘‘pivot’’ metallicity halfway between  $t_{\min}$  and  $t_{\max}$  and  $\Delta_{[\text{Fe}/\text{H}]} = 0.5$  is the metallicity scale-length over which the age transitions from  $t_{\min}$  to  $t_{\max}$ .

The scatter  $\sigma_{t,x}$  is subsequently set based on the mean age of the population  $\mu_{t,x}$  as:

$$\sigma_{t,x}(\mu_{t,x}) = \begin{cases} \sigma_{t,\min} & \frac{t_{\max} - \mu_{t,x}}{n_\sigma} < \sigma_{t,\min} \\ \frac{t_{\max} - \mu_{t,x}}{n_\sigma} & \sigma_{t,\min} \leq \frac{t_{\max} - \mu_{t,x}}{n_\sigma} \leq \sigma_{t,\max} \\ \sigma_{t,\max} & \frac{t_{\max} - \mu_{t,x}}{n_\sigma} > \sigma_{t,\max} \end{cases} \quad (\text{A16})$$

where  $\sigma_{t,\min}$  is the minimum allowed scatter,  $\sigma_{t,\max}$  is the maximum allowed scatter, and  $n_\sigma$  scales  $\sigma_{t,x}$  relative to the difference between the mean age and the maximum age  $t_{\max} - \mu_{t,x}$ . This function smoothly varies the scatter in age between a maximum value of  $\sigma_{t,\max}$  and a minimum value of  $\sigma_{t,\min}$  as the age increases relative to the maximum allowed age  $t_{\max}$ . This ensures that younger populations (such as in the disk) have a higher allowed age dispersion arising from more extended star formation histories, while older populations (such as in the halo) have a lower allowed age dispersion due to the shorter timescale over which the stars could have formed.

The values for this ‘‘age-metallicity relation’’ and the corresponding the mean and standard deviation of the age for each component (thin disk, thick disk, and halo) are summarized in [Table 1](#) and highlighted in [Figure 3](#). The mean values and scatter are in broad agreement with similar work such as [Anders et al. \(2019\)](#). An illustration of the combined prior on number density, metallicity, and age for a specific line of sight is shown in [Figure 4](#).

### A.5. 3-D Dust Extinction

We assume the distribution of dust is independent of the distribution of stars and has a density of  $\rho_{\text{dust}}(d, \ell, b)$ . The impact of dust on the observed photometry for any particular star depends on the cumulative dust along a given LOS:

$$\begin{aligned} A_V(d|\ell, b) &= f_\theta \left( \int_0^d \rho_{\text{dust}}(d', \ell, b) dd' \right) \\ &\equiv f_\theta(N_{\text{dust}}(d|\ell, b)) \end{aligned} \quad (\text{A17})$$

where  $N_{\text{dust}}(d|\ell, b)$  is the column density out to distance  $d$  along the LOS defined by  $(\ell, b)$  and  $f_\theta(\cdot)$  is an unknown function that translates  $N_{\text{dust}}(d|\ell, b) \rightarrow A_V(d|\ell, b)$  into  $V$ -band extinction for a given stellar spectrum  $F_\nu(\lambda|\theta)$ . Typically  $f_\theta(N_{\text{dust}})$  is assumed to be roughly linear in  $N_{\text{dust}}$  and independent of stellar parameters. While this is unimportant for our purposes since we are placing a prior directly on  $A_V$  rather than  $\rho_{\text{dust}}$ , we hope to try to infer  $\rho_{\text{dust}}$  directly in future work.

We assume that the  $A_V$  for stars at roughly the same  $(d, \ell, b)$  are Normally distributed with mean  $\mu_A(d|\ell, b)$  and standard deviation  $\sigma_A(d|\ell, b)$ :

$$\pi(A_V|d, \ell, b) = \mathcal{N}[\mu_A(d|\ell, b), \sigma_A(d|\ell, b)] \quad (\text{A18})$$

We take the mean

$$\mu_A(d|\ell, b) = \frac{1}{N} \sum_{i=1}^N A_{V,i}^{\text{B19}}(d|\ell, b) \quad (\text{A19})$$

to be the sample mean computed from extinction realizations  $A_{V,i}^{\text{B19}}(d|\ell, b)$  taken from the 3-D dust map from [Green et al. \(2019\)](#) (i.e. [Bayestar19](#)) and the uncertainty

$$\sigma_A^2(d|\ell, b) = \frac{1}{N} \sum_{i=1}^N [A_{V,i}^{\text{B19}}(d|\ell, b) - \mu_A(d|\ell, b)]^2 + \Delta_A^2 \quad (\text{A20})$$

to be a combination of the sample variance computed from the same set of `Bayestar19` extinction realizations along with some intrinsic spread  $\Delta_A = 0.2$  mag based on comparisons from [Green et al. \(2019\)](#). This helps to account for both possible systematics in the underlying dust estimates (which were derived using particular stellar models; see §4.2) as well as small-scale dust structure below the current resolution of the `Bayestar19` dust map ([Zucker & Speagle et al. 2019](#)). Note that since `Bayestar19` is defined in terms of  $E(B - V) \equiv A_B - A_V$  (i.e. “reddening” rather than “extinction”), we convert from  $E(B - V)$  to  $A(V)$  as described in the `DUSTMAPS` package using the conversion factor from [Schlafly & Finkbeiner \(2011\)](#).

A summary of the parameters involved in our 3-D dust extinction prior is included in Table 1. An illustration is shown in Figure 5.

#### A.6. Variation in the Dust Extinction Curve

As described above, we allow the dust curve to vary linearly as a function of  $R_V$ . While results from [Schlafly et al. \(2016, 2017\)](#) suggest that  $R_V(d, \ell, b)$  varies as a function of 3-D position, the results are not available with the same fidelity and resolution of the 3-D `Bayestar19` dust map. As a result, in this work we consider variation in  $R_V$  to be independent of position. Following [Schlafly et al. \(2016\)](#), we approximate this variation using a Normal distribution

$$\pi(R_V) = \mathcal{N}[\mu_R, \sigma_R] \quad (\text{A21})$$

with a mean  $R_V$  of  $\mu_R = 3.32$  and standard deviation of  $\sigma_R = 0.18$ .

In practice, it is difficult to infer  $R_V$  variation from individual sources observed only in a handful of bands. Even at high signal-to-noise across  $\sim 8$  bands of optical and near-infrared (NIR) photometry, we find that  $R_V$  constraints improve over our prior by at most  $\sim 30 - 50\%$ . As such, we consider this component of our model mostly a means to accommodate systematic offsets between the models and the data and increase the uncertainty in the derived posteriors. We hope to explore modeling coherent 3-D  $R_V$  variation in future work (see also [Schlafly et al. 2017](#)).

The corresponding mean  $\mu_R$  and standard deviation  $\sigma_R$  are included in Table 1.

## B. IMPLEMENTATION DETAILS

We describe the motivation behind pursuing the overall approach described in §3 in §B.1. The strategy for performing linear regression over magnitude is described in §B.2. The subsequent expansion and linear regression in flux density is described in §B.3. The use of Monte Carlo sampling to incorporate priors is described in §B.4. Computing estimates and (re)sampling from the posterior over a given stellar grid is described in §B.5. Additional implementation details are discussed in §B.6.

### B.1. Motivation

In general, estimating posterior-based quantities tends to follow two approaches:

1. Sampling-based (i.e. Monte Carlo) approaches.
2. Grid-based (i.e. “brute force”) approaches.

Both have benefits and drawbacks, which we discuss briefly below.

Monte Carlo methods such as Markov Chain Monte Carlo (MCMC; [Brooks et al. 2011](#); [Sharma 2017](#); [Hogg & Foreman-Mackey 2018](#); [Speagle 2019](#)) or Nested Sampling ([Skilling 2004, 2006](#)) try to characterize the posterior distribution  $P(\boldsymbol{\theta}, \boldsymbol{\phi} | \hat{\mathbf{F}}, \hat{\boldsymbol{\omega}})$  by generating a set of  $n$  samples  $\{(\boldsymbol{\theta}_i, \boldsymbol{\phi}_i)\}_{i=1}^n$  along with a set of corresponding weights  $\{w_i\}_{i=1}^n$ . Expectation values (i.e. weighted averages) of functions  $f(\boldsymbol{\theta}, \boldsymbol{\phi})$  taken over the posterior

$$\mathbb{E}_P[f(\boldsymbol{\theta}, \boldsymbol{\phi})] \equiv \int f(\boldsymbol{\theta}, \boldsymbol{\phi}) P(\boldsymbol{\theta}, \boldsymbol{\phi} | \hat{\mathbf{F}}, \hat{\boldsymbol{\omega}}) d\boldsymbol{\theta} d\boldsymbol{\phi} \quad (\text{B22})$$

can then be estimated via:

$$\mathbb{E}_P[f(\boldsymbol{\theta}, \boldsymbol{\phi})] \approx \frac{\sum_{i=1}^n w_i \times f(\boldsymbol{\theta}_i, \boldsymbol{\phi}_i)}{\sum_{i=1}^n w_i} \quad (\text{B23})$$

While Monte Carlo methods allow us to in theory derive arbitrarily precise estimates for  $\mathbb{E}_P[f(\boldsymbol{\theta}, \boldsymbol{\phi})]$ , they suffer from two main drawbacks when trying to infer stellar properties from photometry:

1. Many of the posterior distributions for stars have multiple, widely-separated solutions due to the “dwarf-giant degeneracy” since main sequence (MS) stars (“dwarfs”) and post-MS stars (“giants”) can often have similar colors but very different luminosities. Many Monte Carlo methods struggle to characterize these types of multi-modal distributions efficiently.

2. We expect most posteriors to have extended and complex degeneracies since changes in  $\theta$  and  $\phi$  (e.g.,  $T_{\text{eff}}$  and  $A_V$ ) can impact observables in similar ways. Accurately characterizing these uncertainties will require more samples and/or longer run-times from Monte Carlo methods.

“Brute force” methods can get around these problem by computing the posterior probability  $P(\theta_i, \phi_i | \hat{\mathbf{F}}, \hat{\omega})$  over a large grid of  $n$  values  $\{(\theta_i, \phi_i)\}_{i=1}^n$ . These can then be used to estimate the expectation value in a similar way to our initial set of samples via

$$\mathbb{E}_P[f(\theta, \phi)] \approx \frac{\sum_{i=1}^n \Delta_i \times P(\theta_i, \phi_i | \hat{\mathbf{F}}, \hat{\omega}) \times f(\theta_i, \phi_i)}{\sum_{i=1}^n \Delta_i \times P(\theta_i, \phi_i | \hat{\mathbf{F}}, \hat{\omega})} \quad (\text{B24})$$

where  $\Delta_i = \prod_{j=1}^m \Delta_{i,j}$  is the volume of each element  $i$  of the grid with spacing  $\Delta_{i,j}$  for the  $j$ -th parameter (out of  $m$  total) at position  $(\theta_i, \phi_i)$ . For an evenly-spaced grid in each parameter,  $\Delta_i = \Delta$  is constant.

While grids scale extremely poorly ( $\propto e^p$ ) as the number of parameters  $p$  increases, for  $p \lesssim 4$  parameters grids often only comprise  $\sim 10^6$  elements that can be fit extremely quickly using modern computing architectures that excel at linear algebra operations. This often makes evaluating grids 1-2 orders of magnitude faster than sequentially generating samples via Monte Carlo methods. It also allows grids to be expansive enough to explore large regions of parameter space at fine enough resolution to characterize multiple modes robustly.

Unfortunately, when inferring stellar properties from photometry the number of parameters  $p$  is often  $\gtrsim 5$ . To get around this, grid-based approaches often either simplify the problem (see §2.1.1) and/or apply grids to only a few parameters at a time. This, however, often can underestimate uncertainties and possibly miss solutions.

To resolve these various difficulties, BRUTUS adopts a hybrid approach that exploits properties of our statistical model to combine grids, linear regression, and Monte Carlo methods to approximate the posterior. This allows us to exploit grids when possible to explore widely-separated modes while retaining the ability to construct accurate estimates of particular inferred quantities. These are described in more detail in the subsequent sections.

### B.2. Linear Regression in Magnitudes

The core of our approach centers on the fact that our initial model is essentially linear in the extrinsic parameters  $\phi$  since

$$\mu + A_V \times (\mathbf{R}_\theta + R_V \times \mathbf{R}'_\theta) \equiv \phi_{\text{mag}}^T \mathbf{D}_\theta \quad (\text{B25})$$

where we have slightly abused notation by defining the  $3 \times 1$  vector

$$\phi_{\text{mag}} = \begin{bmatrix} \mu \\ A_V \\ A_V \times R_V \end{bmatrix} \quad (\text{B26})$$

and

$$\mathbf{D}_\theta = \begin{bmatrix} \mathbf{1} \\ \mathbf{R}_\theta \\ \mathbf{R}'_\theta \end{bmatrix} \quad (\text{B27})$$

is the  $3 \times b$  “data-generating” matrix where  $\mathbf{1} = \{1\}_{i=1}^b$ .

Assuming our errors  $\sigma_{\mathbf{m}}$  on the magnitudes  $\hat{\mathbf{m}}$  are approximately Normal and defining  $\Delta \hat{\mathbf{m}}_\theta \equiv \hat{\mathbf{m}} - \mathbf{M}_\theta$ , the corresponding log-likelihood at fixed  $\theta$  is then

$$-2 \ln \mathcal{L}_{\text{mag}}(\phi_{\text{mag}} | \theta) = \left[ \Delta \hat{\mathbf{m}}_\theta - \phi_{\text{mag}}^T \mathbf{D}_\theta \right]^T \mathbf{C}_{\mathbf{m}}^{-1} \left[ \Delta \hat{\mathbf{m}}_\theta - \phi_{\text{mag}}^T \mathbf{D}_\theta \right] + \ln [\det (2\pi \mathbf{C}_{\mathbf{m}})] \quad (\text{B28})$$

If we want to solve for the maximum-likelihood estimate (MLE) for  $\phi_{\text{mag}}$ , we set the  $3 \times 1$  *Jacobian* vector  $\partial \ln \mathcal{L}_{\text{mag}} / \partial \phi_{\text{mag}} = \mathbf{0}$  and solve this linear system for  $\phi_{\text{mag}}^{\text{MLE}}$ . This gives

$$\phi_{\text{mag}}^{\text{MLE}}(\theta) = (\mathbf{D}_\theta \mathbf{C}_{\mathbf{m}}^{-1} \mathbf{D}_\theta^T)^{-1} \mathbf{D}_\theta \mathbf{C}_{\mathbf{m}}^{-1} \Delta \hat{\mathbf{m}}_\theta \quad (\text{B29})$$

Note that this is the standard solution for a *weighted least-squares linear regression* problem.

This result immediately implies that the conditional likelihood of  $\phi$  given  $\theta$  is

$$\mathcal{L}_{\text{mag}}(\phi_{\text{mag}} | \theta) = \underbrace{\mathcal{L}_{\text{mag}}^{\text{MLE}}(\theta) \times \det [2\pi \mathbf{C}_{\text{mag}}^{\text{MLE}}(\theta)]}_{\text{Normalization}} \times \underbrace{\mathcal{N} \left[ \phi_{\text{mag}}^{\text{MLE}}(\theta), \mathbf{C}_{\text{mag}}^{\text{MLE}}(\theta) \right]}_{\text{Distribution}} \quad (\text{B30})$$

In other words,  $\phi_{\text{mag}}$  is Normally distributed about the MLE  $\phi_{\text{mag}}^{\text{MLE}}(\boldsymbol{\theta})$  with a maximum amplitude of

$$\mathcal{L}_{\text{mag}}^{\text{MLE}}(\boldsymbol{\theta}) \equiv \mathcal{L}_{\text{mag}}(\boldsymbol{\theta}, \phi_{\text{mag}}^{\text{MLE}}(\boldsymbol{\theta})) \quad (\text{B31})$$

and a covariance of

$$\mathbf{C}_{\text{mag}}^{\text{MLE}}(\boldsymbol{\theta}) = (\mathbf{D}_{\boldsymbol{\theta}} \mathbf{C}_{\text{m}}^{-1} \mathbf{D}_{\boldsymbol{\theta}}^{\text{T}})^{-1} \quad (\text{B32})$$

$$= \left( \frac{\partial^2 \ln \mathcal{L}_{\text{mag}}(\phi_{\text{mag}} | \boldsymbol{\theta})}{\partial \phi_{\text{mag}}^2} \right)^{-1} \quad (\text{B33})$$

where  $\partial^2 \ln \mathcal{L}_{\text{mag}}(\phi_{\text{mag}} | \boldsymbol{\theta}) / \partial \phi_{\text{mag}}^2$  is the  $3 \times 3$  *Hessian* matrix whose elements are comprised of all the second-order derivatives. This correspondence between the covariance and the Hessian is a generic feature for Normal likelihoods. An example of this covariance structure in  $(\mu, A_V, R_V)$  is shown on the left side of Figure 18.

Given a prior/independent constraint  $\pi(\boldsymbol{\phi}) = \mathcal{N}[\boldsymbol{\phi}_{\pi}(\boldsymbol{\theta}), \mathbf{C}_{\pi}(\boldsymbol{\theta})]$  on our extrinsic parameters that are Normally distributed around mean  $\boldsymbol{\phi}_{\pi}(\boldsymbol{\theta})$  with covariance  $\mathbf{C}_{\pi}(\boldsymbol{\theta})$ , the corresponding posterior can also be shown to be Normal with a mean equal to the *maximum a posteriori* (MAP) estimate by solving

$$[\mathbf{C}_{\text{mag}}^{\text{MAP}}(\boldsymbol{\theta})]^{-1} \boldsymbol{\phi}_{\text{mag}}^{\text{MAP}}(\boldsymbol{\theta}) = [\mathbf{C}_{\text{mag}}^{\text{MLE}}(\boldsymbol{\theta})]^{-1} \boldsymbol{\phi}_{\text{mag}}^{\text{MLE}}(\boldsymbol{\theta}) + [\mathbf{C}_{\text{mag}}^{\pi}(\boldsymbol{\theta})]^{-1} \boldsymbol{\phi}_{\text{mag}}^{\pi}(\boldsymbol{\theta}) \quad (\text{B34})$$

where the (inverse) covariance is now

$$[\mathbf{C}_{\text{mag}}^{\text{MAP}}(\boldsymbol{\theta})]^{-1} = [\mathbf{C}_{\text{mag}}^{\text{MLE}}(\boldsymbol{\theta})]^{-1} + [\mathbf{C}_{\text{mag}}^{\pi}(\boldsymbol{\theta})]^{-1} \quad (\text{B35})$$

Unfortunately, we do not have (Normal) priors/independent constraints on  $\mu$ ,  $A_V$ , and  $A_V \times R_V$ , but rather on  $\varpi$ ,  $A_V(d|\ell, b)$ , and  $R_V$  separately. This poses a problem, since in practice we find that the MLE solution is unstable without independent constraints on  $R_V$ , with the reddening vector able to adjust to nonphysical values to better model the data.

We resolve this by breaking our problem into two parts. First, we neglect the contribution of any constraints on  $\mu$  or  $A_V$ , which are not Normal here, and only consider our prior  $\pi(R_V)$ . Then, we exploit the fact that this system of equations is linear in  $(\mu, A_V)$  at fixed  $R_V$ . Likewise, it is linear in  $(\mu, R_V)$  at fixed  $A_V$ . To find  $\boldsymbol{\phi}_{\text{mag}}^{\text{MLE}}$ , we therefore alternate between

- solving for  $(\mu, A_V)_{\text{MLE}}$  at fixed  $R_V$ , including the contribution from  $\pi(R_V)$ , and
- solving for  $(\mu, R_V)_{\text{MLE}}$  at fixed  $A_V$ .<sup>14</sup>

We iterate between the two until both  $A_V$  and  $R_V$  converge to within  $\delta_{A_V} = \delta_{R_V} = 0.05$ , which typically occurs within a handful of iterations. Our strategy for incorporating parallax measurements and other priors is described in §B.4 and §B.6.

Finally, even with these additional constraints, it is still possible that our MAP estimate for  $A_V$  and/or  $R_V$  will be unphysical (e.g.,  $A_V < 0$ ). To deal with these edge cases, by default the MAP for  $A_V$  is limited to be between  $A_{V,\text{min}} = 0$  and  $A_{V,\text{max}} = 6$  and the MAP for  $R_V$  to be between  $R_{V,\text{min}} = 1$  and  $R_{V,\text{max}} = 8$ . While these choices may lead to issues in regions with particularly high extinction, they can easily be changed through in-line arguments.

### B.3. Linear Regression in Flux Density

Above, we have assumed that the photometric errors are Normally distributed in *magnitudes* (i.e. log-flux). This is a reasonable approximation when the errors are small ( $\lesssim 5\%$ ), but lead to estimates and errors for parameters that are slightly different than when we assume errors are distributed following a Normal distribution in *flux density*.

For small changes  $\Delta A_V$  and  $\Delta R_V$  around a given value of  $\boldsymbol{\phi}$ , we can Taylor expand our previous linear model in magnitudes to get a model that is linear in flux density

$$\mathbf{F}_{\boldsymbol{\theta}, \boldsymbol{\phi}}(\Delta \boldsymbol{\phi}) \approx s \mathbf{F}_{\boldsymbol{\theta}, \boldsymbol{\phi}} \odot \left[ 1 - \frac{\ln 10}{2.5} \Delta A_V (\mathbf{R}_{\boldsymbol{\theta}} + \Delta R_V \mathbf{R}'_{\boldsymbol{\theta}}) \right] \quad (\text{B36})$$

<sup>14</sup> BRUTUS can also incorporate Normal priors on  $A_V$  if desired.



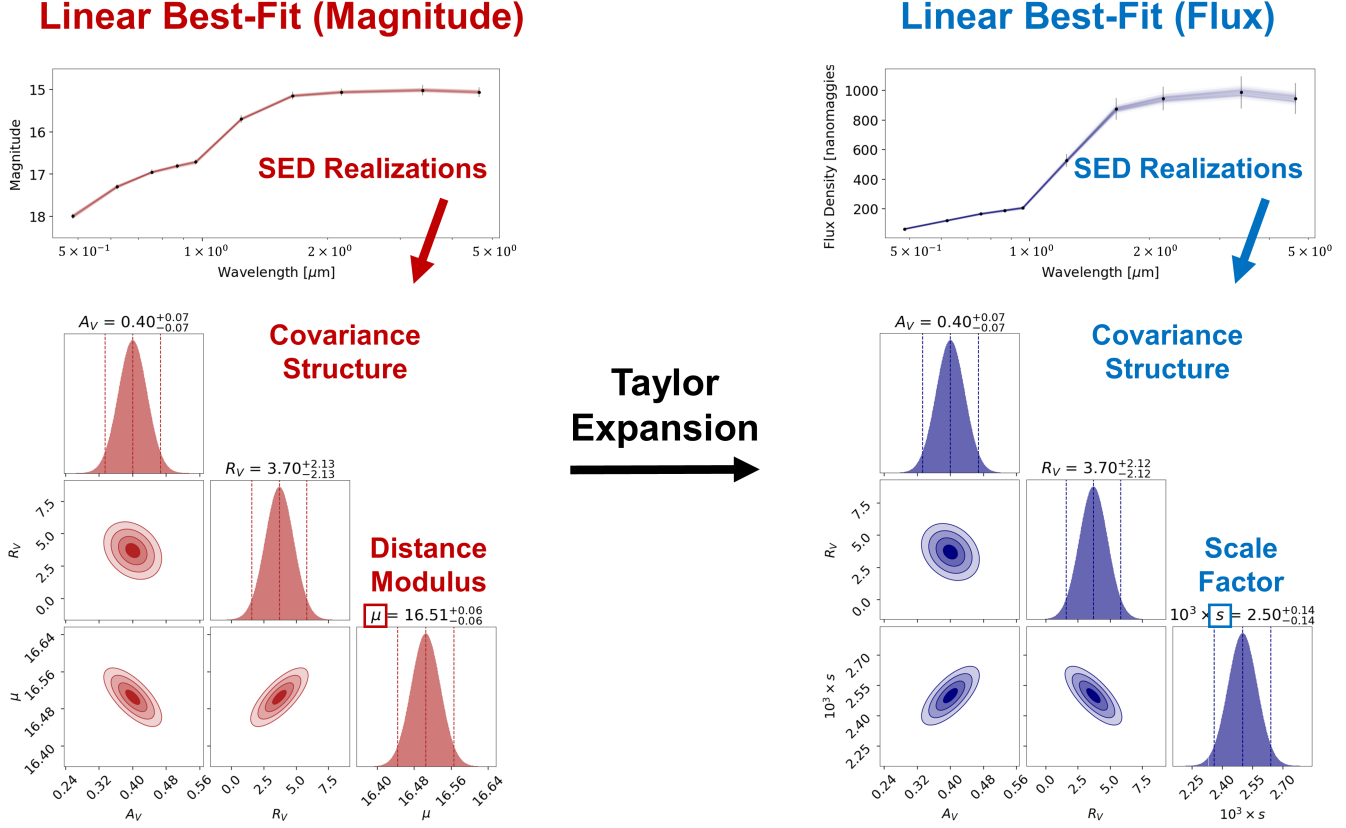


**Figure 18.** An illustration of the best-fit solutions from our linear model for a particular model SED with intrinsic parameters  $\theta$  when fitting for our extrinsic parameters  $\phi$  in magnitudes (see §B.2; left) and after Taylor expanding in flux density (see §B.3; right). The top panels show the measured SED and 2-sigma errors with realizations around the best-fit solution, while the bottom panels show 1-D and 2-D marginalized probability densities in dust extinction  $A_V$ , differential extinction  $R_V$ , and distance modulus  $\mu$  (left)/scale factor  $s$  (right). These highlight the different covariance structure between the two cases. Note that the scale factor  $s$  is directly related to the parallax  $\varpi$  via  $s = \varpi^2$ .

where  $\odot$  here indicates the Hadamard product (i.e. element-wise multiplication),  $\mathbf{F}_{\theta,\phi}$  is the “absolute” model flux density derived from the absolute model magnitudes  $\mathbf{M}_{\theta,\phi}$ , and  $s$  is now a scale factor that adjusts the normalization. Slightly abusing notation again and defining our parameters of interest to be

$$\Delta\phi_{\text{flux}} \equiv \begin{bmatrix} s \\ -s \frac{\ln 10}{2.5} \Delta A_V \\ -s \frac{\ln 10}{2.5} \Delta A_V \Delta R_V \end{bmatrix} \quad (\text{B37})$$

we can again rewrite the above model in matrix form as

$$\mathbf{F}_{\theta,\phi}(\Delta\phi_{\text{flux}}) \approx (\Delta\phi_{\text{flux}})^T \mathbf{D}_{\theta,\phi} \quad (\text{B38})$$

where

$$\mathbf{D}_{\theta,\phi} = \begin{bmatrix} \mathbf{F}_{\theta,\phi} \\ \mathbf{F}_{\theta,\phi} \\ \mathbf{F}_{\theta,\phi} \end{bmatrix} \odot \begin{bmatrix} \mathbf{1} \\ \mathbf{R}_{\theta} \\ \mathbf{R}'_{\theta} \end{bmatrix} \quad (\text{B39})$$

Our log-likelihood then is

$$-2 \ln \mathcal{L}_{\text{flux}}(\Delta\phi_{\text{flux}} | \theta, \phi) = \left[ \hat{\mathbf{F}} - (\Delta\phi_{\text{flux}})^T \mathbf{D}_{\theta,\phi} \right]^T \mathbf{C}_{\mathbf{F}}^{-1} \left[ \hat{\mathbf{F}} - (\Delta\phi_{\text{flux}})^T \mathbf{D}_{\theta,\phi} \right] + \ln [\det (2\pi \mathbf{C}_{\mathbf{F}})] \quad (\text{B40})$$

As §B.2, this implies the conditional likelihood is analytic such that

$$\mathcal{L}_{\text{flux}}(\Delta\phi_{\text{flux}}|\theta, \phi) = \underbrace{\mathcal{L}_{\text{flux}}^{\text{MLE}}(\theta, \phi) \times \det[2\pi\mathbf{C}_{\text{flux}}^{\text{MLE}}(\theta, \phi)]}_{\text{Normalization}} \times \underbrace{\mathcal{N}[\Delta\phi_{\text{flux}}^{\text{MLE}}(\theta, \phi), \mathbf{C}_{\text{flux}}^{\text{MLE}}(\theta, \phi)]}_{\text{Distribution}} \quad (\text{B41})$$

where  $\mathcal{L}_{\text{flux}}^{\text{MLE}}(\theta, \phi)$  is again evaluated at the MLE, the mean is

$$\Delta\phi_{\text{flux}}^{\text{MLE}}(\theta, \phi) = (\mathbf{D}_{\theta, \phi} \mathbf{C}_{\mathbf{F}}^{-1} \mathbf{D}_{\theta, \phi}^{\text{T}})^{-1} \mathbf{D}_{\theta, \phi} \mathbf{C}_{\mathbf{F}}^{-1} \hat{\mathbf{F}} \quad (\text{B42})$$

and the covariance is

$$\mathbf{C}_{\text{flux}}^{\text{MLE}}(\theta, \phi) = (\mathbf{D}_{\theta, \phi} \mathbf{C}_{\mathbf{F}}^{-1} \mathbf{D}_{\theta, \phi}^{\text{T}})^{-1} \quad (\text{B43})$$

As with §B.2, in the presence of (Normal) priors/independent constraints, the MAP estimates  $\Delta\phi_{\text{flux}}^{\text{MAP}}(\theta, \phi)$  and  $\mathbf{C}_{\text{flux}}^{\text{MAP}}(\theta, \phi)$  are straightforward to derive. Similarly, due to the constraints on  $R_V$  needed for the solution to be well-behaved, we solve for elements of  $\Delta\phi_{\text{flux}}$  iteratively conditioning on  $A_V$  and  $R_V$  in turn.

As the data  $\hat{\mathbf{F}}$  are fundamentally in flux density space, we are ultimately interested in constraining our parameters relative to our linear model in flux density  $\mathbf{F}_{\theta, \phi}(\Delta\phi)$ . We therefore will redefine our earlier set of extrinsic parameters as

$$\phi \equiv \begin{bmatrix} s \\ A_V \\ R_V \end{bmatrix} \quad (\text{B44})$$

where the only change relative to our original parameters is that now we are inferring the scale-factor  $s$  rather than the distance modulus  $\mu$ . Note that it is straightforward to convert from  $\phi_{\text{mag}}$  and  $\Delta\phi_{\text{flux}}$  to  $\phi_{\text{flux}}$  and  $\phi$ . Around the true MAP solution  $\phi_{\text{MAP}}(\theta)$  where  $\Delta\phi = (0, 0, 0)$ , we can compute  $\mathbf{C}_{\text{MAP}}(\theta)$  by explicitly computing the corresponding Hessian matrix of second-order derivatives. An example showing the covariance structure in  $(s, A_V, R_V)$  versus that in  $(\mu, A_V, R_V)$  from §B.2 is shown in Figure 18.

Altogether, this gives us a straightforward recipe for “optimizing” our initial MAP solution, derived from magnitudes, to the corresponding distribution in flux:

1. Starting from an initial guess of  $A_V = 1$ ,  $R_V = 3.32$ , derive  $\phi_{\text{mag}}^{\text{MAP}}(\theta)$ . Iterate in  $(\mu, A_V)$  and  $(\mu, R_V)$  until convergence.
2. Convert from  $\phi_{\text{mag}}^{\text{MAP}}(\theta) \rightarrow \phi_{\text{MAP}}(\theta)$  and expand around  $\phi_{\text{MAP}}(\theta)$  to derive  $F_{\theta, \phi}(\Delta\phi)$ .
3. Compute first order corrections  $\Delta\phi_{\text{MAP}}(\theta, \phi)$  for  $s$ ,  $A_V$ , and  $R_V$ .
4. Compute the new MAP solution  $\phi_{\text{MAP}}^{\text{new}} = \phi_{\text{MAP}} + \Delta\phi_{\text{MAP}}(\theta, \phi)$ .
5. Repeat steps 2-4 starting from  $\phi_{\text{MAP}}^{\text{new}}$  until the likelihood converges.

In general, we find the likelihood quickly converges after only a handful of iterations.

#### B.4. Incorporating Priors with Importance Sampling

We are interested in estimating expectation values (see §B.1) over the *conditional posterior*

$$P(\phi|\theta, \hat{\mathbf{F}}, \hat{\omega}) = \mathcal{L}_{\text{phot}}(\phi|\theta) \mathcal{L}_{\text{astr}}(\phi) \pi(\phi|\theta) \quad (\text{B45})$$

From our above calculations, we now have an analytic approximation for  $\mathcal{L}_{\text{phot}}(\phi|\theta)$ . Critically, we now know that, conditional on  $\theta$ ,  $\phi$  is approximately distributed as

$$\phi(\theta) \sim \mathcal{N}[\phi_{\text{MAP}}(\theta), \mathbf{C}_{\text{MAP}}(\theta)] \quad (\text{B46})$$

and therefore easy to simulate. Given a set of  $m$  independently and identically distributed (iid) samples  $\{\phi_i\}_{i=1}^m \sim \mathcal{N}[\phi_{\text{MAP}}(\theta_i), \mathbf{C}_{\text{MAP}}(\theta_i)]$  drawn from this Normal distribution at a particular value  $\theta_i$ , we can then approximate expectation values over posterior using a Monte Carlo approach through *Importance Sampling* via

$$\begin{aligned} \mathbb{E}_P[f(\phi|\theta_i)] &= \int f(\phi|\theta_i) P(\phi|\theta_i, \hat{\mathbf{F}}, \hat{\omega}) d\phi \\ &\approx \frac{1}{m} \sum_{j=1}^m q_{i,j} \times f(\phi_j|\theta_i) \end{aligned} \quad (\text{B47})$$

where the importance weight  $q_{i,j}$  for each sample  $\phi_{i,j}$  is defined as

$$q_{i,j} \equiv \frac{P(\phi_j|\theta_i, \hat{\mathbf{F}}, \hat{\omega})}{\mathcal{L}_{\text{phot}}(\phi_j|\theta_i)} = \mathcal{L}_{\text{astr}}(\phi_j)\pi(\phi_j|\theta_i) \quad (\text{B48})$$

Generally, we find that for  $n_{\text{prior}} \gtrsim 30$  samples our estimates of the integrated conditional probability for a particular model

$$q_i \equiv \int P(\phi|\theta_i, \hat{\mathbf{F}}, \hat{\omega}) d\phi \approx \frac{1}{m} \sum_{j=1}^m q_{i,j} \quad (\text{B49})$$

tend to roughly converge. As a result, we choose  $n_{\text{prior}} = 50$  as the default number of samples in our computations. This step, which requires generating a large number of samples for every un-clipped model in our initial grid and subsequently evaluating the astrometric likelihood and Galactic prior for each sample, typically takes up the majority of the computation time.

### B.5. Application over Stellar Parameter Grids

Above, we showed that we can analytically solve for the conditional likelihood  $\mathcal{L}_{\text{phot}}(\phi|\theta)$ , which implies that we should be able to generate estimates for those parameters without the use of grids over  $\phi$ . This allows us to both substantially improve our resolution in both  $\theta$  (over our grid) and  $\phi$  (with analytic sampling). In addition, we simultaneously decrease the required computation since we only require a grid of  $n$  values  $\{\theta_i\}_{i=1}^n$  over the  $m \lesssim 4$  intrinsic set of stellar parameters  $\theta$  rather than over the  $m+3$  parameters from both  $\theta$  and  $\phi$ .

We can exploit such a grid by noting that our original posterior can be rewritten as

$$P(\theta, \phi|\hat{\mathbf{F}}, \hat{\omega}) = P(\phi|\theta, \hat{\mathbf{F}}, \hat{\omega})P(\theta|\hat{\mathbf{F}}, \hat{\omega}) \quad (\text{B50})$$

for a given  $\theta$ . This then implies that we can generate random samples from our joint likelihood in two steps. First, we draw a random sample  $\theta'$  from  $P(\theta|\hat{\mathbf{F}}, \hat{\omega})$ . Then, we draw a corresponding random sample  $\phi'$  from  $P(\phi|\theta', \hat{\mathbf{F}}, \hat{\omega})$ . More formally,

$$\begin{aligned} \theta' &\sim P(\theta|\hat{\mathbf{F}}, \hat{\omega}) \\ \phi' &\sim P(\phi|\theta', \hat{\mathbf{F}}, \hat{\omega}) \end{aligned}$$

We exploit the weighted Monte Carlo samples from §B.4 to perform this operation using a *bootstrap approximation*. For a particular grid point  $\theta_i$ , generating a random sample  $\phi'$  from the conditional posterior  $P(\phi|\theta_i, \hat{\mathbf{F}}, \hat{\omega})$  is roughly equivalent to picking one of the already-generated set of  $m$  samples  $\{\phi_{i,j}\}_{j=1}^{j=m}$  with a probability proportional to its weight  $q_{i,j}$ . More formally, this implies

$$\phi' \sim \text{Cat} \left[ \{\phi_{i,j}\}_{j=1}^{j=m}, \{q_{i,j}/q_i\}_{j=1}^{j=m} \right] \quad (\text{B51})$$

where  $\text{Cat}[\mathbf{x}, \mathbf{p}]$  is the *Categorical distribution* over  $\mathbf{x} = \{x_j\}_{j=1}^{j=m} = \{\phi_{i,j}\}_{j=1}^{j=m}$  with corresponding probabilities  $\mathbf{p} = \{p_j\}_{j=1}^{j=m} = \{q_{i,j}/q_i\}_{j=1}^{j=m}$  and again  $q_i = \sum_j q_{i,j}$  is the total conditional probability.

Likewise, we can approximate drawing a sample  $\theta'$  from  $P(\theta|\hat{\mathbf{F}}, \hat{\omega})$  using the same strategy by taking

$$\theta' \sim \text{Cat} \left[ \{\theta_i\}_{i=1}^{i=n}, \{p_i/p\}_{i=1}^{i=n} \right] \quad (\text{B52})$$

The prior-weighted probability  $p_i$  corresponding to a given  $\theta_i$  is related to our previous  $q_i$  via

$$p_i \equiv q_i \times \pi_i \times \Delta_i \quad (\text{B53})$$

where  $\pi_i = \pi(\theta_i)$  is the prior probability evaluated at  $\theta_i$  and  $\Delta_i$  is the associated grid spacing. The normalization

$$p \equiv \sum_i p_i \approx \int P(\phi, \theta|\hat{\mathbf{F}}, \hat{\omega}) d\phi d\theta \quad (\text{B54})$$

is then the estimated marginal likelihood (i.e. the Bayesian evidence) for the source, which in theory may be useful for model comparisons in future applications.

Using this strategy, we post-process our MAP fits and Monte Carlo samples over our grid points to generate  $n_{\text{post}} = 250 \{(\theta_k, \phi_k)\}_{k=1}^{k=n_{\text{post}}}$  samples that serve as rough approximations to the underlying posterior  $P(\theta, \phi|\hat{\mathbf{F}}, \hat{\omega})$ . In particular, we wish to emphasize that these options only generate *approximations* to the underlying posterior. We expect the largest differences between the estimated posterior relative to the true distribution will be primarily due to

**Table 6.** Default settings for hyper-parameters used when deriving posterior estimates with BRUTUS.

Description	Symbol	Value
<b>Bounds</b>		
Minimum allowed $A_V$	$A_{V,\min}$	0 mag
Maximum allowed $A_V$	$A_{V,\max}$	6 mag
Minimum allowed $R_V$	$R_{V,\min}$	1
Maximum allowed $R_V$	$R_{V,\max}$	8
<b>Magnitude Step</b>		
Tolerance in $A_V$	$\delta_{A_V}$	0.05 mag
Tolerance in $R_V$	$\delta_{R_V}$	0.05
Relative likelihood tolerance threshold	$f_{\text{tol}}^{\text{mag}}$	0.005
<b>Flux Step</b>		
Relative likelihood threshold	$f_{\text{init}}^{\text{flux}}$	0.005
Tolerance in $\mathcal{L}_{\text{phot}}$	$\delta_{\mathcal{L}}$	0.03
Relative likelihood tolerance threshold	$f_{\text{tol}}^{\text{flux}}$	0.01
<b>Monte Carlo Step</b>		
Relative posterior threshold	$f_{\text{post}}$	0.005
Number of samples used for integration	$n_{\text{prior}}$	50
Number of resampled posterior draws to save	$n_{\text{post}}$	250

- grid resolution effects in  $\theta$ ,
- “posterior noise” caused by noisy estimates of the  $p_i$ ’s, and
- “resampling noise” due to the procedure used to resample the final set of  $n_{\text{post}}$  samples.

See §6 for examples of the impact these may have on inferring underlying relevant intrinsic and extrinsic stellar properties. An example of the output stellar parameters and the associated SED can be seen in Figure 7.

### B.6. Additional Implementation Details

At multiple points during the fitting process we apply cuts to decrease the effective size of the stellar parameter grid we are dealing with in order to reduce the overall run time. The choices we take are summarized below. The relevant parameters associated with them are listed in Table 6. The general procedure is shown in Figure 6.

#### B.6.1. Magnitude Step

While models that are reasonable fits to the data generally converge quickly, the  $A_V$  and  $R_V$  values for models that are poor fits can sometimes be ill-behaved. As a result, we only worry about convergence for objects with likelihoods whose values are greater than  $f_{\text{tol}}^{\text{mag}} = 0.005$  times the maximum value after the first linear regression step. We consider our fits converged when the maximum variation in  $A_V$  and  $R_V$  over these “reasonably fit” models falls below  $\delta_{A_V} = 0.05$  mag and  $\delta_{R_V} = 0.05$ , respectively, between one iteration and the next. This usually occurs within  $\lesssim 5$  iterations.

### B.6.2. Flux Density Step

After our magnitude fits have converged, we only want to perform additional optimization after expanding in flux density for a smaller subset of grid points, indexed by  $i$ , that give “good” likelihoods. Using the MLE values for  $\{\phi_{\text{MLE},i}\}_{i=1}^n$ , we compute the corresponding photometric likelihood  $\mathcal{L}_{\text{phot}}(\theta_i, \phi_{\text{MLE},i})$  and, if it is measured, an astrometric likelihood  $\mathcal{L}_{\text{astr}}(\phi_{\text{MLE},i})$  for each object. We only perform the subsequent flux density expansion and optimization for objects with combined astro-photometric likelihoods that are within  $f_{\text{init}}^{\text{flux}} = 0.005$  times the maximum value. This further screens models that may provide good fits to the photometry but give inconsistent parallax estimates.

As with our magnitude step, we only consider convergence over a set of “reasonably fit” models with likelihoods greater than  $f_{\text{tol}}^{\text{flux}} = 0.01$  the current maximum value in order to avoid being overly-sensitive to the worst-fit models under consideration (i.e. to decrease our sensitivity to the likely tails of the distribution). We take our fits to be converged after the change in the photometric log-likelihood  $\ln \mathcal{L}_{\text{phot}}(\theta_i, \phi_{\text{MLE},i})$  between iterations falls below  $\delta_{\mathcal{L}} = 0.03$ . As in §B.6.1, this usually occurs within  $\lesssim 5$  iterations.

### B.6.3. Monte Carlo Step

Since generating samples for all of our models is both time-consuming and memory-intensive over large grids, we only want to perform this step (and the subsequent resampling) over a small subset of models. We subselect these based on their “expected” posterior probabilities, which we compute in two steps.

First, we ignore all distance-dependent effects such as our 3-D priors over stellar properties and dust extinction. The remaining “static” contributions of our prior are then direct functions of our underlying grid of stellar parameters  $\{\theta_i\}_{i=1}^n$  and can therefore be pre-computed. This includes contributions from the spacing of our grid points  $\{\Delta_i\}_{i=1}^n$  (see §B.1) and the associated IMF prior over mass  $\pi(M_{\text{init}})$ .

Second, we again want to incorporate possible constraints from the measured parallax. Unlike in §B.6.2, however, we now want to incorporate uncertainties  $\sigma_s(\theta_i)$  in the inferred scale-factor  $s(\theta_i)$  for a particular model  $\theta_i$ . The marginal distribution of  $s(\theta_i)$  derived from  $\mathcal{L}_{\text{phot}}(\phi|\theta_i)$  is Normal:

$$s(\theta_i) \sim \mathcal{N}[\mu_s(\theta_i), \sigma_s^2(\theta_i)] \quad (\text{B55})$$

where  $\mu_s(\theta_i)$  and  $\sigma_s(\theta_i)$  are just taken from the appropriate elements of  $\phi_{\text{MAP}}(\theta_i)$  and  $\mathbf{C}_{\text{MAP}}(\theta_i)$ . It is straightforward to show that the inferred scale-factor  $s(\theta_i)$  is simply the square of the associated parallax  $\varpi(\theta_i)$ :

$$s(\theta_i) = \varpi^2(\theta_i) \quad (\text{B56})$$

In the case where the measured parallax  $\hat{\varpi}$  is Normally distributed with at least a moderate signal-to-noise ratio (SNR) (i.e.  $\hat{\varpi}/\sigma_{\varpi} \gg 1$ ), it is straightforward to show that the  $\varpi^2(\theta_i)$  is also expected to be approximately Normally distributed such that

$$\varpi(\theta_i) \sim \mathcal{N}[\hat{\varpi}, \sigma_{\varpi}^2] \Rightarrow \varpi^2(\theta_i) \sim \mathcal{N}[\mu_{\varpi^2}, \sigma_{\varpi^2}^2] \quad (\text{B57})$$

where  $\mu_{\varpi^2} = \hat{\varpi}^2 + \sigma_{\varpi}^2$  and  $\sigma_{\varpi^2} = 2\sigma_{\varpi}^4 + 4\hat{\varpi}^2\sigma_{\varpi}^2$ . We take our likelihood  $\mathcal{L}_s(\theta)$  for  $s$  to be the convolution of this distribution with the MAP uncertainties assuming the parallax SNR is above a minimum SNR threshold  $\varpi_{\text{SNR}}^{\text{min}}$  and uniform otherwise:

$$\mathcal{L}_s(\theta) = \begin{cases} 1 & \hat{\varpi}/\sigma_{\varpi} < \varpi_{\text{SNR}}^{\text{min}} \\ \mathcal{N}[\mu_{\varpi^2}, \sigma_{\varpi^2}^2 + \sigma_s^2(\theta)] & \hat{\varpi}/\sigma_{\varpi} \geq \varpi_{\text{SNR}}^{\text{min}} \end{cases} \quad (\text{B58})$$

We find  $\varpi_{\text{SNR}}^{\text{min}} = 4$  to be a reasonable threshold where this approximation remains valid to  $\sim 10\%$ .

After applying these two terms to the photometric likelihoods computed from our earlier steps, we then select the small subset of models (often  $\lesssim 1\%$  of the original grid) with expected posterior probabilities greater than  $f_{\text{post}} = 0.005$  that of the maximum computed value. We then perform the Monte Carlo integration and resampling procedure described in §B.4 using  $n_{\text{prior}} = 50$  samples per selected model and saving a total of  $n_{\text{post}} = 250$  posterior samples.

### B.6.4. Runtime

Overall, we find that for grids with  $n \sim 7.5 \times 10^5$  models, BRUTUS is able to perform full posterior estimation in  $\lesssim 5-10$  seconds when fitting  $\sim 5-10$  bands of photometry with low-to-moderate SNR parallax measurements. This is comparable to the “rough” version of STARHORSE described in Anders et al. (2019) while giving continuous resolution in the extrinsic parameters  $\phi$  and reasonable resolution over the intrinsic stellar parameters  $\theta$  (see §4).

Due to the adaptive thresholding, Monte Carlo (re)sampling, and use of parallax measurements, the scaling tends to be non-linear in the number of bands and the size of the grid. For smaller grids of  $n \sim 4 \times 10^4$  elements (as in §4.2),



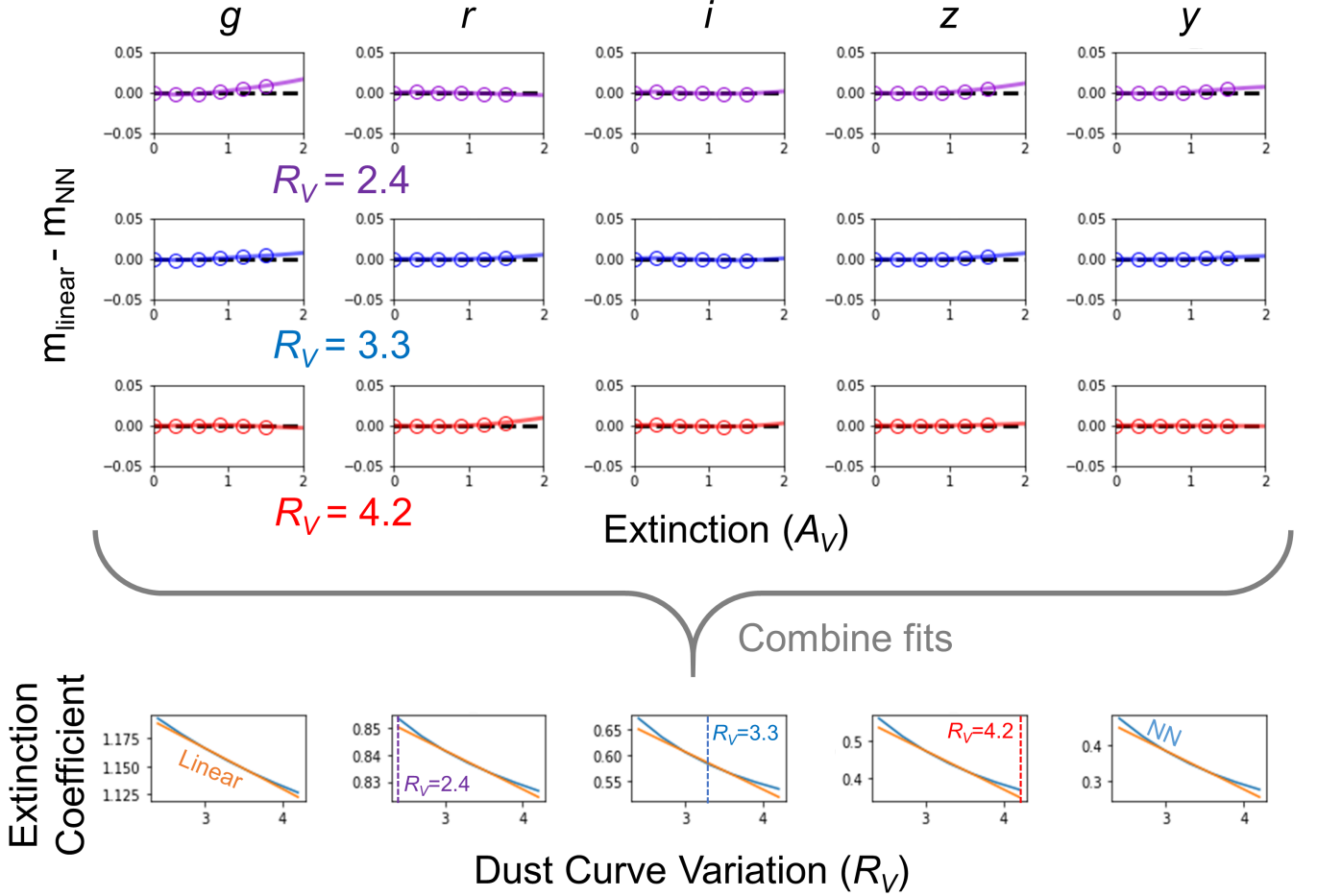


**Figure 19.** An illustration of the linear reddening approximation used in BRUTUS for the MIST models with the Fitzpatrick (2004)  $R_V$ -dependent reddening curve in the Pan-STARRS  $g$ ,  $r$ ,  $i$ ,  $z$ , and  $y$  filters. First, photometry in each filter is generated using a neural network (NN) trained on the grid of C3K model atmospheres summarized in Table 3 over a grid of  $A_V$  values (open circles) at fixed  $R_V$ . The resulting magnitudes are then fit using weighted linear regression. Deviations between the linear predictions ( $m_{\text{linear}}$ ) and the NN baseline ( $m_{\text{NN}}$ ) for values of  $R_V = 2.4$  (purple),  $R_V = 3.3$  (blue), and  $R_V = 4.2$  (red) are highlighted in the first three rows. We then perform weighted linear regression over the set of fitted linear extinction coefficients. The resulting linear fits (orange) and the baseline NN predictions (light blue) are shown in the bottom row. See §4.1.3 for additional details.

the typical runtime is  $\sim 1$  second, while for much larger grids of  $n \sim 2 \times 10^6$  elements the typical runtime can range from  $\sim 20 - 40$  seconds. With tight parallax constraints, runtimes can be up to an order of magnitude faster (down to  $\sim 0.1$  seconds).

### C. LINEAR REDDENING APPROXIMATION

We approximate the linear  $A_V$  and  $R_V$  vector in two steps:

1.  $A_V$  step: At fixed  $R_V$ , we compute the absolute magnitudes  $\{\mathbf{M}_{\theta}(A_{V,i}|R_V)\}_{i=1}^m$  over a grid of  $m$   $A_V$  values from  $A_V = 0$  to  $A_V = 1.5$  with a resolution of  $\Delta A_V = 0.3$ . We then perform weighted linear regression over the grid points where each point is assigned a weight

$$w(A_V) = (10^{-5} + A_V)^{-1} \quad (\text{C59})$$

This ensures the fit essentially goes through  $A_V = 0$  with the  $A_V > 0$  grid points assigned a weight inversely proportional to the extinction. This then provides a set of reddening vectors  $\mathbf{R}_{\theta}(R_V)$  as a function of  $R_V$ .

2.  $R_V$  step: We compute  $\mathbf{R}_\theta(R_V)$  over a grid of  $R_V$  values from  $R_V = 2.4$  to  $4.2$  with a resolution of  $\Delta R_V = 0.3$ . Then, we perform weighted linear regression over the  $R_V$  grid points where each point is assigned a weight of

$$w(R_V) = \exp(-|R_V - 3.3|/0.5) \quad (\text{C60})$$

This gives maximum weight to the grid point at  $R_V = 3.3$  and exponentially declining weight for grid points with larger/smaller  $R_V$  to ensure we best reproduce the behavior for “typical”  $R_V$  values. This procedure then provides a set of  $\mathbf{R}_\theta$  and  $\mathbf{R}'_\theta$  associated with each  $\mathbf{M}_\theta$ .

An example of this overall procedure and the accuracy of these linear approximations for a solar-like star over several filters is shown in Figure 19. Overall, we find agreement at the few percent level across a wide range of  $A_V$  and  $R_V$  values.

## D. CLUSTER MODELING

We build up the basic components of our cluster model below. In §D.1, we outline our baseline model. In §D.2, we introduce our approach for modeling unresolved (non-interacting) binaries. In §D.3, we describe our approach for dealing with cluster contamination and/or alternate stellar populations. In §D.4, we describe the additional parameters used to add empirical corrections to underlying isochrones derived from the MIST models. We finally describe additional empirical photometric corrections in §D.5.

### D.1. Baseline Model

Assuming that an open cluster can be effectively approximated by a simple stellar population (SSP), all stars in the cluster have identical initial metallicities  $[\text{Fe}/\text{H}]_{\text{init}}$  and ages  $t_{\text{age}}$  but have initial masses  $M_{\text{init}}$  that have been independently sampled from the stellar IMF. We further assume that stars are located at approximately the same distance  $d$  and are co-spatial on the sky that they are behind the same screen of dust (i.e. all have the same  $A_V$  and  $R_V$ ). We will collectively refer to these “cluster-level” parameters as  $\theta_{\text{cluster}}$ . The log-posterior over  $n$  photometric sources  $\{\hat{\mathbf{F}}_i\}_{i=1}^{i=n}$  is then proportional to the product of the likelihoods and priors for each source plus the prior over the cluster-level parameters:

$$P(\{M_{\text{init},i}\}_{i=1}^{i=n}, \theta_{\text{cluster}} | \{\hat{\mathbf{F}}_i\}_{i=1}^{i=n}) \propto \pi(\theta_{\text{cluster}}) \prod_{i=1}^n \mathcal{L}_i(M_{\text{init},i} | \theta_{\text{cluster}}) \pi(M_{\text{init},i}) \quad (\text{D61})$$

$$\equiv \pi_{\text{cluster}} \times \prod_{i=1}^n \mathcal{L}_i \times \pi_i \quad (\text{D62})$$

We want the likelihoods of each individual source to incorporate information from various sources when available without implicitly favoring objects with greater/fewer measurements. As a result, we consider our likelihood for each object to follow the  $\chi^2$ -distribution, which is substantially less sensitive compared to the Normal distribution to changes in dimensionality. Our likelihood is then defined as

$$\mathcal{L}_i \equiv \frac{(\chi_i^2)^{k_i/2-1} e^{-\chi_i^2/2}}{2^{k_i/2} \Gamma(k_i/2)} \quad (\text{D63})$$

where  $k_i$  is the effective number of data points ( $b_i$  bands of photometry plus an optional parallax measurement),  $\Gamma(\cdot)$  is the Gamma function, and

$$\chi_i^2 \equiv \sum_{j=1}^{b_i} \frac{(\hat{F}_{i,j} - F_{i,j})^2}{\sigma_{F,i,j}^2} + \frac{(\hat{\omega}_i - 1/d)^2}{\sigma_{\omega,i}^2} \quad (\text{D64})$$

is the “standard”  $\chi^2$ -statistic as a function of the model photometry  $\mathbf{F}_i$  for each object  $i$  given  $M_{\text{init},i}$  and  $\theta_{\text{cluster}}$ .

For our baseline model, we assume that our prior is uniform within some specific range of allowed  $\theta_{\text{cluster}}$  and  $M_{\text{init}}$  values such that  $\pi_{\text{cluster}}$  and  $\{\pi_i\}_{i=1}^{i=n}$  are constant. While this assumption is not entirely accurate (e.g., it does not apply constraints from the IMF), it drastically simplifies the problem since in practice we do not know  $\{M_{\text{init},i}\}_{i=1}^{i=n}$  or other associated parameters for each source. While proper inference requires utilizing a full hierarchical model (e.g., von Hippel et al. 2006; De Gennaro et al. 2009; van Dyk et al. 2009) to estimate both  $\theta_{\text{cluster}}$  and  $\{M_{\text{init},i}\}_{i=1}^{i=n}$ , we instead simply marginalize over the latter to get

$$P(\theta_{\text{cluster}} | \{\hat{\mathbf{F}}_i\}_{i=1}^{i=n}) \propto \prod_{i=1}^n \int_{M_{\text{min}}}^{M_{\text{max}}} \mathcal{L}_i(M_{\text{init}} | \theta_{\text{cluster}}) dM_{\text{init}} \quad (\text{D65})$$

where  $M_{\min} = 0.3 M_{\odot}$  (the minimum mass where the MIST models are well-behaved) and  $M_{\max} = 100 M_{\odot}$  (the standard upper limit for the IMF).

As described in [Dotter \(2016\)](#), isochrones are more evenly sampled in EEP than in  $M_{\text{init}}$ . As a result, we opt to evaluate this integral using a grid in EEP. Similar to §4.1.1, we account for the unequal spacing in  $M_{\text{init}}$  using second-order numerical derivatives in  $\Delta M_{\text{init}}/\Delta \text{EEP}$ . By default, we use a grid of  $n = 2000$  evenly-spaced values between  $\text{EEP} = 202$  and 808, which spans the beginning of the MS to the beginning of the thermally-pulsing asymptotic giant branch.

We wish to note that the approach taken here is substantially different from the analysis of binned ‘‘Hess Diagrams’’ commonly used in the literature (see, e.g., [Dolphin 1997, 2002](#); [de Jong et al. 2008](#); [Weisz et al. 2011](#); [Gouliermis et al. 2011](#); [Gossage et al. 2018](#)). While the current approach requires simpler models, it has the benefit of not being sensitive to any issues related to binning over the CMD and can jointly model *all* observed bands rather than just 2-3 at a time. More complex star formation histories beyond SSPs can also be explored through the use of, e.g., inhomogeneous Poisson processes (see, e.g., [Leja et al. 2019](#)), although we defer any such improvements to future work.

This baseline model is shown in the first panel of [Figure 10](#).

### D.2. Binaries

As clusters display prominent binary sequences, we explicitly consider the case where a given source could be an unresolved binary with a primary mass of  $M_{\text{init}}$  and a binary companion with secondary mass fraction  $q \in [0, 1]$ , where  $q = 0$  is equivalent to a single source and  $q = 1$  is an equal-mass binary. Marginalizing over both  $M_{\text{init}}$  and  $q$  then gives

$$P(\boldsymbol{\theta}_{\text{cluster}} | \{\hat{\mathbf{F}}_i\}_{i=1}^n) \propto \prod_{i=1}^n \int_{M_{\min}}^{M_{\max}} \int_0^1 \mathcal{L}_i(M_{\text{init}}, q | \boldsymbol{\theta}_{\text{cluster}}) \pi(M_{\text{init}}, q | \boldsymbol{\theta}_{\text{cluster}}) dM_{\text{init}} dq \quad (\text{D66})$$

We evaluate this integral in  $q$  using an adaptively-spaced grid of  $n = 14$  values from  $q = 0$  to 1 with a resolution that ranges from  $\Delta q = 0.2$  near the edges to  $\Delta q = 0.05$  around  $q = 0.6$ .

Compared to §D.1, incorporating binaries involves dealing with a few additional subtleties. First, we only can model binaries down to  $M_{\min}$ . This means that while the likelihood for  $q = 0$  (i.e. a single star) is defined, the likelihood from  $0 < q < M_{\min}/M_{\text{init}}$  is undefined. Second, close (unresolved) binaries generally only exist when the primary (higher-mass) binary companion has not yet evolved off the MS, since this process tends to decouple the system. As a result, our likelihood as a function of  $q > 0$  is only defined for systems with  $\text{EEP} < 480$  (i.e. before the first ascent up the giant branch). Our prior therefore becomes

$$\pi(M_{\text{init}}, q | \boldsymbol{\theta}_{\text{cluster}}) \propto \begin{cases} 1 & \underbrace{q = 0}_{\text{Single}} \text{ or } \underbrace{\left( \frac{M_{\min}}{M_{\text{init}}} \leq q \leq 1 \text{ and } \text{EEP} < 480 \right)}_{\text{Binary System}} \\ 0 & \text{otherwise} \end{cases} \quad (\text{D67})$$

where EEP again is a function of  $M_{\text{init}}$  and  $\boldsymbol{\theta}_{\text{cluster}}$ .

A representation of the impact including binaries has on our cluster model is shown in the second panel of [Figure 10](#).

### D.3. Outliers

In addition to the  $\chi^2$  likelihood defined above, clusters are subject to additional contamination due to background/foreground field stars, which are not associated with the assumed SSP. In addition, clusters can also have populations such as blue stragglers ([Sandage 1953](#)) whose stellar evolution has been influenced by interactions with a companion, violating our basic SSP assumption. To account for these outliers, we modify our likelihood for each object to be a weighted mixture of two components such that

$$\mathcal{L}_i(f_{\text{out}} | p_{\text{in},i}) = p_{\text{in},i} \times \mathcal{L}_{\text{in},i} + (1 - p_{\text{in},i}) \times \mathcal{L}_{\text{out},i} \quad (\text{D68})$$

Here,  $p_{\text{in},i}$  is the probability that object  $i$  is well-modeled by our SSP (i.e. an ‘‘inlier’’) and  $1 - p_{\text{in}}$  is the probability that it is not (i.e. an ‘‘outlier’’).

The inlier probability

$$p_{\text{in},i}(p_{\text{mem},i}, f_{\text{out}}) = p_{\text{mem},i} \times (1 - f_{\text{out}}) \quad (\text{D69})$$

is defined to be a mixture of two things. The first is the cluster membership probability  $p_{\text{mem},i}$  for object  $i$  based on possible external information such as spatial position and/or proper motion. The second is the baseline outlier fraction

$f_{\text{out}}$ , which governs the fraction of objects for which our outlier model  $\mathcal{L}_{\text{out},i} > \mathcal{L}_{\text{in},i}$  serves as a better model than our inlier model (i.e. an SSP). This is a free parameter that we are interested in modeling in addition to the cluster parameters  $\theta_{\text{cluster}}$ .

We take our outlier model to be an adaptive threshold such that our likelihood is constant

$$\mathcal{L}_{\text{out},i}(k_i) \equiv \mathcal{L}_{\text{in},i}(\chi_{\text{max}}^2(k_i), k_i) \quad (\text{D70})$$

where the value of the likelihood is defined at the point where the cumulative probability of our  $\chi^2$ -distribution with  $k_i$  degrees of freedom is less than a particular threshold  $p_{\text{min}}$ :

$$\int_{\chi_{\text{max}}^2(k_i)}^{\infty} \mathcal{L}_{\text{in},i}(\chi_i^2, k_i) d\chi_i^2 = p_{\text{min}} \quad (\text{D71})$$

This scheme is functionally equivalent to a Bayesian version of “sigma-clipping” for a given  $p_{\text{min}}$  with two main exceptions:

1. The threshold used is not a constant value but depends on the number of bands  $k_i$  observed for each object  $i$ .
2. An individual object’s contribution to the overall likelihood is *de-emphasized* rather than being completely ignored.

We set  $p_{\text{min}} = 10^{-5}$  by default, a conservative value which corresponds to  $\sim 4.5$ -sigma clipping.

A representation of the impact of outlier modeling on our cluster model is shown in the third panel of Figure 10.

#### D.4. Empirical Isochrone Corrections

While the above model allows us to incorporate most of the behavior seen in open clusters (excluding the impact of rotation) such as binarity (§D.2) and outliers (§D.3), it does not account for systematic modeling issues in the SSP itself as derived from theoretical isochrones such as MIST and the use of synthetic spectra such as those derived from the C3K models. We use a series of *empirically-motivated corrections* (see §5.1) to the underlying isochrones in order to address some of these issues. Note that these are common across all theoretical isochrones, not just MIST, with the exception of specialized grids designed to specifically tackle particular problems.

Our corrections work by adding an additional set of “corrected” surface-level parameters  $\theta'_*(\theta_*, \theta)$  that are a function of the original predicted surface-level parameters  $\theta_*$  as well as the underlying stellar evolution parameters  $\theta$  from the MIST isochrones. In particular, we opt to modify the stellar radius  $\log R_*$  and the effective temperature  $\log T_{\text{eff}}$  (and by proxy the surface gravity  $\log g$  and bolometric luminosity  $\log L_{\text{bol}}$ ) such that

$$\begin{bmatrix} M_{\text{init}} \\ [\text{Fe}/\text{H}]_{\text{init}} \\ t_{\text{age}} \end{bmatrix} \rightarrow \begin{bmatrix} \log g \\ \log T_{\text{eff}} \\ \log L_{\text{bol}} \\ \log R_* \\ [\text{Fe}/\text{H}]_{\text{surf}} \end{bmatrix} \rightarrow \begin{bmatrix} \log g' \\ \log T'_{\text{eff}} \\ \log L'_{\text{bol}} \\ \log R'_* \\ [\text{Fe}/\text{H}]_{\text{surf}} \end{bmatrix} \rightarrow \begin{bmatrix} M_1 \\ \vdots \\ M_b \end{bmatrix}$$

We choose to apply empirical corrections to  $\log R_*$  and  $\log T_{\text{eff}}$  for two reasons. The first is that we expect both to be strongly affected by magnetic fields, which appear to “puff up” stars, making them larger, and contribute to sunspot activity, making them cooler overall (Berdugina 2005; Somers & Pinsonneault 2015; Somers et al. 2020). Magnetic activity tends to increase at lower masses, leading to substantial deviations in the observed properties of stars compared to predictions from models such as MIST which does not take these effects into account. The second reason we choose to apply corrections in this domain is that detailed modeling of binaries already suggests that the MIST models deviate slightly from the observations in these two domains (Choi et al. 2016).

To keep our empirical corrections as simple as possible, we only introduce corrections for masses below  $M_{\text{init}} = 1 M_{\odot}$  and “suppress” the effects of our derived corrections after stars evolve off the MS (i.e. after stars have EEP > 454) and for sub-solar metallicities (where the fits are relatively unconstrained; see §5.2). We further assume that our corrections only involve a single parameter,  $M_{\text{init}}$ , and that they are fully linear. While we experimented with more complex functional forms, we found that there was not enough data to warrant using them. Note that these corrections *do not* deal in any way with evolved stars, such as the red clump and horizontal giant branch. While there are known disagreements between the MIST models and observations at those particular stellar evolutionary phases (Choi et al. 2016), investigating them is beyond the scope of this work.

Altogether, we end up modeling variations in  $\Delta \log T_{\text{eff}} \equiv \log T'_{\text{eff}} - \log T_{\text{eff}}$  and  $\Delta \log R_{\star} \equiv \log R'_{\star} - \log R_{\star}$  using

$$\Delta \log T_{\text{eff}}(\boldsymbol{\theta}) = f_T(M_{\text{init}}) \times g(\text{EEP}) \times h([\text{Fe}/\text{H}]_{\text{init}}) \quad (\text{D72})$$

$$\Delta \log R_{\star}(\boldsymbol{\theta}) = f_R(M_{\text{init}}) \times g(\text{EEP}) \times h([\text{Fe}/\text{H}]_{\text{init}}) \quad (\text{D73})$$

We then propagate these modifications to derive relative corrections  $\Delta \log g \equiv \log g' - \log g$  and  $\Delta \log L_{\text{bol}}(T'_{\text{eff}}) \equiv \log L'_{\text{bol}}(T'_{\text{eff}}) - \log L_{\text{bol}}(T_{\text{eff}})$  via

$$\Delta \log g = -2 \times \Delta \log R_{\star} \quad (\text{D74})$$

$$\Delta \log L_{\text{bol}}(T'_{\text{eff}}) = 2 \times \Delta \log R_{\star} \quad (\text{D75})$$

Our corrections in  $\Delta \log T_{\text{eff}}$  and  $\Delta \log R_{\star}$  have three components. The first,  $f_T(M_{\text{init}})$  and  $f_R(M_{\text{init}})$ , represent the “baseline” shifts in effective temperature and radius, respectively, and are defined to be piece-wise linear functions of  $M_{\text{init}}$  such that

$$f_T(M_{\text{init}}) = \begin{cases} \log [1 + c_T \times (M_{\text{init}} - 1)] & M_{\text{init}} < 1 M_{\odot} \\ 0 & M_{\text{init}} \geq 1 M_{\odot} \end{cases} \quad (\text{D76})$$

$$f_R(M_{\text{init}}) = \begin{cases} \log [1 + c_R \times (M_{\text{init}} - 1)] & M_{\text{init}} < 1 M_{\odot} \\ 0 & M_{\text{init}} \geq 1 M_{\odot} \end{cases} \quad (\text{D77})$$

where  $c_T$  and  $c_R$  can be seen as characterizing the (fractional) offset in  $T_{\text{eff}}$  and  $R_{\star}$ , respectively, as a function of  $M_{\text{init}}$ . The second,  $g(\text{EEP})$ , represents a “suppression” term that reduces the offsets as stars evolve off the MS. We take this to be a modified logistic function

$$g(\text{EEP}) = 1 - \frac{1}{1 + \exp[-(\text{EEP} - 454)/\Delta_{\text{EEP}}]} \quad (\text{D78})$$

where  $\Delta_{\text{EEP}}$  sets the EEP scale over which this suppression takes place. This function strictly decreases from  $1 \rightarrow 0$  as a star evolves off the MS. Finally,  $h([\text{Fe}/\text{H}]_{\text{init}})$  represents an additional “suppression” term that reduces the offsets at sub-solar metallicities. We take this to be a simple exponential

$$h([\text{Fe}/\text{H}]_{\text{init}}) = \exp(A_{[\text{Fe}/\text{H}]} \times [\text{Fe}/\text{H}]_{\text{init}}) \quad (\text{D79})$$

where  $A_{[\text{Fe}/\text{H}]}$  sets the amplitude of the suppression ( $1/A_{[\text{Fe}/\text{H}]}$  can also be thought of as a scale). We note that while this function does suppress contributions at sub-solar metallicities, it actually give a slight *enhancement* for super-solar metallicities. The tests performed in §5.2 and §5.3 did not provide enough evidence to support/refute this effect, and so we opted to leave it in for simplicity.

While we consider  $c_T$  and  $c_R$  as free parameters we are interested in modeling in addition to the cluster parameters  $\boldsymbol{\theta}_{\text{cluster}}$ , we find we do not have enough data to model  $\Delta_{\text{EEP}}$  and  $A_{[\text{Fe}/\text{H}]}$  reliably. After experimenting with a variety of values using the data described in §5.2 as well as observations of Ruprecht 106 taken from Dotter et al. (2018), we ultimately set  $\Delta_{\text{EEP}} = 30$  and  $A_{[\text{Fe}/\text{H}]} = 0.5$ . See Table 4 for a summary of the parameters used to model empirical corrections used in this work and their final set of values.

A representation of the impact these empirical corrections have on our cluster model is shown in the fourth panel of Figure 10. An illustration of the functional forms used for the corrections themselves is shown in Figure 9. We find that the overall empirical corrections substantially improve behavior down to  $M_{\text{init}} \sim 0.5 M_{\odot}$ , which can be seen more clearly in Figure 11 and §E.

#### D.5. Empirical Photometric Corrections

Although we find the set of empirical corrections outlined in §D.4 substantially improve the overall shape and overall offset of the MIST isochrones relative to data from nearby open clusters, they are unable to address overall offsets in photometry that might come from, e.g., slightly different photometric calibrations between the synthetic photometry computed from models versus the real photometry from surveys (such as in the Vega system) or issues with the C3K stellar atmosphere models. Both of these manifest themselves, to first order, as *photometric offsets* between the model predictions and the observed data.

We model these offsets explicitly by introducing a set of scale-factors  $\mathbf{s}_{\text{em}} = \{s_{\text{em},i}\}_{i=1}^{i=b}$  that simply rescale the *data* such that the new flux density  $\hat{F}'_{i,j}$  for a given star  $i$  in band  $j$  is

$$\hat{F}'_{i,j} = s_{\text{em},j} \times \hat{F}_{i,j} \quad (\text{D80})$$

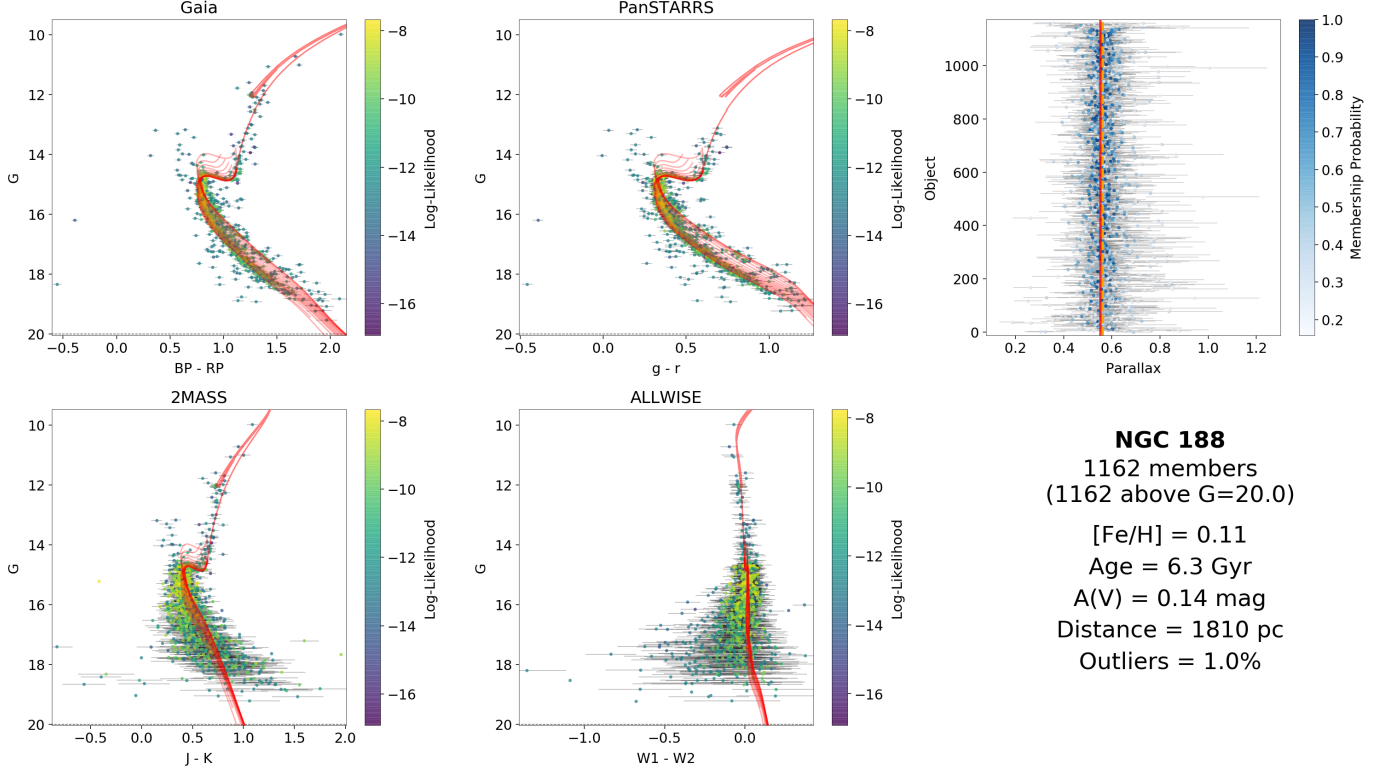


**Figure 20.** As Figure 11, but for NGC 188.

We treat  $\mathbf{s}_{\text{em}}$  as  $b$  free parameters that we are interested in modeling in addition to the cluster parameters  $\theta_{\text{cluster}}$ . We are able to do so thanks to the large number of available parallax measurements from *Gaia* DR2 that give independent constraints on the distance, thereby fixing not just offsets in color but offsets in absolute magnitude.

Our final cluster model after including these additional empirical corrections is shown in the fifth panel of Figure 10.

### E. BENCHMARK CLUSTER FITS

The fits to the remaining five clusters discussed in §5.2 are shown in Figures 20, 21, 22, 23, and 24.

### F. ESTIMATING PHOTOMETRIC OFFSETS FROM FIELD STARS

We aim to estimate  $s_{\text{em},j}$  in each band  $j$  by computing the ratio of the observed flux  $\hat{F}_{i,j}$  for star  $i$  to the predicted flux  $F_{i,j}(\theta, \phi)$ . This will be averaged over the posterior  $P(\theta, \phi | \hat{\mathbf{F}}_{i,\setminus j}, \hat{\omega}_i)$ , estimated from the measured flux densities *excluding band  $j$*   $\hat{\mathbf{F}}_{i,\setminus j}$  for each individual source. Averaging across all  $n$  sources then gives:

$$s_{\text{em},j} \approx \frac{1}{n} \sum_{i=1}^n \int \frac{F_{i,j}(\theta, \phi)}{\hat{F}_{i,j}} P(\theta, \phi | \hat{\mathbf{F}}_{i,\setminus j}, \hat{\omega}_i) d\theta d\phi \quad (\text{F81})$$

Naively, computing this would require generating  $b$  sets of  $n$  posteriors (excluding each band in turn). Instead, we opt to simply reweight the samples from the single set of  $n$  posteriors  $P(F_{i,j} | \hat{\mathbf{F}}_i, \theta, \phi)$  computed using *all* the bands. Assuming that each source  $i$  has a set of  $m$  samples  $\{(\theta_{i,1}, \phi_{i,1}), \dots, (\theta_{i,m}, \phi_{i,m})\} \sim P(\theta, \phi | \hat{\mathbf{F}}_i, \hat{\omega}_i)$  from the underlying posterior, our estimate then becomes

$$s_{\text{em},j} \approx \frac{1}{nm} \frac{1}{\hat{F}_{i,j}} \sum_{i=1}^n \frac{\sum_{k=1}^m w_{i,j}(\theta_{i,k}, \phi_{i,k}) F_{i,j}(\theta_{i,k}, \phi_{i,k})}{\sum_{k=1}^m w_{i,j}(\theta_{i,k}, \phi_{i,k})} \quad (\text{F82})$$

where the importance weights  $w_{i,j}(\theta_{i,k}, \phi_{i,k})$  are defined as

$$w_{i,j}(\theta_{i,k}, \phi_{i,k}) = \frac{P(\theta, \phi | \hat{\mathbf{F}}_{i,\setminus j}, \hat{\omega}_i)}{P(\theta, \phi | \hat{\mathbf{F}}_i, \hat{\omega}_i)} = \frac{\mathcal{L}_{\text{phot},\setminus j}(\theta_{i,k}, \phi_{i,k})}{\mathcal{L}_{\text{phot}}(\theta_{i,k}, \phi_{i,k})} \quad (\text{F83})$$



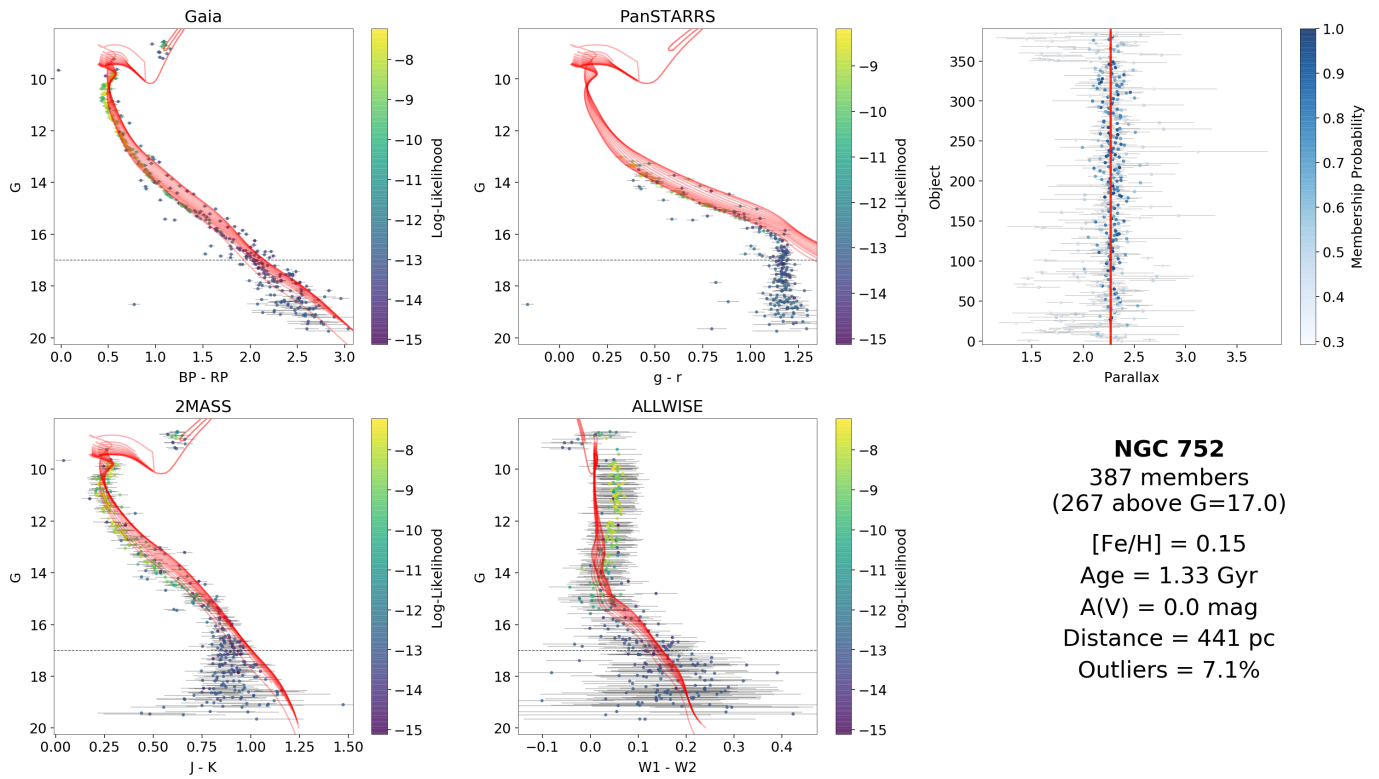


Figure 21. As Figure 11, but for NGC 752.

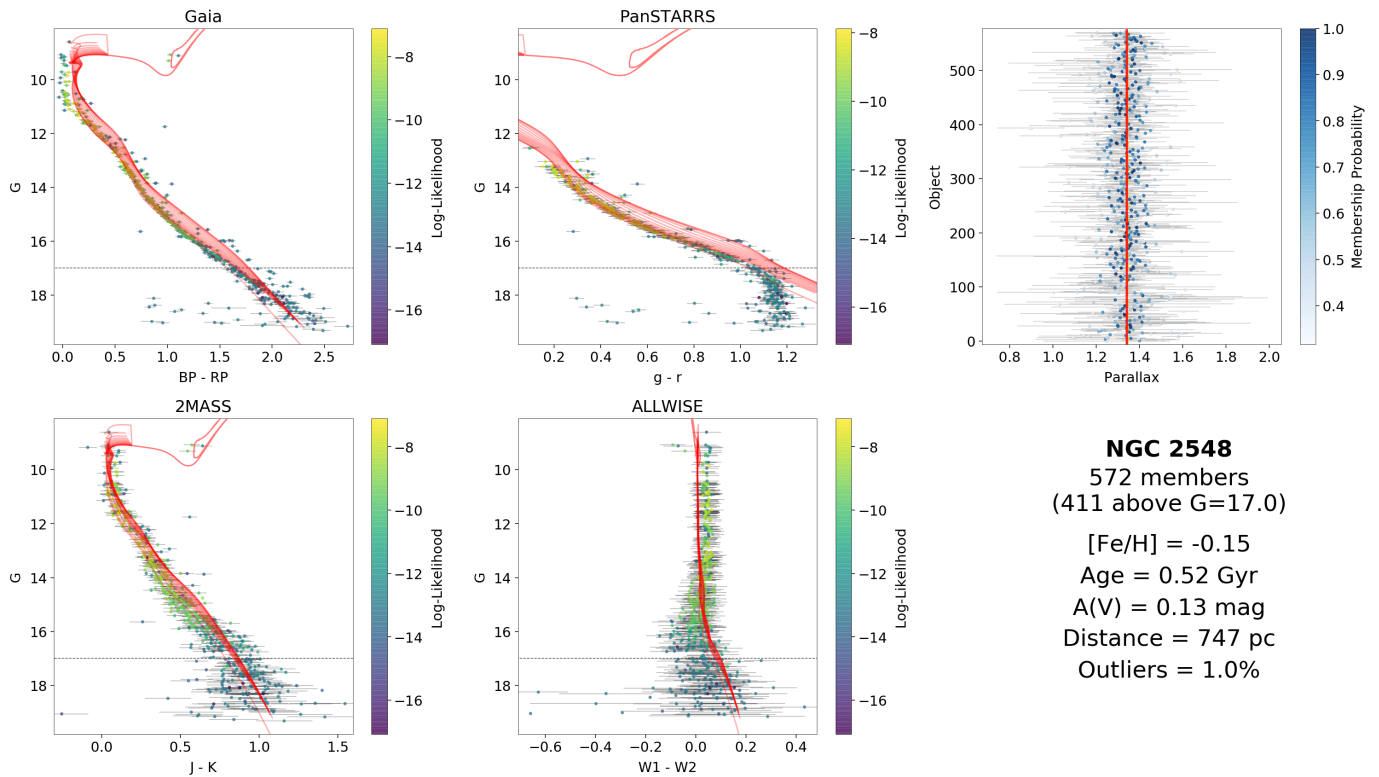
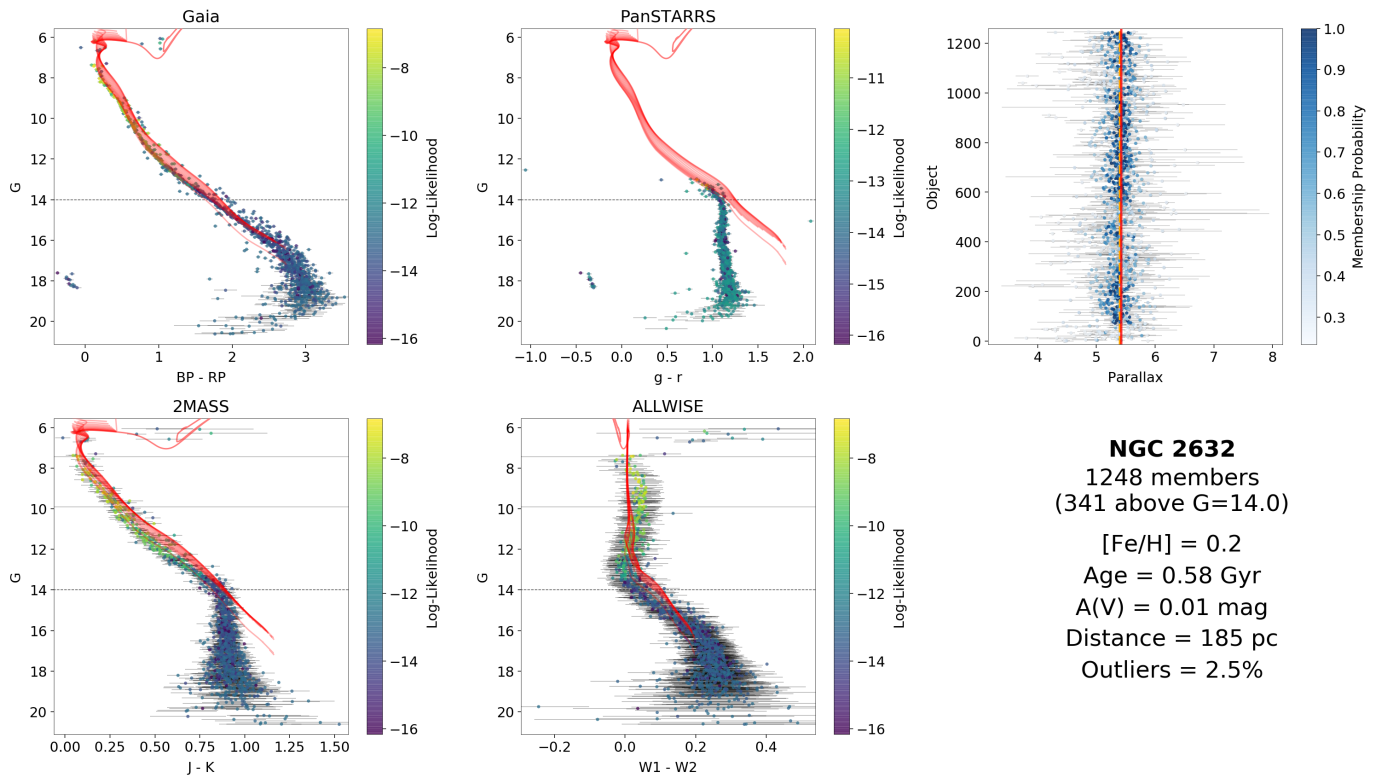
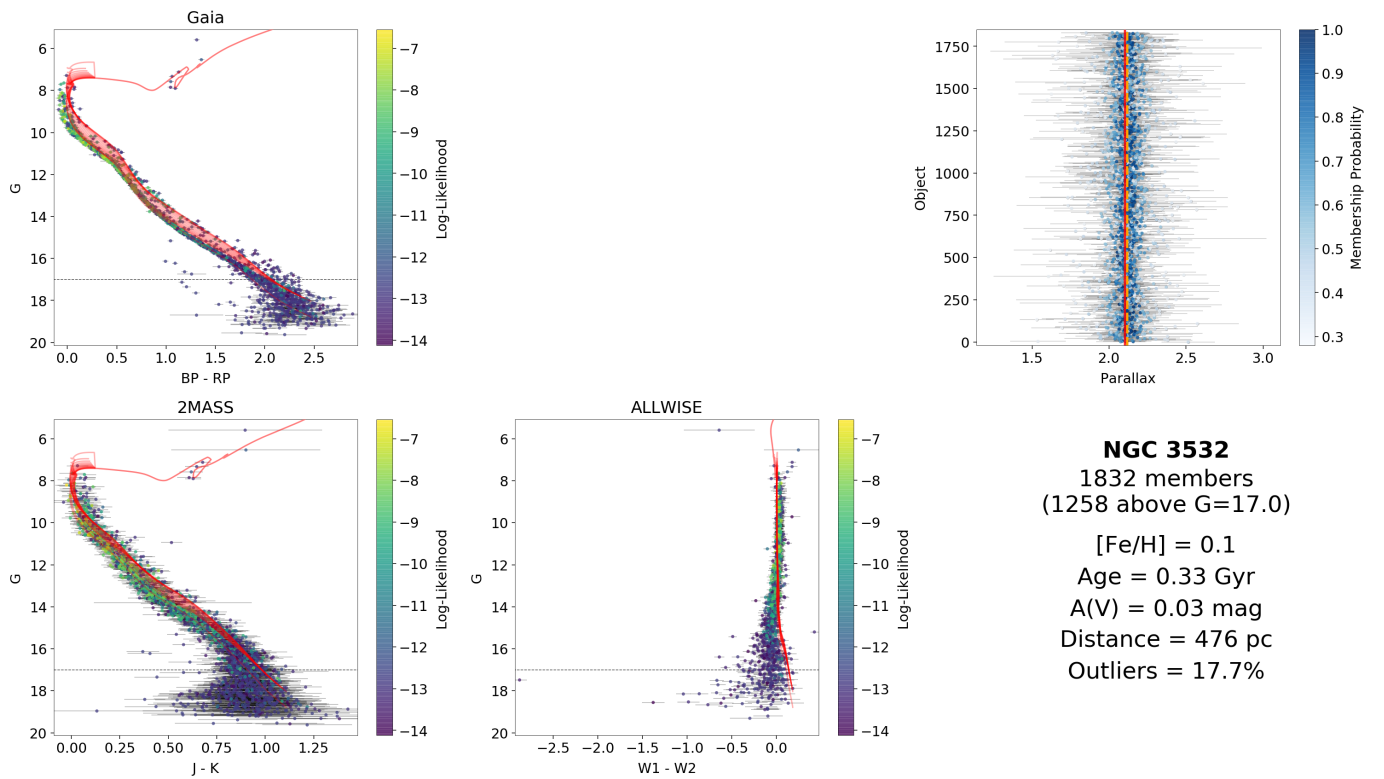


Figure 22. As Figure 11, but for NGC 2548 (i.e. M48).



**Figure 23.** As Figure 11, but for NGC 2632 (i.e. Praesepe).



**Figure 24.** As Figure 11, but for NGC 3532. Note that no Pan-STARRS data was available for use in the fit.

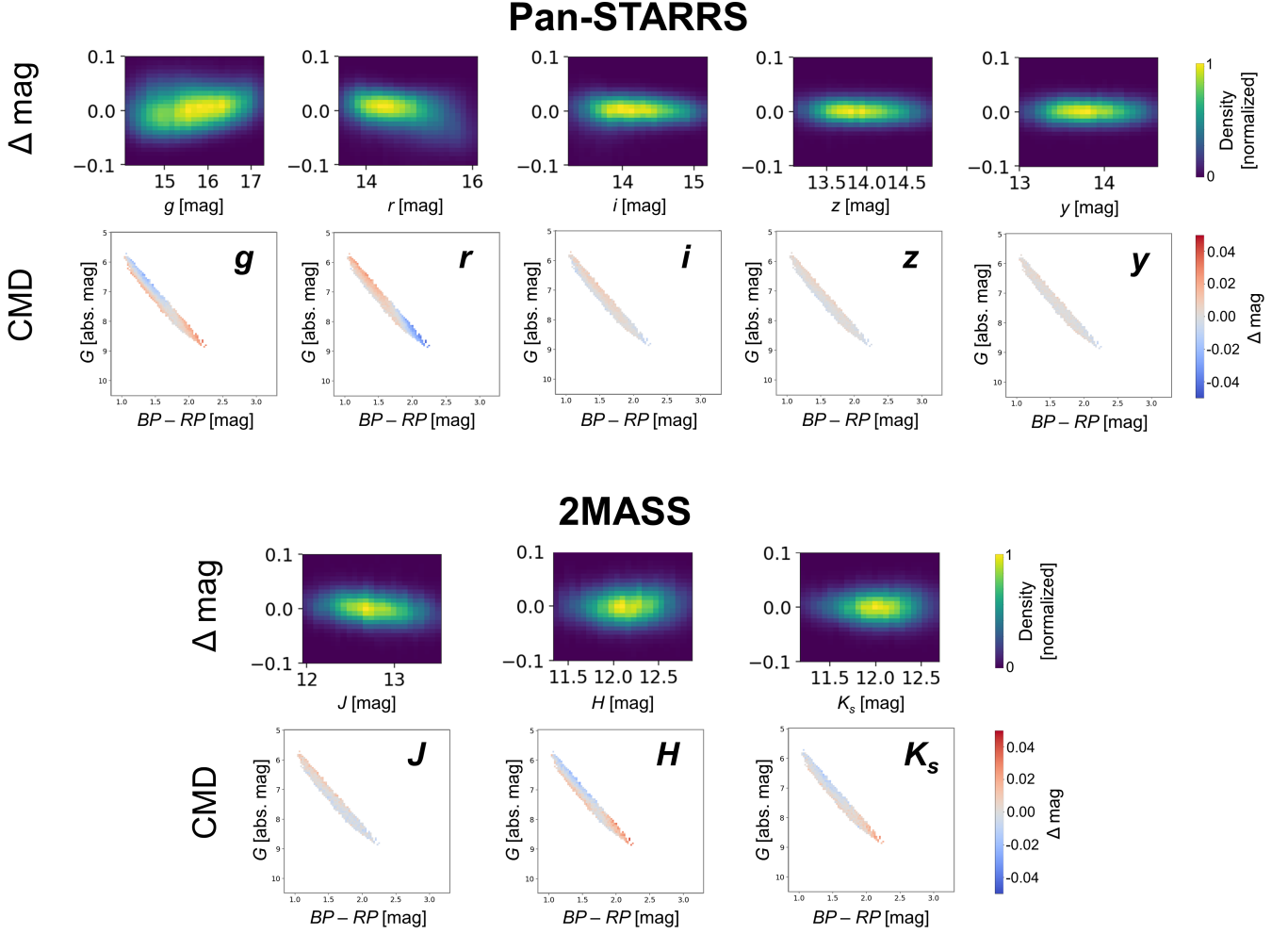


**Figure 25.** Residual magnitude offsets within the *Bayestar* models in the Pan-STARRS (top) and 2MASS (bottom) data over the “benchmark” field star sample (Figure 12) after correcting for mean photometric offsets using the procedure described in §5.3. The top row of each set of figures shows the normalized density of stars as a function of  $\Delta\text{mag}$  versus *Gaia* observed magnitude in each band, while the bottom row shows the corresponding offset as a function of position on the *Gaia*  $G$  versus  $BP - RP$  CMD from Figure 12. Since the empirical *Bayestar* models were originally constructed using both Pan-STARRS and 2MASS photometry, as expected the overall offsets are small ( $\lesssim 1\%$ ) and only display weak trends as a function of magnitude and position of the CMD.

where  $\mathcal{L}_{\text{phot}, \setminus j}(\theta, \phi)$  is the photometric likelihood excluding band  $j$ . Since computing the photometric likelihoods with and without band  $j$  is trivial, this procedure offers a much more computationally efficient way to estimate photometric offsets.

We make three small changes when applying the above strategy in practice:

1. Rather than strictly using the weighted mean of the entire sample, we compute the median of weighted mean estimates from jackknife realizations ( $n = 1000$ ) in order to be less sensitive to possible outliers.
2. We apply a Gaussian prior over  $\mathbf{s}_{\text{em}}$  with a mean of 1 and standard deviation of 0.01 in each band to avoid behavior where a combination of (large) offsets can become degenerate with adjusting entire intrinsic stellar types. We incorporate this into the initial estimate of  $\mathbf{s}_{\text{em}}$  computed above by using bootstrapping to estimate errors in our initial estimate and assuming the PDF is Gaussian.

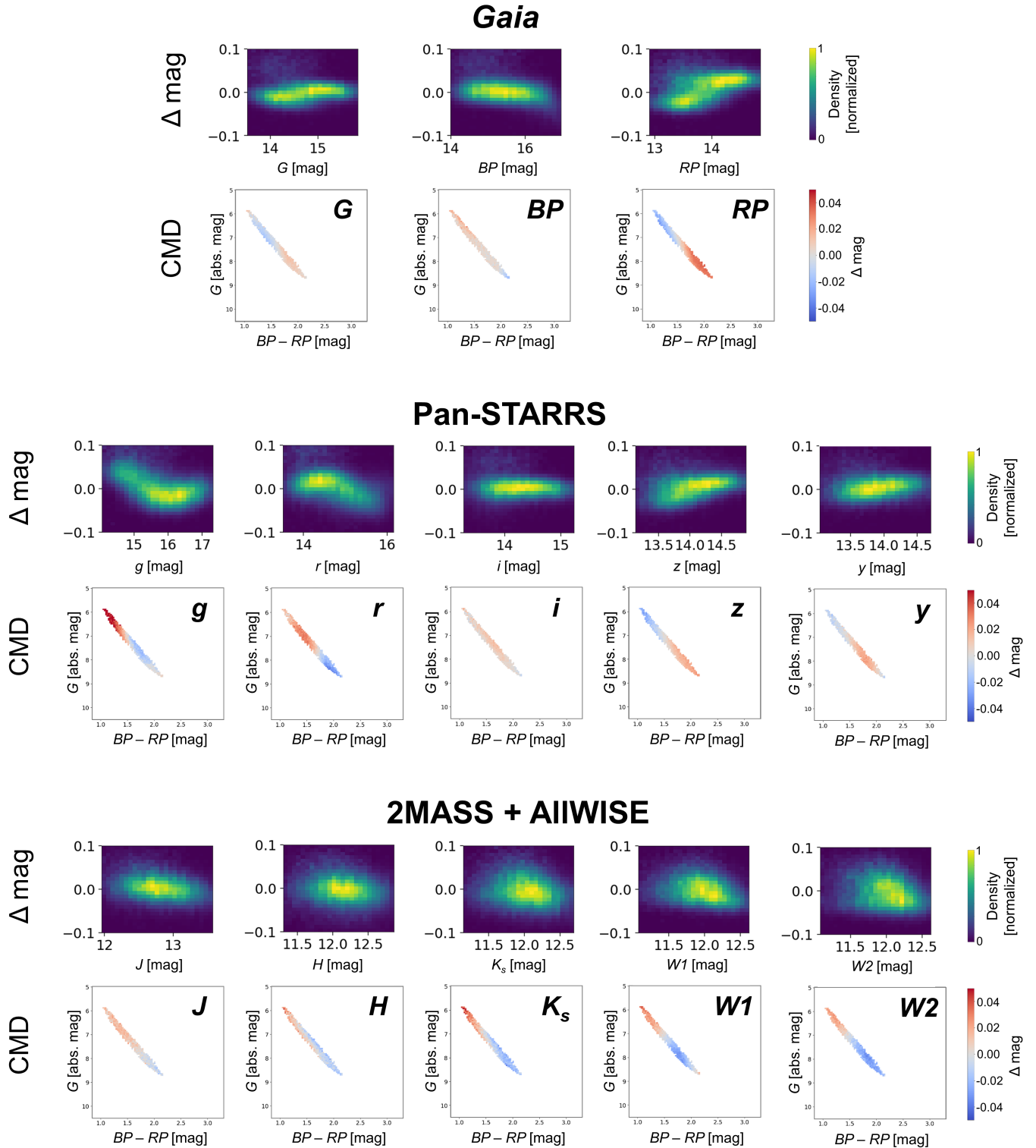


**Figure 26.** As Figure 25, but now showing the residual magnitude offsets within the MIST models in the *Gaia* DR2 (top), Pan-STARRS, and 2MASS+AllWISE (bottom) data. Compared to the *Bayestar* models (Figure 25), the offsets here are substantially larger ( $\sim 3\%$ ) and display strong trends as a function of magnitude and position of the CMD, especially in the bluest and reddest bands.

3. We repeat the process iteratively by applying the  $\mathbf{s}_{\text{em}}$  estimated from the previous stage before computing new estimates of the posteriors. We consider our results converged when each element of  $\mathbf{s}_{\text{em}}$  changes by less than  $\sim 0.01$ .

### G. PHOTOMETRIC OFFSETS ACROSS THE COLOR-MAGNITUDE DIAGRAM

The behavior of our estimated photometric offsets for the **Bayestar** and **MIST** models as a function of magnitude and position on the *Gaia* CMD is shown in Figures 25 and 26, respectively. As expected, the **Bayestar** models do not exhibit large variations since they were calibrated on the same datasets (Pan-STARRS and 2MASS) used in this work. By contrast, we see that the **MIST** models still exhibit large variation ( $\sim 0.05$  mag) across both magnitude and position on the CMD, especially on the blue side. This is in line with expectations from Choi et al. (2016). A combination of this observed behavior, expected systematics from each survey, and the disagreement between estimates of  $\mathbf{s}_{\text{em}}$  derived in §5.2 and §5.3 is then used to set the combined systematic errors in each band listed in Table 5.

### H. A/B TESTS

We investigate the impact various assumptions can have on recovery of extrinsic parameters  $\phi$ , in particular distance  $d$  and extinction  $A_V$ . To do this, we decide to model a subsample of stars in sightlines towards the Orion star forming complex taken from Zucker & Speagle et al. (2019). For each star, we model the 8-band SED (Pan-STARRS and 2MASS) along with the measured parallax from *Gaia* DR2 under four different assumptions:

- *Case 1*: We emulate the setup used in Green et al. (2019) when deriving the 3-D **Bayestar19** dust map, where the underlying stellar models are the **Bayestar** models the  $R_V$  is fixed to a value of 3.3, and there is no 3-D dust prior applied.
- *Case 2*: As above, but now allowing  $R_V$  to vary subject to the prior described in §A.6. This emulates the setup from Zucker & Speagle et al. (2019) and Zucker et al. (2020).
- *Case 3*: As above, but now using the **MIST** models instead of the **Bayestar** models. This approximates the setup in Cargile et al. (2020), where the 3-D dust extinction prior is extremely weak.
- *Case 4*: As above, but now with the full 3-D **Bayestar19** dust map prior applied. This is the default setup in BRUTUS.

The results of each of these tests for a representative subsample of stars that were well-fit in all four cases is shown in Figure 27. While we find some stars do not exhibit many changes in their inferred distance modulus  $\mu$  or extinction  $A_V$ , we do find large variations for many sources. Some of these can be attributed to  $R_V$  variation, such as with source 3, which shows a substantial change in  $A_V$  linked to shifts in  $R_V$  and changes in the inferred intrinsic parameters  $\theta$  as a result. We also see substantial changes for a number of sources when moving from the **Bayestar** to the **MIST** models, many of which are either caused by changes in stellar type or by additional solutions now made available due to the increased diversity of allowed stellar models (see Figure 8). Finally, we see that the 3-D dust extinction prior serves as a strong constraint in many cases, with the inferred  $\mu$  and  $A_V$  constraints both shifting around and tightening considerably. These results, along with the degeneracies discussed in §6.1, highlight the importance of obtaining strong constraints on the dust extinction towards various sources in order to be confident that the inferred  $\theta$  for various stars are both well-constrained and accurate.

We also perform an additional test with an alternate codebase designed to more closely emulate the setup (modeling, priors, etc.) used in Schlafly et al. (2014) and Green et al. (2019). The differences between the two approaches were minimal and could primarily be traced back to differences in the Galactic prior.

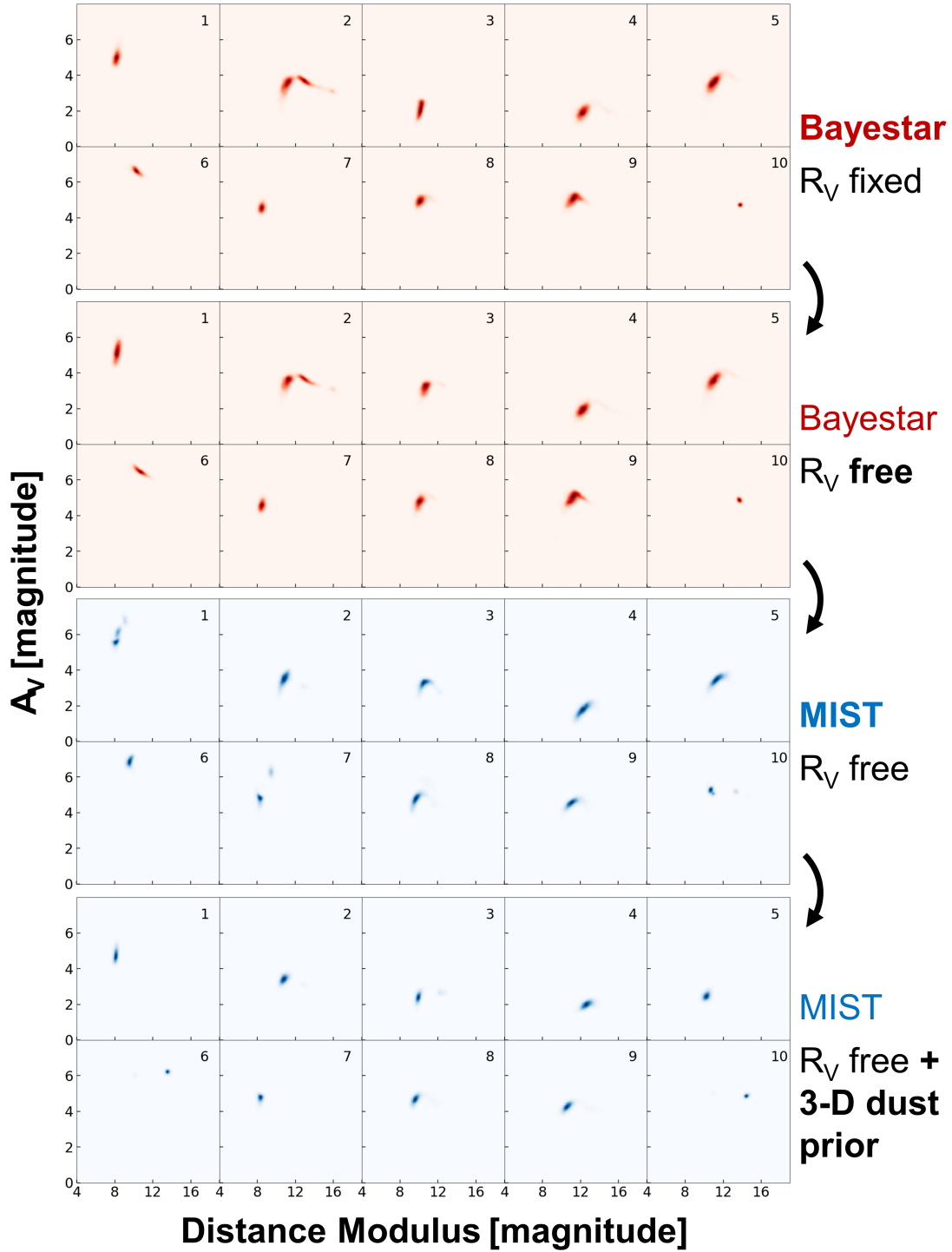


**Figure 27.** Probability density functions (shaded regions) in extinction  $A_V$  and distance modulus  $\mu$  for ten representative stars along sightlines to the Orion star-forming region ( $\ell, b$ ) =  $(204.7^\circ, -19.2^\circ)$  under various modeling assumptions. The top panels show the results for the **Bayestar** stellar models (red) assuming  $R_V$  is fixed (far top) or allowed to vary (middle top). The bottom panels show the results for the **MIST** models before (middle bottom) and after (far bottom) applying the prior from the **Bayestar19** 3-D dust map. While some stars do not show much change, a number of sources show marked changes in inferred distance and/or reddening, illustrating the impact the underlying priors and stellar models when inferring *extrinsic* parameters  $\phi$  for each source (in addition to the *intrinsic* parameters  $\theta$ ).